Low temperature sintering of copper nanoparticles
Mechanism and die attach application

Zhang, Boyao

DOI
10.4233/uuid:777716df-4c4f-4ee8-aa87-eb7f796904a4

Publication date
2020

Document Version
Final published version

Citation (APA)
Zhang, B. (2020). *Low temperature sintering of copper nanoparticles: Mechanism and die attach application*. [Dissertation (TU Delft), Delft University of Technology]. https://doi.org/10.4233/uuid:777716df-4c4f-4ee8-aa87-eb7f796904a4

LOW TEMPERATURE SINTERING OF CU NANOPARTICLE PASTE

MECHANISM AND DIE ATTACH APPLICATION

LOW TEMPERATURE SINTERING OF CU NANOPARTICLE PASTE

MECHANISM AND DIE ATTACH APPLICATION

Proefschrift

ter verkrijging van de graad van doctor
aan de Technische Universiteit Delft,
op gezag van de Rector Magnificus Prof. dr. ir. T. H. J. J. van der Hagen,
voorzitter van het College voor Promoties,
in het openbaar te verdedigen op donderdag 30 april 2020 om 15:00 uur

door

Boyao ZHANG

Master of Science in Materials Science and Engineering,
University of California, San Diego, La Jolla, USA
geboren te Xi'an, China.

Dit proefschrift is goedgekeurd door de promotor:

Prof. dr. G. Q. Zhang

Samenstelling promotiecommissie:

Rector Magnificus,	voorzitter
Prof. dr. G. Q. Zhang,	Technische Universiteit Delft, promotor

Onafhankelijke leden:

Prof. dr. S. Rzepka,	Fraunhofer Institute for Electronic Nano Systems
Dr. K. Pressel,	Infineon Technologies
Prof. dr. U. Staufer,	Technische Universiteit Delft
Prof. dr. R. Ross,	Technische Universiteit Delft
Prof. dr. ir. W. D. van Driel,	Technische Universiteit Delft
Dr. H. W. van Zijl,	Technische Universiteit Delft
Prof. dr. ir. P. M. Sarro,	Technische Universiteit Delft, reservelid

Keywords: Electronics packaging sintering copper nanoparticle paste time-dependent material study MEMS-enabled characterization method

Printed by: Johannes Gutenberg

Front & Back: Beautiful cover art that captures the entire content of this thesis in a single illustration.

ISBN 000-00-0000-000-0

An electronic version of this dissertation is available at
http://repository.tudelft.nl/.

To my parents
For all their devotion and sacrifices.

CONTENTS

SUMMARY

POWER electronics demand miniaturization, integration, higher electrical and thermal conductivities. However, the traditional electronic packaging materials and technology have limitations to meet these requirements. Conventional lead-free die attach materials, like Sn-Ag-Cu solders, can not satisfy high power electronics application, due to their low operating temperatures and intermetallic defects. Therefore, material innovation has attracted much attention in this field. Metallic particle sintering of silver nanoparticle (Ag NP) has become one of the most applied technologies in power electronics industry. Furthermore, to achieve "all copper interconnect" in packaging system, and to reduce the cost further, copper nanoparticle(Cu NP)-based paste has been explored recently in both material synthesis and process development. However, since Cu NPs are reactive and easy to be oxidized, it is challenging to achieve a compatible process, with profound bonding properties. In this thesis, both fundamental understanding of Cu NP-based paste sintering process and die attach process development in power electronics applications are conducted. These two important parts of research works give insight to Cu NP-based paste sintering from various aspects, but on the same physical scale. In this thesis, these knowledge and experience obtained with deep understanding of the material and process can be transferred as one of the significant information to push Cu NP-based paste into industrial application, with deep understanding of the material and processes.

First, to obtain a deeply fundamental knowledge about sintering process, both static and time-dependent characterizations need to be performed, at similar scale as in real application. X-ray diffraction (XRD) is selected due to its large detection volume and valuable material information, both qualitative and quantitive. To enable a dynamic time-resolved X-ray diffraction (TRXRD) study and in-situ sample monitoring, a MEMS-based TRXRD nanomaterial platform is firstly designed and fabricated. It contains an embedded micro-hotplate (MHP) for temperature control and four-point electrical measurement electrodes for sample property monitoring. A gas cell is designed and fabricated to provide an environmental experimental condition, without interference with XRD measurements. To achieve the optimum temperature fast switch and mechanical stability, two designs with different lateral thermal isolation structures, Si_2O and suspended Si membrane with beams, are proposed and fabricated. With these designs, 60 ms and 50 ms minimum heat pulse widths and uniform temperature distribution are achieved. Combined with gas cell and power supply, this set up can enable TRXRD characterization of nanomaterial, with large flexibility of temperature control and gas environment.

Next, with the developed characterization platform, both static and time-dependent investigations on the sintering process of a commercial Cu NPs-based paste are performed under different conditions. Series of XRD patterns and in-situ electrical resistance measurement are collected, followed with detailed XRD analysis and microstructure observation. The sintering process can be determined as three stages during the process: organic solvents evaporation, surface oxides reduction, and NP sintering. In static study, temperature ranges for each stages can be determined, with crystallography and in-situ electrical resistance data. From time-dependent experiment, the sintering process is evaluated from a different perspective. Three sintering stages are also found in the same order from time-dependent study, but in various time frame. These results and insights are on the one hand, a validation of the function of the developed nanomaterials characterization method and platform. On the other hand, they can be transferred to improve and guide process development and material optimization of Cu NPs-based paste.

Last but not least, the in-air pressure assisted sintering behaviors of Cu NP-based paste under various process conditions are investigated and analyzed. Based on the paste characterization results, the in-air sintering temperature range is determined and multiple pressure-assisted sintering experiments in the air are performed. As temperature and pressure increase, Cu NPs form more condensed structures with neighboring particles. Both of these parameters can accelerate the neck formation and inter-particle connection inside Cu joints. The maximum shear strength of $41.63 \pm 4.35\ MPa$ is finally obtained under the sintering condition of $240\ ^{\circ}C$, $25\ MPa$ for $3\ min$. It is also discovered that the highest shear strength improvement can be achieved at $240\ ^{\circ}C$, $10\ MPa$, to $28.1 \pm 8.47\ MPa$, which already meets the requirements for die attach in power electronics applications. Considering the process cost and the risk of the die damaged at high pressure, the optimal sintering condition can be determined. Based on the experiments and characterization analysis, it can be concluded that in-air sintering with pressure assistance of Cu NP-based paste can be applied in die attach for power electronics applications.

SAMENVATTING

VERMOGENSELEKTRONICA vereist miniaturisatie, integratie, hogere elektrische en thermische geleidbaarheid. De traditionele elektronische verpakkingsmaterialen en technologie hebben echter beperkingen om aan deze vereisten te voldoen. Conventionele loodvrije matrijsbevestigingsmaterialen, zoals Sn-Ag-Cu-soldeers, kunnen niet voldoen aan hoogvermogen elektronische toepassingen vanwege hun lage bedrijfstemperaturen en intermetallische defecten. Daarom heeft materiële innovatie op dit gebied veel aandacht getrokken. Sinteren van metallische deeltjes van zilveren nanodeeltjes (Ag NP) is een van de meest toegepaste technologieën in de vermogenselektronica-industrie geworden. Om bovendien "alle koperverbindingen" in het verpakkingssysteem te bereiken en de kosten verder te verlagen, is pasta op basis van koper nanodeeltjes (Cu NP) recentelijk onderzocht in zowel materiaalsynthese als procesontwikkeling. Omdat Cu NP's echter reactief zijn en gemakkelijk kunnen worden geoxideerd, is het een uitdaging om een compatibel proces te bereiken met diepgaande bindingseigenschappen. In dit proefschrift worden zowel fundamenteel begrip van het op Cu NP gebaseerde pasta-sinterproces als matrijsbevestigingsprocesontwikkeling in vermogenselektronica-toepassingen uitgevoerd. Deze twee belangrijke delen van onderzoekswerk geven inzicht in het op sinter NP gebaseerde pastasinteren vanuit verschillende aspecten, maar op dezelfde fysieke schaal. In dit proefschrift kan deze kennis en ervaring die is verkregen met diep begrip van het materiaal en proces worden overgedragen als een van de belangrijke informatie om Cu NP-gebaseerde pasta in industriële toepassing te brengen, met diep begrip van het materiaal en de processen.

Ten eerste moeten, om een diepgaande fundamentele kennis over het sinterproces te verkrijgen, zowel statische als tijdsafhankelijke karakteriseringen worden uitgevoerd, op dezelfde schaal als in echte toepassing. Röntgendiffractie (XRD) is geselecteerd vanwege het grote detectievolume en waardevolle materiaalinformatie, zowel kwalitatief als kwantitatief. Om een dynamisch tijdopgelost röntgendiffractieonderzoek (TRXRD) en in-situ monsterbewaking mogelijk te maken, is eerst een MEMS-gebaseerd TRXRD-nanomateriaalplatform ontworpen en gefabriceerd. Het bevat een ingebedde microkookplaat (MHP) voor temperatuurregeling en vierpunts elektrische meetelektroden voor monstereigenschapscontrole. Een gascel is ontworpen en vervaardigd om een experimentele omgevingstoestand te bieden, zonder interferentie met XRD-metingen. Om de optimale temperatuur snelle schakelaar en mechanische stabiliteit te bereiken, worden twee ontwerpen met verschillende laterale thermische isolatiestructuren, Si_2O en zwevend Si-membraan met balken voorgesteld en gefabriceerd. Met deze ontwerpen worden 60 ms en 50 ms minimale warmtepulsbreedtes en een uniforme temperatuurverdeling bereikt. Gecombineerd met gascel en voeding, kan deze opstelling TRXRD-karakterisering van nanomateriaal mogelijk maken, met een grote flexibiliteit van temperatuurregeling en gasomgeving.

Vervolgens worden met het ontwikkelde karakterisatieplatform zowel statische als tijdsafhankelijke onderzoeken naar het sinterproces van een commerciële pasta op basis van Cu NP's onder verschillende omstandigheden uitgevoerd. Serie XRD-patronen en in-situ elektrische weerstandsmeting worden verzameld, gevolgd door gedetailleerde XRD-analyse en observatie van de microstructuur. Het sinterproces kan tijdens het proces worden bepaald als drie fasen: verdamping van organische oplosmiddelen, reductie van oppervlakte-oxiden en NP-sintering. In statische studie kunnen temperatuurbereiken voor elke fase worden bepaald, met kristallografie en in-situ elektrische weerstandsgegevens. Vanuit een tijdsafhankelijk experiment wordt het sinterproces vanuit een ander perspectief geëvalueerd. Drie sinterfasen worden ook gevonden in dezelfde volgorde uit tijdsafhankelijke studie, maar in verschillende tijdsbestekken. Deze resultaten en inzichten zijn enerzijds een validatie van de functie van de ontwikkelde karakteriseringsmethode en het platform voor nanomaterialen. Aan de andere kant kunnen ze worden overgedragen om procesontwikkeling en materiaaloptimalisatie van op Cu NP's gebaseerde pasta te verbeteren en te begeleiden.

Last but not least worden de in de lucht ondersteunde sintergedragingen van op Cu NP gebaseerde pasta onder verschillende procesomstandigheden onderzocht en geanalyseerd. Op basis van de pastakarakterisatieresultaten wordt het sintertemperatuurbereik in de lucht bepaald en worden meerdere drukondersteunde sinterexperimenten in de lucht uitgevoerd. Naarmate de temperatuur en druk toenemen, vormen Cu NP's meer gecondenseerde structuren met aangrenzende deeltjes. Beide parameters kunnen de nekvorming en verbinding tussen deeltjes in Cu-gewrichten versnellen. De maximale afschuifsterkte van 41,63 ± 4,35 MPa wordt uiteindelijk verkregen onder de sinterconditie van 240 $°C$, 25 MPa voor 3 min. Er is ook ontdekt dat de hoogste afschuifsterkteverbetering kan worden bereikt bij 240 $°C$, 10 MPa, tot 28,1 ± 8,47 MPa, die al voldoet aan de vereisten voor die attach in power elektronische toepassingen. Gezien de proceskosten en het risico dat de matrijs bij hoge druk beschadigd raakt, kan de optimale sinterconditie worden bepaald. Op basis van de experimenten en karakterisatieanalyse kan worden geconcludeerd dat sinteren in de lucht met drukondersteuning van Cu NP-gebaseerde pasta kan worden toegepast in de matrijs voor toepassingen in vermogenselektronica.

1

INTRODUCTION

1.1. METALLIC NP SINTERING FOR POWER ELECTRONICS APPLICATION

With the demand for miniaturization, multifunction, high operation temperature and frequency in power electronics, conventional die attachment materials, such as lead-free solders, are facing challenges [1–3]. As shown in Fig. 1.1, for high power electronics packaging, material innovation is one of the key features to boost its growth. With the environmental restriction, lead-free die-attach materials are required. Conventional lead-free solders, like Sn-Ag-Cu (SAC) alloys, which can be melted at their reflow temperatures (200 - 260 $^\circ C$) [3], can lead to failure when devices operate at a temperature of 300 $^\circ C$ or above. Au-Sn solders have higher reflow temperatures, but it is not cost-effective for high-volume mass production. Furthermore, intermetallic compounds' growth and Kirkendall void formations inside the solder bonding layer can also cause cracks and delamination during device operation. To avoid these problems, metallic nanoparticle (NP) sintering is selected to be the potential solution for future high power electronics packaging. Besides having alloys in the bonding layer, sintered metallic NPs has only one material. This feature can prevent bonding layers or interconnects from failure caused by alloys.

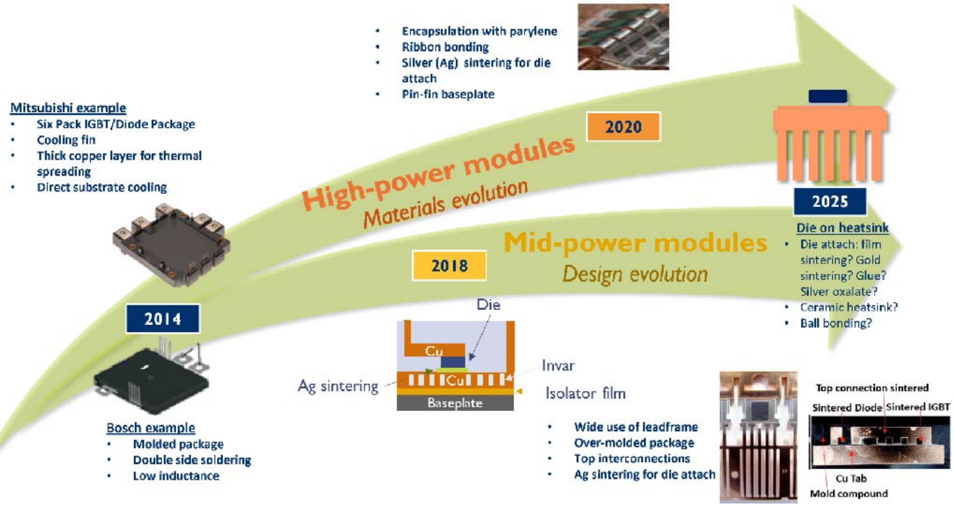

Figure 1.1: Technology roadmap of power electronics packaging.

Metallic NP-based paste sintering becomes the emerging technology in power electronics, especially for die-attach, due to its benefit on material properties and process compatibility. Sintering, which is fundamentally different from soldering, is defined as a densification process that happened far below material melting temperatures. As shown in Figure 1.2, there are several stages involved in the sintering process. Particles start sintering at separated status. In the mediate status, with supplied energy, normally heat or pressure, particles could form connections, which are sintering necks. At this stage, there are still many voids remained between particles. As the sintering process contin-

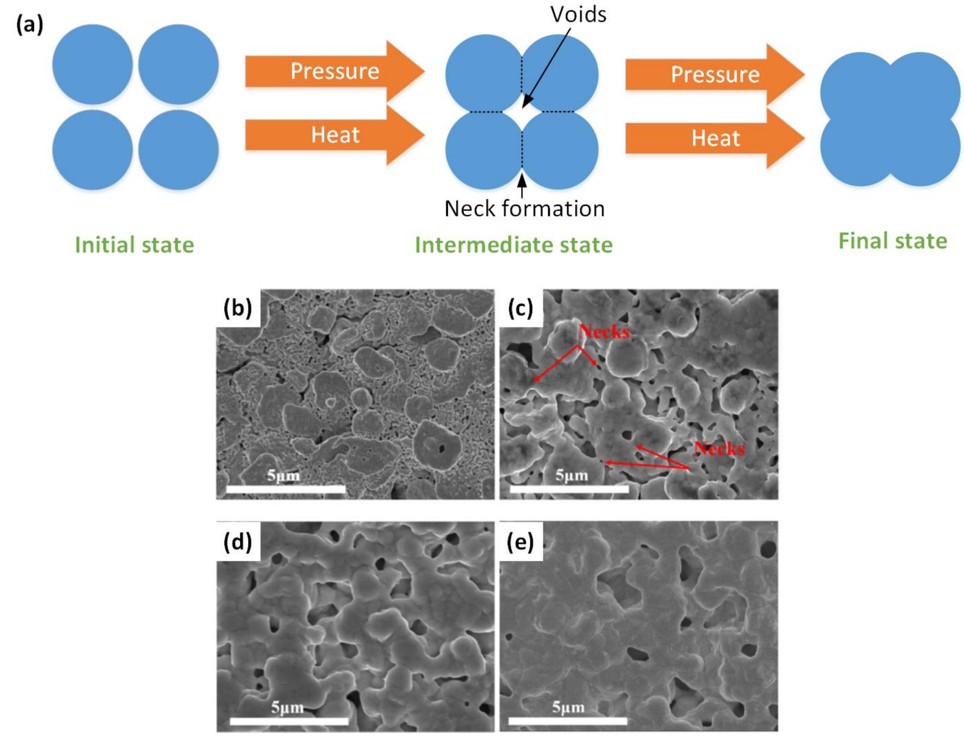

Figure 1.2: (a) Schematic sintering process of metallic NPs. SEM images of microstructures of Ag paste sintered at (b) 200 $^{\circ}C$, (c) 230 $^{\circ}C$, (d) 265 $^{\circ}C$ and (e) 300 $^{\circ}C$ [4].

ues further or supplied with more energy, materials can eventually achieve high-density, with reduced porosity.

In metallic NP-based pastes, there are mostly metallic NPs, and a small volume of multiple types of organic solvents and additives. These organic additives can usually keep metallic NPs from oxidation, modify paste viscosity and bind them together. Thus, NP-based paste can be dispensed, patterned and processed with existing equipment in the packaging industry. As a metal material with high electrical and thermal conductivity, and strong resistance to oxidation, Ag NP-based paste it attracts considerable attention. It has been successfully studied and developed as a bonding material for die attachment in high power electronics applications [5–7]. There are a considerable number of reports explored and studied both on material and on the process, trying to optimize its properties and reveal the fundamental knowledge beneath it [4, 8–11]. Even Ag NP paste sintering has success in die-attach of some high power electronics die attach, this material has difficulty to be applied in wider application range, due to its relatively high price. Thus, researchers continuously seek for alternative materials, with similar performance as Ag but more cost-effective.

1.2. Copper NP-based paste

Cu, as one of the most abundant materials used in electronics packaging, has benefits in cost and compatibility. Thus, Cu NP-based paste attracts more attention as an emerging material. Cu has also high electrical and thermal conductivity, with only 14% of Ag price. In the power electronics packaging application, copper is already widely used in various levels, including bonding substrate, heat sinks, interconnections and wire bonds. Its superior properties and material abundance make it highly promising to be used as a novel die attach material. Thus, an “all copper connection” system, from interconnection inside the device to bonding substrate can be formed by introducing Cu paste into sintering technology [12], as shown in Figure 1.3a. Not only in power-electronics, but also 3D integration, wafer-to-wafer, chip-to-wafer packaging can also benefit from this technology (Figure 1.2b). Therefore, a more reliable, low-cost and high-performance packaging system can be achieved.

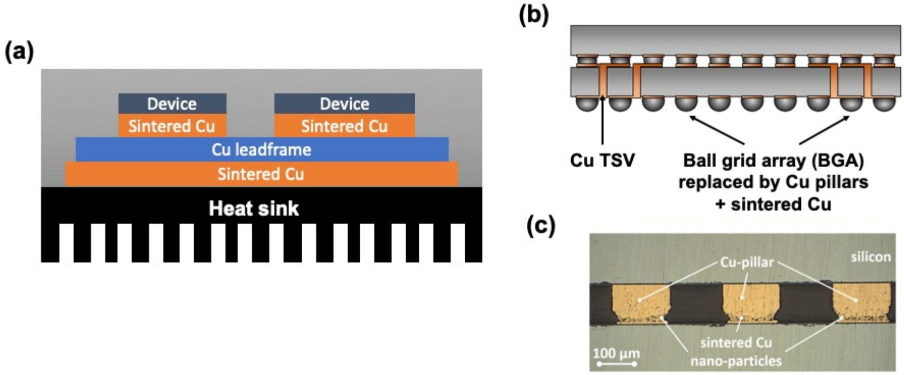

Figure 1.3: Schematic of proposed (a) powerelectronics packaging and (b)3D integration using Cu sintering technology. (c) An example of "all copper interconnect" using Cu pillars and Cu sintering [12, 13].

To understand the state-of-art of Cu NP paste sintering technology, a brief review of the current research works is given as following. Firstly, it starts with material synthesis, which includes variant reports with promising results. Second, several sintering processes related to electronics applications are summarized, Third, to understand the fundamental knowledge of sintering, some mechanism studies are presented in this section, with both experimental and simulation approaches. Last but not least, performance evaluations of sintered joints are also summarized, with some representative research works published previously.

1.2.1. Material synthesis

Similar to the method to synthesize other metallic NPs, reduction in precursor solution is often employed in Cu NP paste synthesis. There are three main steps of synthesis, including dissolving or dispersing precursors, reductants and capping agents, reacting and concentrate reacted solution, as in Figure 1.4. To achieve profound performance, more additives can be included in the system. In this chapter, only main materials, precursors, reductants and capping agents, are discussed. Since Cu is not noble metal as

Ag, it is much more reactive with both oxygen and moisture. With large surface energy of Cu NPs, they are tentative to be oxidized and form hydroxide compounds at room temperature. Thus, capping agents are preferred to be introduced in the system. They can form protection or passivation layers, which will improve the particle dispersion, enhance surface stability and prevent oxidation. In Table 1.1, a summary of current synthesis methods is listed, since 2008. Various materials are evaluated and optimized to achieve stable paste, with higher electrical conductivity. The precursors are often copper salts. Combined with corresponding reductants and capping agents, Cu NPs with passivation layers can be synthesized. Researchers investigated capping agents from several categories, including polymers, organic compounds, and acids. Organic compounds and polymers can isolate Cu NPs from oxidation and agglomeration, by forming condensed passivation layers. Acids are proven to have a good reductive function to remove potential or existence copper oxides. Furthermore, most of the capping agents used in the paste have relative low evaporation temperatures. Thus, there is hardly residues left after sintering.

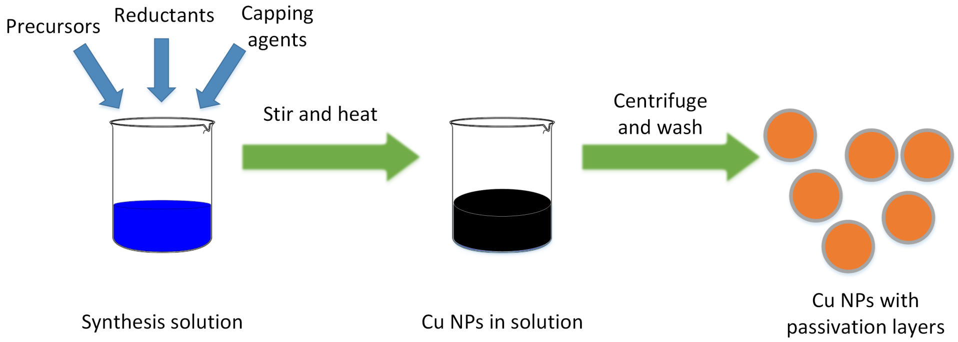

Figure 1.4: Main steps of synthesis of Cu NP paste.

Table 1.1: Cu NP synthesis material and related properties

Year	Precursor	Reductant	Capping agent	Particle size (nm)	Reference
2007	$CuSO_4$	NaH_2PO_2 H_2O	PVP	40-50	[14]
2008	$CuSO_4$	$NaHPO_4$	PVP	30-65	[15]
2012	$Cu_2(OH)_2CO_3$	Oleyl acid	Oleylamine	25-30	[16]
2012	Cu salts	$NaBH_4$	N/A	5-25	[17]
2013	$Cu(OAc)_2$	Hydrazine	Lactic acid	10	[18]
2013	$Cu(NO_3)_2$	$NaBH_4$	Tergitol	10-15	[19]
2013	$Cu(OH)_2$	L-ascorbic acid	PEG-2000	135	[20]
2014	$Cu(acac)_2$	Oleylamine	Oleylamine	10	[21, 22]
2019	$Cu(OH)_2$	Hydrazine	$NTAH_2Na$	50-60	[23]
2019	$Cu(OAc)_2$	Phenylhydrazine	Oleic acid	93	[24]

Additionally, modifying particle morphology and size is also an effective approach to improve the performances of the paste. Cu flakes and spherical particles were synthesized and mixed to prevent crack formation while immersion with neighbored particles [24]. Sintered Cu joints can have low porosity and improved mechanical strength. Furthermore, introducing various particle sizes in one paste is another solution to reduce porosity and crack formations [25–27]. Smaller particles can be used as bridging or filling agents between large particles. They can be easily sintered and achieve high-density sintered Cu at relatively low temperatures.

1.2.2. SINTERING PROCESS

Sintering technology has a long history since prehistoric times. It is defined as a condensation process that happens far below the melting temperatures of materials. The driving force of sintering is the surface energy of materials. Powders, flakes, even nanoparticles tend to have high surface energies. Thus, these are the main materials widely studied in the field of sintering. To condense powders or flakes together, there are multiple methods to provide sufficient energy for sintering, including microwave, heat, optical energy, and spark plasma, etc. For Cu NPs, considering the application, it can be sintered by mainly two approaches: photonic sintering and thermos-pressure sintering. In thermo-pressure sintering, technologies with and without pressure assistance will be discussed.

PHOTONIC SINTERING

With superior electrical conductivity and potentially low price, Cu NP-based conductive material has attracted lots of attention in printed electronics applications widely, as interconnect materials. Direct printing of conductive ink has the potential to be applied to large areas, roll-to-roll manufacturing and compatible with the existing equipment. Different from power electronics, the conductive inks usually have a lower viscosity and less metallic solid content, for ease of printer nozzle dispensing. Furthermore, a flexible and transparent substrate is often required for applications in wearable devices, photovoltaics, RFID tags, and displays. Photonic sintering is a technique employs light as an energy source for NPs to sinter. It has advantages in flexible substrate process, low-cost and non-contact feature. In the sintering process of Cu NP ink, intense pulse light (IPL) and laser are the two most applied methods. Both of them can provide high energy density in pulse form, which can lead to Cu NPs condensation or even melt. Thus, a sintered Cu connection can be formed within milliseconds.

IPL usually uses a Xenon lamp, which gives incoherent pulses of light, typically milliseconds, with a wide spectrum. Cu NPs can absorb the light and transfer photonic energy into thermal energy, which raises the local temperature [28]. As investigated by Park, the localized temperature can exceed 300 $^\circ C$, within the pulses. It gives Cu NPs sufficient energy to form condensed connection networks with neighboring particles. H-S. Kim and co-workers have done a series of IPL sintering, using a white light Xenon lamp [29–39]. To improve the electrical conductivity and robustness of sintered Cu NP, carbon nanotubes (CNTs) [35] and Cu nanowires [36] were added in the ink. The light wavelength, energy, pulse number, and duration were studied extensively for optimization [19, 33, 37, 38, 40]. The lowest electrical resistivity of 6.97 $\mu\Omega \cdot cm$ was achieved by relating the wavelength to the plasmonic wavelength of Cu NPs. to reduce and sinter Cu NPs. Thick copper conductors 13.2 μm, with a resistivity of 11.4 $\mu\Omega \cdot cm$ [24]. It was found that IPL also has a reduction capability to turn CuO into Cu and sinter them further [31, 38].

This reduction effect was believed to corporate with reductive agents produced by reaction between IPL and organic compounds in ink. These by-products from additives provide a novel method for Cu NP sintering.

Instead of using incoherent IPL, a laser was also proven to sinter Cu NP. Since it has much higher energy output than IPL and focused beam size, it was applied to induce local sintering and patterning [41–46]. Selective laser sintering in inert gas can give high quality, low resistivity Cu lines with fine pitch $< 5\ \mu m$ [43]. Furthermore, laser sintering also has an advantage in sintering speed. With femtosecond laser sintering (800 nm, 100 fs), Cu NPs surfaces can reach a high temperature, and melted within a few picosecond [42]. Due to its high energy density, laser sintering also can induce a reduction process during sintering [41], which acid can be produced from polymer solvents. A resistivity of 31 $\mu\Omega \cdot cm$ can be achieved with 10 μm-thick electrodes.

THERMO-PRESSURE SINTERING

Recently, there have been many reports on the Cu NP paste fabrication process and attempts to investigate and optimize its application in die attachment. Typically, pressure-assisted sintering with a protective or reductive gas atmosphere can result in a high shear strength [4, 47–49]. To reduce copper oxides and prevent further oxidation, inert gas or even reductive gas are required during the process, including formic acid gas, 5% H_2 + 95% N_2, or Ar. The highest shear strength of 51.7 MPa is achieved using pressure-assisted sintering with reductive treatments [49]. As shown in Figure 1.5, in this work, a formic acid treatment at a pressure of 10 MPa for 10 min at 260 $^\circ C$ was applied in order to achieve better mechanical properties. It included a dedicated wet chemical treatment and a relatively long sintering process time. As in industrial applications, processing gas and complex wet chemical treatments are time-consuming and costly.

Pressureless or low pressure (lower than 1 MPa) sintering offers the advantage of process simplicity. Furthermore, thin dies can avoid the damage risk from pressure. However, it sometimes requires extreme process conditions [50–52], like 100 % H_2 atmosphere, or mixing with other types of materials [22, 53, 54]. The purpose of these conditions is to provide strong reductive agents, in gas or liquid form. Therefore, any traces of copper oxides during the process can be reduced. A long-range and strong connections among Cu NPs can be formed at elevated temperatures. Besides pure H_2 atmosphere, pressureless sintering in 5% H_2 + 95% N_2 or inert gas has also been reported [23, 55]. However, the shear strength of sintered Cu NP joints is sometimes too low, which cannot meet the die attach application requirements [53, 55]. Additionally, the sintering process time reported is usually between 20 min and 1 hour, or even longer. This long process time can also decrease the throughput in mass production, which will raise the cost of the process. It is a challenge to develop a reliable and cost-effective sintering process for Cu NP paste without pressure assistance. Consequently, pressure-assisted sintering in the ambient air can achieve high quality sintered Cu NP joints, without the complexity of process conditions, is required.

1.2.3. SINTERING MECHANISM AND ITS INVESTIGATION METHODS

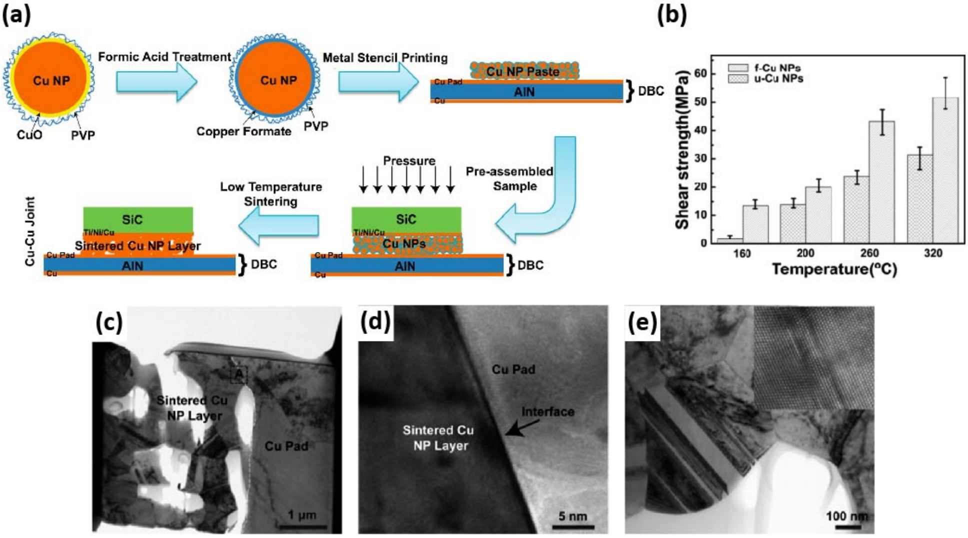

Figure 1.5: (a) Schematic representation of the formation of Cu joints. (b) Shear strengths of Cu joints using paste containing formic acid-treated Cu NPs and Cu NPs without, sintered at 160, 200, 260 and 320 $^{\circ}C$ for 5 min. (c) The TEM image of Cu pad/Cu joints sintered with formic acid-treated Cu NPs at 260 $^{\circ}C$. (b) Te HRTEM image of area A showing on the interface. (e) The TEM image of twins formed in the sintered Cu layer. Inset: HRTEM of the twins [49].

MOLECULAR DYNAMIC SIMULATION METHOD

Considering the nano-size particle inside Cu paste, it is a challenge to use experimental methods to analyze the sintering mechanism, as it with variable processing parameters. Consequently, molecular denyamic (MD) simulation is employed to investigate the sintering process, which can potentially reveal more fundamental phenomena. By applying isothermal sintering simulation on a free-standing two spherical Cu NPs system, the whole process is divided into three regimes, by contact and melting point. As shown in Figure 1.6, different mechanism can be observed to be dominated under various situations [56–59]. After initial contact between two particles, it can be visualized that the hexagonal close-packed (HCP) structure was found at the sintering neck area [56]. The HCP structures formed inside the face-centered crystal (FCC) are considered as stacking fault (or twin boundaries) on (111) planes. These crystal defects may have an essential impact on promoting diffusion on the interface. Formation of single- and multi-fold stacking faults (twinning) is reported to have a different method [42]. Multi-fold stacking was found in the simulation to occur via a series of shear and rigid-body rotation processes, caused by elastic waves. The heating rate impact on the process is also investigated [59]. Similarly, FCC structures or stacking faults also appeared in the necking area. However, these defects disappeared after a few picoseconds. They then gradually transformed into other crystal structures due to the superheating. Furthermore, the critical function of (111) surface on fast surface diffusion was studied previously by the experimental approach [60]. The system used oriented (111) surface, instead of NPs. TEM observation confirmed the essential role of (111) plan in the diffusion of the bonding

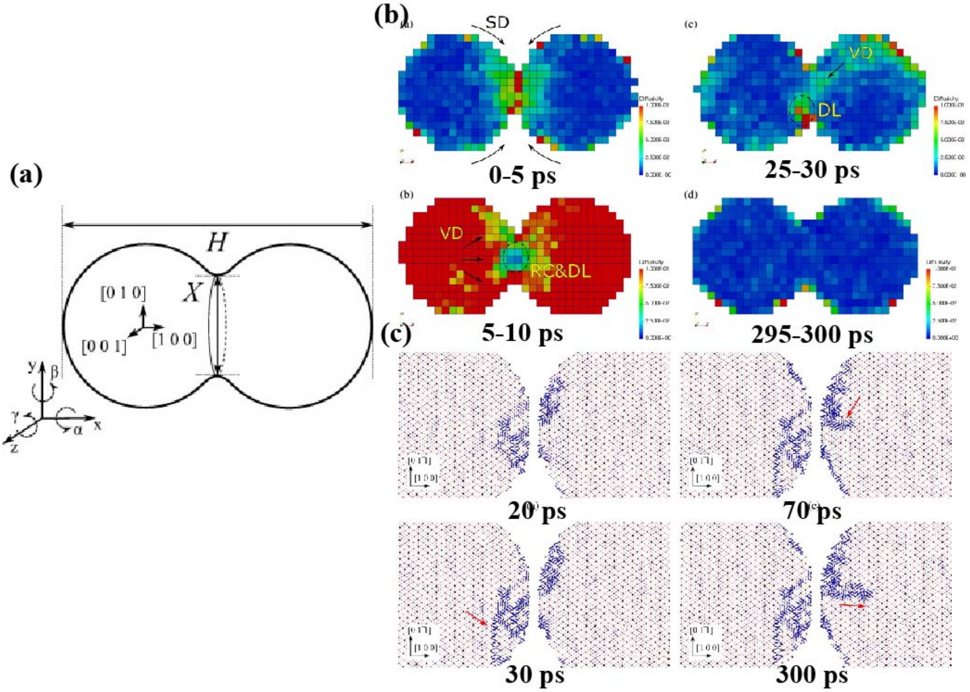

Figure 1.6: a) Schematic diagram of two-particle sintering. (b) Local diffusivity during isothermal sintering at 1000 K with perfect alignment of atoms between various time periods. SD stands for surface diffusion, VD is volume diffusion, RC is recrystallization and DL is dislocation. Units of diffusivity is 0.1 $mm^{(}2)/s$. (c) Dislocation at 1000 K at various times [58].

process.

However, due to the simulation limitation, the Cu NP built in the simulation is usually under 10 nm, which is much smaller than the application. Sintering temperature applied in the simulation is between 300-1000 K, where small NPs will melt. Atomic movement and property of sintered material can be variant from the real situations. Thus, obtained simulation results need to be related to experimental observations. Furthermore, intrinsic defects inside Cu NPs, including vacancy, dislocation, are not taken into simulations, which might have a high impact on the sintering process. More simulation studies including these factors should be conducted in the future.

EXPERIMENTAL APPROACH

Based on the current characterization methods, there is a number of researchers explored the sintering mechanism using experimental approaches, from macro to nanoscales. Thermodynamic change during the process was studied by Mittal [61]. From (differential scanning calorimetric (DSC) results, an exothermic process was observed, indicating that surface energy of the system is lowered, while particles are fused. In this work, dislocation slipping was also observed in-situ under transmission electron microscope (TEM), where the strong sintering process occurred. The work of Mittal provides experimental evidence that crystal planes move through dislocations slipping, which results in a lower energy level of Cu NPs after sintering. As a material used in interconnect and bonding application, electrical property is essential. However, an $in-situ$ resistance monitoring experiment is only conducted with Ag paste [62]. Limited experimental data is received for electrical resistance change during Cu NP sintering [26].

In order to understand the material behavior at the atomic level, TEM is often employed to capture the particle change at various sintering status. In-situ TEM heating applied in Ag NP sintering confirmed twin defects play important role in sintering neck formations [11, 61]. At different temperature range, particles sintering can be dominated by specific mechanisms. Similar phenomena are also observed in Cu NP sintering. J. Liu showed the twin-type dislocation at the interface between sintered Cu and Cu substrate [49]. Liu and co-workers also observed hexagonal dislocation network at the grain boundary, using bright-field TEM [60]. Theses coherent twins are believed to enhance both mechanical and electrical properties of sintered joints, especially at interfaces.

There are limited researches conducted on low-temperature sintering of Cu NP paste, especially time-dependent studies which provide dynamic information about materials as conditions change. $In-situ$ TEM at elevated temperature can reveal the mechanism at the atomic level, but it only applies in the two-particle system, most in ultra-high vacuum. These conditions can deviate far from applications. Besides TEM, the obtained knowledge about dynamic material change during sintering, including structure, electrical and thermal properties, is limited.

1.2.4. PERFORMANCE EVALUATION

ELECTRICAL PROPERTY

Table 1.2: Electrical resistivity and corresponding sintering conditions

Particle size (nm)	Temperature (°C)	Pressure (MPa)	Time (min)	Atmosphere	ρ ($\mu\Omega \cdot cm$)	Reference
30-65	200	0	60	Formic acid	3.6	[15]
350	FLS	0	-	Air	5.8	[25]
<100	FLS	0	-	Air	6.97	[37]
93	FLS	0	-	Air	7.1	[24]
10	200	0	60	N_2	9.1 ± 2.0	[18]
25-30	300	0	20	H_2	13	[16]
10	350	0	60	H_2	13.7	[21, 22]
135 ± 30	250	0	30	N_2	15.8	[20]
50-60	200	0	30	N_2	16	[23]
40-50	325	0	60	Vacuum	17.2	[14]
10-15	IPL 22.4 (J/cm^2)	0	-	Air	96	[19]

As an interconnect material, the electrical property of sintered Cu particles is one of the most important perspectives to investigate. Table 1.2 summarizes some of the important sintering research works evaluating the electrical resistivity regarding different sintering conditions. Most of the works included have applications in printable interconnect on a flexible substrate. Therefore, there is no pressure applied in the process. Thermal sintering and photonic sintering are the main methods used. From the table 1.2, thermal sintering needs reductive atmosphere to achieve good electrical conductivity. Furthermore, the process time is between $20-60$ min, which is much longer than photonic sintering. With energy from flash light or impulsed light, sintered Cu NPs can achieve lower resistivity in an ambient atmosphere using photonic sintering, with appropriate energy and wavelength. It is possible that photonic sintering can rise up local temperature above 300 $^\circ C$ in milliseconds, which can have an effect on the oxidation prevention.

MECHANICAL PROPERTY

Table 1.3: Shear strengths and corresponding sintering conditions

Particle size(nm)	Temperature ($^\circ C$)	Pressure (MPa)	Time (min)	Atmosphere	Shear strength (MPa)	Reference
70-200	200	0	60	Formic acid	19 ± 5	[12]
40-60	200	0	20	N_2	0.7	[55]
50-60	200	0	30	N_2	39	[23]
50	300	0	11	N_2	24.8	[54]
1 wt% NiO	350	0.002	5	H_2	30.5	[63]
Flake 690	300	0.08	5	Formic acis	30.9	[48]
60.5	300	1.08	60	Ar-5%H_2	31.88	[64]
100-1000	250	4	5	Air	20	[27]
25-30	150 and 250-350	5	10	H_2	>30	[16]
50, Phosphated	250	8	5	Air	20	[65]
40	300	10	10	Air	>40	[66]

As die-attach is a major application for Cu paste sintering, shear strength is widely used to investigate the mechanical property of sintered joints. Table 1.3 summarizes the shear strength and corresponding sintering conditions from recent research reports. Most of the sintering processes are conducted in a protective or reductive atmosphere, at a temperature of 300 $^\circ C$ or above, which can be challenging and costly to be embedded in current sintering technology and environment. Furthermore, pressureless sintering attracted much attention, due to its simplicity of process and low risk of device damage. However, the sintering time is quite long, from 20 – 60 min, to achieve qualified shear strength. Power electronics has a large variation in die sizes, depending on the device types. Only a limited number of die sizes were tested these process conditions, which may prevent them from transferring to wider application ranges. In-air sintering was also explored by a few researchers. According to their results, a reasonable level of pressure, normally > 4 MPa, is required to achieve strong sintered joints.

1.3. CHALLENGES AND GAPS

ALTHOUGH much efforts were devoted to the computational approaches to investigate the underlying mechanism of Cu NPs low-temperature sintering, there are insufficient experimental results reported. Furthermore, an in-situ or dynamic study has high value in revealing the sintering process at different status. In-situ TEM studies, focusing on only a limited number of particles in the view field, only provide information that may apply for a small system. Dynamic macro to micro-level study can rarely be found, which can offer a systematic, complete information about sintering.

In current sintering technology for Cu NP-based paste, the protective or reductive atmosphere is mostly needed, due to risk of oxidation at process temperature. However, long process time is another challenge especially for die-attach application. Furthermore, considering the cost and compatibility of industrial productions, most of the reported process may face many challenges, when it needs to be embedded in the existing production flow. Thus, a simplified, cost-effective and compatible sintering solution is required for Cu NP-based paste.

1.4. RESEARCH OBJECTIVES

WITH the demand in future high power electronics application, Cu NP-based paste has the potential to replace Ag paste, with similar performance and lower cost. However, the sintering process of Cu NP-based paste is still not completely understood. On the other hand, there is insufficient fundamental knowledge reported regarding the Cu NPs sintering process. Both experimental and simulation methods should be applied to explore more detailed information. Combined with fundamental knowledge and process, Cu NP-based paste may be applied widely in the high power-electronics application, including die-attach and other interconnections. Thus an “all copper” interconnect shall be achieved.

In this thesis, a new material characterization method and platform is proposed and applied in the Cu NP-based paste sintering study. It can reveal the detailed information about the inner structure and electrical property change of Cu paste as a collective behavior in micrometer-thick sample. This information can be combined with other studies to a shine light on both material development and process optimization. Furthermore, the sintering behavior of one commercial Cu paste is also investigated. The results showed the possibility to achieve Cu joints in air, with good mechanical strength and microstructure.

1.5. OUTLINE OF THESIS

THE outline of this thesis is as follows: A brief review of the current status of time-dependent characterization methods of nanomaterial is given in Chapter 2. A few widely used methods are discussed in detail, including transmission electron microscopy (TEM), scanning electron microscopy (SEM), and X-ray diffraction (XRD). MEMS-based devices and systems developed and applied in $in-situ$ TEM and SEM observations are summarized and discussed. There are a considerable amount of researches conducted, with insights obtained to reveal the micro or atomic level mechanism. In XRD field, the approach to achieve time-resolved or in-situ measurement is different. Limitations and disadvantages of these approaches are investigated in this chapter.

In Chapter 3, a MEMS-based nanomaterial characterization platform for time-resolved X-ray diffraction (TRXRD) is designed and fabricated, in order to achieve time-dependent study of Cu NP sintering. To fulfills the requirement of TRXRD study, a microhotplate (MHP) is embedded in the MEMS device, with a four-point electrical resistance measurement structure. Fast temperature switch and uniform temperature distribution can be achieved. According to device assessment, millisecond temperature switch time can be obtained. A gas cell is introduced to provide an environmental condition, while heating. Packaging of the MEMS chip was designed to enable plug-in loading, which is convenient and cost-effective. Additionally, the validation of the platform is included.

Chapter 4 illustrates the obtained fundamental understanding of Cu paste sintering, while mimicking the real application. A series of sintering experiments were conducted using the platform developed in Chapter 3. TRXRD method was applied, with in-situ electrical resistance measurements to investigate the process from different aspects . There are two temperature profiles included in this study. One is step temperature, from 150 - 285 $^\circ C$, with 25 $^\circ C$ step, in 5% H_2 + 95% N_2 atmosphere. With results obtained from the first profile, the critical changing point of electrical resistance and XRD patterns can be determined. The second temperature profile is heat pulses at critical changing points, which conducted with TRXRD method. Materials microstructure evolution is separated in time scale, by applying millisecond-heat pulses. Combined TRXRD and microstructure observation, an insight of Cu NP sintering can be given. This information can be used to guide further material development and process optimization.

In Chapter 5, in-air sintering behavior of this commercial Cu paste is studied, by applying various pressures and temperatures, using an industrial instrument. Sintering temperature range is firstly determined by material characterizations in air. Three temperatures and five pressures are selected then, based on the characterization results. After sintering experiments, shear strength and microstructure of fracture surfaces are analyzed and discussed. It is found that both temperature and pressure have a promote role during the process. An optimal sintering condition in the air is obtained from this study.

REFERENCES

[1] Thomas Siewert. *Properties of lead-free solders.* Thesis, 2002.

[2] P. G. Neudeck, R. S. Okojie, and Liangyu Chen. High-temperature electronics - a role for wide bandgap semiconductors? *Proceedings of the IEEE*, 90(6):1065–1076, 2002.

[3] Y. Yamada. *Die-Attach Materials for High Temperature Applications in Microelectronics Packaging*, pages 181–196. Springer International Publishing, 2019.

[4] Jie Li, Xin Li, Lei Wang, Yun-Hui Mei, and Guo-Quan Lu. A novel multiscale silver paste for die bonding on bare copper by low-temperature pressure-free sintering in air. *Materials & Design*, 140:64–72, 2018.

[5] Seyed Amir Paknejad and Samjid H. Mannan. Review of silver nanoparticle based die attach materials for high power/temperature applications. *Microelectronics Reliability*, 70:1–11, 2017.

[6] Hui Yu, Liangliang Li, and Yujun Zhang. Silver nanoparticle-based thermal interface materials with ultra-low thermal resistance for power electronics applications. *Scripta Materialia*, 66(11):931–934, 2012.

[7] Hao Zhang, Yang Liu, Lingen Wang, Fenglian Sun, Jiajie Fan, Mark D. Placette, Xuejun Fan, and Guoqi Zhang. Effects of sintering pressure on the densification and mechanical properties of nanosilver double-side sintered power module. *IEEE Transactions on Components, Packaging and Manufacturing Technology*, 9(5):963–972, 2019.

[8] Chengjie Du, Xin Li, Yunhui Mei, and Guoquan Lu. An explanation of sintered silver bonding formation on bare copper substrate in air. *Applied Surface Science*, 490:403–410, 2019.

[9] Z. Zhang, C. T. Chen, Y. Yang, H. Zhang, D. Kim, T. Sugahara, S. Nagao, and K. Suganuma. Low-temperature and pressureless sinter joining of cu with micron/submicron ag particle paste in air. *Journal of Alloys and Compounds*, 780:435–442, 2019.

[10] Chuantong Chen and Katsuaki Suganuma. Microstructure and mechanical properties of sintered ag particles with flake and spherical shape from nano to micro size. *Materials & Design*, 162:311–321, 2019.

[11] M. Y. Li, Y. Xiao, Z. H. Zhang, and J. Yu. Bimodal sintered silver nanoparticle paste with ultrahigh thermal conductivity and shear strength for high temperature thermal interface material applications. *ACS Applied Materials & Interfaces*, 7(17):9157–9168, 2015.

[12] Jonas Zürcher, Luca Del Carro, Gerd Schlottig, Daniel Nilsen Wright, Astrid-Sofie B. Vardøy, Maaike M. Visser Taklo, and Thomas Brunschwiler. All-copper flip chip interconnects by pressureless and low temperature nanoparticle sintering, 2016.

[13] Yole Development. Igbt market and technology trends, 2015.

[14] Bong Kyun Park, Dongjo Kim, Sunho Jeong, Jooho Moon, and Jang Sub Kim. Direct writing of copper conductive patterns by ink-jet printing. *Thin Solid Films*, 515(19):7706–7711, 2007.

[15] Youngil Lee, Jun-rak Choi, Kwi Jong Lee, E. Nathan Sott, and Donghoon Kim. Large-scale synthesis of copper nanoparticles by chemically controlled reduction for applications of inkjet-printed electronics. *Nanotechnology*, 19(41):415604, 2008.

[16] Toshitaka Ishizaki and Ryota Watanabe. A new one-pot method for the synthesis of cu nanoparticles for low temperature bonding. *Journal of Materials Chemistry*, 22(48):25198–25206, 2012.

[17] A Zinn, R Stoltenberg, AT Fried, J Chang, A Elhawary, J Beddow, and F Chiu. nanocopper based solder-free electronic assembly material. *Nanotechnology*, 2:71–74, 2012.

[18] Dunying Deng, Yunxia Jin, Yuanrong Cheng, Tianke Qi, and Fei Xiao. Copper nanoparticles: aqueous phase synthesis and conductive films fabrication at low sintering temperature. *ACS applied materials & interfaces*, 5(9):3839–3846, 2013.

[19] R. Dharmadasa, M. Jha, D. A. Amos, and T. Druffel. Room temperature synthesis of a copper ink for the intense pulsed light sintering of conductive copper films. *ACS Applied Materials & Interfaces*, 5(24):13227–34, 2013.

[20] Yu Zhang, Pengli Zhu, Gang Li, Tao Zhao, Xianzhu Fu, Rong Sun, Feng Zhou, and Ching-ping Wong. Facile preparation of monodisperse, impurity-free, and antioxidation copper nanoparticles on a large scale for application in conductive ink. *ACS applied materials & interfaces*, 6(1):560–567, 2013.

[21] Na Rae Kim, Kihyun Shin, Inyu Jung, Moonsub Shim, and Hyuck Mo Lee. Ag–cu bimetallic nanoparticles with enhanced resistance to oxidation: A combined experimental and theoretical study. *The Journal of Physical Chemistry C*, 118(45):26324–26331, 2014.

[22] Na Rae Kim, Yung Jong Lee, Changsoo Lee, Jahyun Koo, and Hyuck Mo Lee. Surface modification of oleylamine-capped ag–cu nanoparticles to fabricate low-temperature-sinterable ag–cu nanoink. *Nanotechnology*, 27(34):345706–345712, 2016.

[23] Yoichi Kamikoriyama, Hiroshi Imamura, Atsushi Muramatsu, and Kiyoshi Kanie. Ambient aqueous-phase synthesis of copper nanoparticles and nanopastes with low-temperature sintering and ultra-high bonding abilities. *Scientific Reports*, 9:1–10, 2019.

[24] H. J. Park, Y. Jo, S. S. Lee, S. Y. Lee, Y. Choi, and S. Jeong. Printable thick copper conductors from optically modulated multidimensional particle mixtures. *ACS Applied Materials & Interfaces*, 11(22):20134–20142, 2019.

[25] Wanli Li, Lingying Li, Yue Gao, Dawei Hu, Cai-Fu Li, Hao Zhang, Jinting Jiu, Shijo Nagao, and Katsuaki Suganuma. Highly conductive copper films based on submicron copper particles/copper complex inks for printed electronics: Microstructure, resistivity, oxidation resistance, and long-term stability. *Journal of Alloys and Compounds*, 732:240–247, 2018.

[26] Mai Kanzaki, Yuki Kawaguchi, and Hideya Kawasaki. Fabrication of conductive copper films on flexible polymer substrates by low-temperature sintering of composite cu ink in air. *ACS Applied Materials & Interfaces*, 9(24):20852–20858, 2017.

[27] Yang Zuo, Jun Shen, Jiacheng Xie, and Lu Xiang. Influence of cu micro/nano-particles mixture and surface roughness on the shear strength of cu-cu joints. *Journal of Materials Processing Technology*, 257:250–256, 2018.

[28] Sung-Hyeon Park, Wan-Ho Chung, and Hak-Sung Kim. Temperature changes of copper nanoparticle ink during flash light sintering. *Journal of Materials Processing Technology*, 214(11):2730–2738, 2014.

[29] Hak-Sung Kim, Sanjay R. Dhage, Dong-Eun Shim, and H. Thomas Hahn. Intense pulsed light sintering of copper nanoink for printed electronics. *Applied Physics A*, 97(4):791–798, 2009.

[30] Jin Sung Kang, Hak Sung Kim, Jongeun Ryu, H. Thomas Hahn, Seonhee Jang, and Jae Woo Joung. Inkjet printed electronics using copper nanoparticle ink. *Journal of Materials Science: Materials in Electronics*, 21(11):1213–1220, 2010.

[31] Jongeun Ryu, Hak-Sung Kim, and H. Thomas Hahn. Reactive sintering of copper nanoparticles using intense pulsed light for printed electronics. *Journal of Electronic Materials*, 40(1):42–50, 2010.

[32] Hyun-Jun Hwang, Wan-Ho Chung, and Hak-Sung Kim. In situ monitoring of flash-light sintering of copper nanoparticle ink for printed electronics. *Nanotechnology*, 23(48):485205, 2012.

[33] Sung Jun Joo, Hyun Jun Hwang, and Hak Sung Kim. Highly conductive copper nano/microparticles ink via flash light sintering for printed electronics. *Nanotechnology*, 25(26):265601, 2014.

[34] Wan-Ho Chung, Hyun-Jun Hwang, and Hak-Sung Kim. Flash light sintered copper precursor/nanoparticle pattern with high electrical conductivity and low porosity for printed electronics. *Thin Solid Films*, 580:61–70, 2015.

[35] Hyun-Jun Hwang, Sung-Jun Joo, and Hak-Sung Kim. Copper nanoparticle/multiwalled carbon nanotube composite films with high electrical conductivity and fatigue resistance fabricated via flash light sintering. *ACS applied materials & interfaces*, 7(45):25413–25423, 2015.

[36] Sung Jun Joo, Sung-Hyeon Park, Chang-Jin Moon, and Hak-Sung Kim. A highly reliable copper nanowire/nanoparticle ink pattern with high conductivity on flexible substrate prepared via a flash light-sintering technique. *ACS applied materials & interfaces*, 7(10):5674–5684, 2015.

[37] Y. T. Hwang, W. H. Chung, Y. R. Jang, and Hak-Sung Kim. Intensive plasmonic flash light sintering of copper nanoinks using a band-pass light filter for highly electrically conductive electrodes in printed electronics. *ACS Applied Materials & Interfaces*, 8(13):8591–9, 2016.

[38] Hyun-Jun Hwang, Dug-Joong Kim, Yong-Rae Jang, Yeon-Taek Hwang, I. L. Hyoung Jung, and Hak-Sung Kim. Multi-pulsed flash light sintering of copper nanoparticle pastes on silicon wafer for highly-conductive copper electrodes in crystalline silicon solar cells. *Applied Surface Science*, 462:378–386, 2018.

[39] Chung-Hyeon Ryu, Sung-Jun Joo, and Hak-Sung Kim. Intense pulsed light sintering of cu nano particles/micro particles-ink assisted with heating and vacuum holding of substrate for warpage free printed electronic circuit. *Thin Solid Films*, 675:23–33, 2019.

[40] Matthew S Rager, Tolga Aytug, Gabriel M Veith, and Pooran Joshi. Low-thermal-budget photonic processing of highly conductive cu interconnects based on cuo nanoinks: Potential for flexible printed electronics. *ACS applied materials & interfaces*, 8(3):2441–2448, 2016.

[41] Bongchul Kang, Seungyong Han, Jongsu Kim, Seunghwan Ko, and Minyang Yang. One-step fabrication of copper electrode by laser-induced direct local reduction and agglomeration of copper oxide nanoparticle. *The Journal of Physical Chemistry C*, 115(48):23664–23670, 2011.

[42] C. W. Cheng and J. K. Chen. Femtosecond laser sintering of copper nanoparticles. *Applied Physics A*, 122(4):289, 2016.

[43] Michael Zenou, Oleg Ermak, Amir Saar, and Zvi Kotler. Laser sintering of copper nanoparticles. *Journal of Physics D: Applied Physics*, 47(2):025501, 2013.

[44] Luca Del Carro, Martin Kossatz, Lucas Schnackenberg, Matthias Fettke, Ian Clark, and Thomas Brunschwiler. Laser sintering of dip-based all-copper interconnects. In *2018 IEEE 68th Electronic Components and Technology Conference (ECTC)*, pages 279–286. IEEE.

[45] Young D. Suh, Jinhyeong Kwon, Jinhwan Lee, Habeom Lee, Seongmin Jeong, Dongkwan Kim, Hyunmin Cho, Junyeob Yeo, and Seung Hwan Ko. Maskless fabrication of highly robust, flexible transparent cu conductor by random crack network assisted cu nanoparticle patterning and laser sintering. *Advanced Electronic Materials*, 2(12):1600277, 2016.

[46] Akira Watanabe and Jinguang Cai. Laser direct writing of conductive micropatterns using copper nanoparticle ink toward 3d interconnection. In *2016 IEEE International Conference on Industrial Technology (ICIT)*, pages 1119–1124. IEEE.

[47] W. van Zeijl, Henk, Y. Carisey, Andrei Damian, R. H. Poelma, A. Zinn, Alfred, and Guoqi. Zhang. Metallic nanoparticle based interconnect for heterogeneous 3d integration, 2016.

[48] Xiangdong Liu and Hiroshi Nishikawa. Low-pressure cu-cu bonding using in-situ surface-modified microscale cu particles for power device packaging. *Scripta Materialia*, 120:80–84, 2016.

[49] Jingdong Liu, Hongtao Chen, Hongjun Ji, and Mingyu Li. Highly conductive cu–cu joint formation by low-temperature sintering of formic acid-treated cu nanoparticles. *ACS Applied Materials & Interfaces*, 8(48):33289–33298, 2016.

[50] Qipeng Liu, Xianping Chen, Jie Zhu, Huankun Zhang, S. Zhang, J., G Zhang, J., Lingen Wang, Huaiyu Ye, S. W. Koh, and Guoqi Zhang. The performance of sintered nanocopper interconnections for high temperature device. In *The 19th International Conference on Electronic Packaging Technology (ICEPT)*, pages 1476–1478. IEEE.

[51] Hideo Nakako, Dai Ishikawa, Chie Sugama, Yuki Kawana, Motohiro Negishi, and Yoshinori Ejiri. Sintering copper die-bonding paste curable under pressureless conditions, 2017.

[52] H. Nakako, C. Sugama, Y. Kawana, M. Negishi, Y. Yanaka, D. Ishikawa, and Y. Ejiri. Sintering cu bonding paste: cycle reliability and applications. In *International Exhibition and Conference for Power Electronics, Intelligent Motion, Renewable Energy and Energy Management (PCIM Europe 2018)*, pages 1–6.

[53] Ho Jung, Kwang, Deuk Min, Kyung, Jae Lee, Choong, and Boo Jung, Seung. Pressureless die attach by transient liquid phase sintering of cu nanoparticles and sn-58bi particles assisted by polyvinylpyrrolidone dispersant. *Journal of Alloys and Compounds*, 781:657–663, 2019.

[54] Yue Gao, Wanli Li, Chuantong Chen, Hao Zhang, Jinting Jiu, Caifu Li, Shijo Nagao, and Katsuaki Suganuma. Novel copper particle paste with self-reduction and self-protection characteristics for die attachment of power semiconductor under a nitrogen atmosphere. *Materials and Design*, 160:1265–1272, 2018.

[55] Y. Y. Dai, M. Z. Ng, P. Anantha, Y. D. Lin, Z. G. Li, C. L. Gan, and C. S. Tan. Enhanced copper micro/nano-particle mixed paste sintered at low temperature for 3d interconnects. *Applied Physics Letters*, 108(26):263103, 2016.

[56] Seunghwa Yang, Wonbae Kim, and Maenghyo Cho. Molecular dynamics study on the coalescence kinetics and mechanical behavior of nanoporous structure formed by thermal sintering of cu nanoparticles. *International Journal of Engineering Science*, 123:1–19, 2018.

[57] Bingqing Cheng and Alfonso H. W. Ngan. The crystal structures of sintered copper nanoparticles: A molecular dynamics study. *International Journal of Plasticity*, 47:65–79, 2013.

[58] Yujin Seong, Youngkyu Kim, Randall German, Sungho Kim, Seong-Gon Kim, See Jo Kim, Hak Jun Kim, and Seong Jin Park. Dominant mechanisms of the sintering of copper nano-powders depending on the crystal misalignment. *Computational Materials Science*, 123:164–175, 2016.

[59] Qibin Li, Meng Wang, Yunpei Liang, Liyang Lin, Tao Fu, Peitang Wei, and Tiefeng Peng. Molecular dynamics simulations of aggregation of copper nanoparticles with different heating rates. *Physica E: Low-dimensional Systems and Nanostructures*, 90:137–142, 2017.

[60] C. M. Liu, H. W. Lin, Y. S. Huang, Y. C. Chu, C. Chen, D. R. Lyu, K. N. Chen, and K. N. Tu. Low-temperature direct copper-to-copper bonding enabled by creep on (111) surfaces of nanotwinned cu. *Scientific Reports*, 5:9734–9744, 2015.

[61] J. Mittal and K. L. Lin. Exothermic low temperature sintering of cu nanoparticles. *Materials Characterization*, 109:19–24, 2015.

[62] Di Erick Xu, Jang Baeg Kim, Michael David Hook, Jae Pil Jung, and Michael Mayer. Real time resistance monitoring during sintering of silver paste. *Journal of Alloys and Compounds*, 731:504–514, 2018.

[63] T. Satoh and T. Ishizaki. Enhanced pressure-free bonding using mixture of cu and nio nanoparticles. *Journal of Alloys and Compounds*, 629:118–123, 2015.

[64] Junjie Li, Xing Yu, Tielin Shi, Chaoliang Cheng, Jinhu Fan, Siyi Cheng, Guanglan Liao, and Zirong Tang. Low-temperature and low-pressure cu–cu bonding by highly sinterable cu nanoparticle paste. *Nanoscale Research Letters*, 12(1):255, 2017.

[65] Yang Zuo, Jun Shen, Youdian Hu, and Runhua Gao. Improvement of oxidation resistance and bonding strength of cu nanoparticles solder joints of cu–cu bonding by phosphating the nanoparticle. *Journal of Materials Processing Technology*, 253:27–33, 2018.

[66] Won Yoon, Jeong and Hoon Back, Jong. Effect of sintering conditions on the mechanical strength of cu-sintered joints for high-power applications. *Materials*, 11(11):2105–2117, 2018.

2

MEMS-ENABLED TIME-DEPENDENT CHARACTERIZATION METHODS

2.1. IN-SITU TRANSMISSION ELECTRON MICROSCOPY

TRANSMISSION electron microscopy (TEM) technology uses electrons with high velocity to obtain images with high resolution. Therefore, single atoms in the materials can be observed. It reveals the fundamental mechanism of a certain reaction or process at the atomic level. Considering materials requires various stimuli inside the TEM to trigger the reaction, in situ TEM has become one of the fastest-growing areas where multiple tools and platforms were built. Since there is only limited space inside the TEM holder, and interference to the electron beam from the platform must be limited, solutions which are high integrated, and multi-functionalized should be selected for this application. Therefore, microelectromechanical system (MEMS) attracts many researches attention to enable in-situ environmental TEM characterization platform.

To achieve the goal, there are a number of issues need to be taken in to considerations. In the TEM characterizations, one of the most critical aspects is to ensure electron beam can travel through the sample material without decrease of the image quality. In conventional setup, carbon or copper grids are used as sample holder, since they have minor influence on image quality, while providing support to samples. In a MEMS platform, to reach the best performance, a nanometer-thick suspended membrane structure is often employed as the sample holder. The materials of the this suspended membrane does not react with most of chemicals and nanomaterials. At the meantime, it can withstand enough pressure under liquid and gas to create a customized environment for in-situ observation under TEM. Based on this design, various stimuli elements are designed and integrated in the MEMS system to have a larger variant of experimental environments.

As one of the most important parameters in material studies, temperature control is one of the functions realized the earliest. It is often designed with an embedded microhotplate (MHP), by using bulk micromachining fabrication technologies. This type of MEMS platform is explored by many researchers in recent years. Different metallic heating elements and designs are investigated to achieve wider operation range, high thermal resolution, and temperature uniformity. As shown in Figure 2.1, the temperature range of MHP can reach up to 1300 $^\circ C$ by using a spiral metal heating element on a thin suspended SiNx membrane [1]. The four-point measurement method is employed to ensure precise temperature control. Molybdenum is chosen to be the heater material due to its high melting temperature and process compatibility compared with Pt. It is suitable for high-temperature MEMS MHP [2], which operates above 500 $^\circ C$. With precise temperature control, direct observation of material dynamic response can be possible under TEM [3–8]. As shown in Figure 2.2, various temperature stages were applied by MHP, where MOS_2 samples could experience growth evolution [7]. The fundamental structural changes while annealing can be captured and investigated. In the figure, the decomposition and growth process with detailed crystalline structures and related temperature conditions can be related precisely.

Furthermore, other stimuli, including gas [9, 10], liquid, optics [11] and mechanical tilting [12], are also embedded in the MEMS platforms with different design and fabrication technologies, for in-situ materials study. Since TEM requires an ultra-high vacuum environment, gas and liquid environments are among the most challenging devices. To prevent TEM chamber contamination, gas and liquid need to be sealed in a

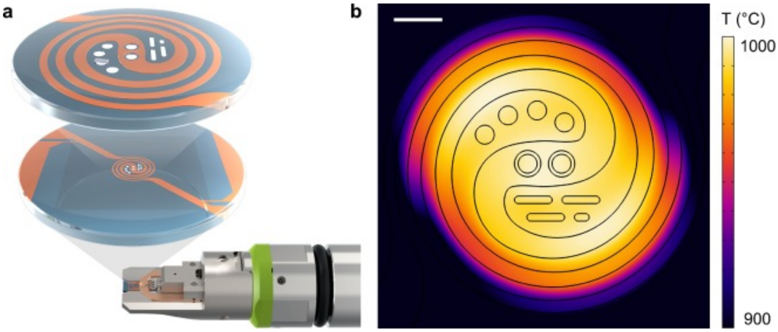

Figure 2.1: One of the MHP embedded MEMS platform under TEM [1]. (a) Overview of the MEMS chip in TEM holder, with spiral heating elements. (b) Finite element simulation of the temperature distribution of the heating area, reaching 1000 $^{\circ}C$.

well-confined chamber to ensure an electron beam working environment. As in Dai's work, atmospheric pressure was created within the MEMS platform under STEM by using a dedicated gas cell with TEM windows [9]. With these specialized characterization tools for $in-situ$ TEM, the possibilities to study nanomaterials and 2D materials are significantly expanded. Structural and compositions evolution of materials, including atomic movement, interfaces, and dislocations, can be captured $in-situ$, with various testing conditions [13].

2.2. $In-situ$ SCANNING ELECTRON MICROSCOPY

BESIDES atomic level information from structures of materials at atomic-level, scanning electron microscopy (SEM) focuses mostly on the morphology of the materials. Surface structure study can be performed with great details with high-resolution SEM (HRSEM). In the meantime, comparing to TEM, more sample size and thickness can fit the SEM environment. Combined with the benefits of MEMS devices, a larger design window can be explored inside SEM environment.

Since mechanical property is one of the essential property of material, SEM can explicit precise information about material fracture mechanism, interface adhesive and elastic properties. In order to study microstructure under mechanical loading, precise control of the applied force and measurement are required. Miniaturized MEMS platform can provide high-resolution of force load by accurate control of the actuators. This platform can have wide applications in electronics and energy fields. Actuators are usually employed in the MEMS platform design to accurately control the force and displacement [14–16]. The thin-film, or even 2D materials, is attached to the surface platform. Ramachandramoorthy employed a MEMS mechanical test platform (Figure 2.3) to study the silver nanowires crystallography change under high strain rate, in in-situ SEM [15]. Due to the large operating range and fast response time, 2 orders of magnitude higher strain rate could be performed on a single silver nanowire. It was revealed that silver nanowire experienced a brittle-to-ductile transition of failure mode at a certain threshold strain rate. TEM observation and molecular dynamic (MD) simulation are combined to confirm the fundamental mechanism of this material failure mode. By implementing

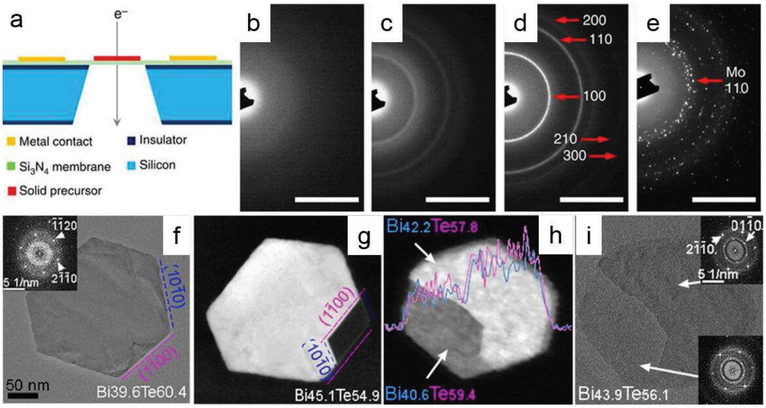

Figure 2.2: In situ thermal TEM study of MoS_2 growth evolution and Bi_2Te_3 decomposition [7]. (a) Schematic of the experimental setup of $in-situ$ TEM thermal stage. (b – e) SAED patterns of MoS_2 growth evolution with increasing temperature: 25 $^\circ C$, 400 $^\circ C$, 780 $^\circ C$, and 900 $^\circ C$. Scale bars are 5 nm. (f – i) Sublimation procedure of Bi_2Te_3 nanocrystals annealing temperature of 350 and 400 $^\circ C$. (f) TEM images of a Bi_2Te_3 nanocrystal before thermal annealing and its corresponding FFT in the inset. (g – i) Three STEM images of partially sublimated Bi_2Te_3 nanocrystals at 350 $^\circ C$.

accurate force and measurement, material behavior can be observed simultaneously under SEM. Therefore the dynamic mechanical response and properties can be obtained. Elastic property and fracture behavior, interface energy, cleavage of a variety of materials can be studied by applying this method.

With assistance of MEMS devices, the capability of electron microscopes is strengthened and enlarged. This opens much more possibilities in fundamental understanding of materials behavior and properties, with dynamic stimuli and responses. However, sample preparation of some samples is always challenging. It sometimes requires a transfer process or advanced atomic force microscopy (AFM), which can place the film samples on the required position of the testing platform. Defects, impurities and layer numbers of the testing samples need to be considered in characterizations and analyzes. This can raise the number of experiments and possible variables, which may have an impact on the final data acquisition.

2.3. ULTRA-FAST X-RAY SCANNING

As one of the most used material characterization methods, X-ray has a much longer history employed for medical purpose and material studies [17]. Therefore, a number of different technologies are developed in the past, based on crystallography of materials [18–20]. Among these methods, X-ray diffraction is one of the most widely used method. For crystalline materials, different lattice sizes can be utilized by XRD to provide quantitative information about their crystallography [21], inner stress, and phase changes. Comparing to electron microscopy discussed above, which requires strictly an ultra-high vacuum working environment, XRD can work in the ambient atmosphere. Additionally, X-ray is penetrative, comparing to the electron beam. It can penetrate a few micrometers, depends on the specific materials. These features offer much more flexi-

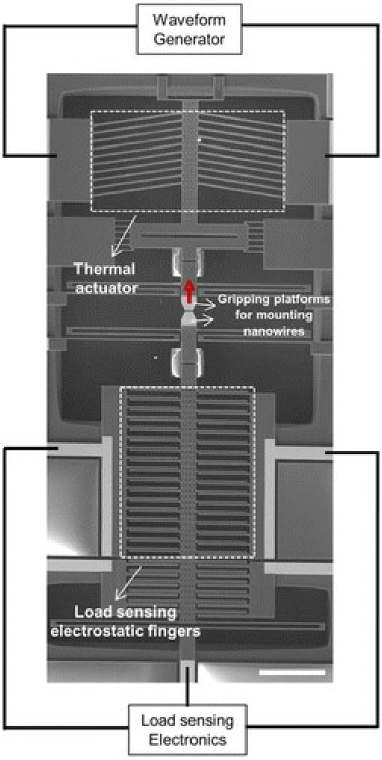

Figure 2.3: Schematic of MEMS mechanical test platform [15]. The red arrow indicates the actuation direction, with a scale bar of 250 mm.

bility in sample size requirements and preparation methods. The fundamental principle of XRD is Bragg's law as depicted in Figure 2.4, which reveals precisely the lattice parameter of the material in terms of diffraction angles [22]. To collect sufficient diffraction patterns, an X-ray diffractometer needs to scan at a wide angle range. Therefore ,this process takes a few minutes to hours to finish a single scan, which is time-consuming. To overcome this problem and improve the diffraction signal further, a synchrotron X-ray diffractometer is introduced in this field to enable ultra-fast XRD, even in-situ XRD to detect the kinetics of specific processes or reactions quantitatively. This method is applied widely in the area of nanoparticles study, lithium batteries and catalyst [23–27].

Similar to the situation in in-situ electron microscopy, more stimuli for the process are in demand to be embedded in the instrument set-up. Consequently, laser pulse, as an ultrafast heating source down to femtosecond, is introduced in the synchrotron X-ray diffractometer to give precise temperature control [28]. In this condition, the XRD method is called time-resolved XRD (TRXRD), where it can be used as a probe to visualize the transition change of material with an extremely short time interval. With advanced laser beam and short X-ray pulses, atomic-scale phenomena can be observed [29]. Rose-Petruck reported a 100-ps coherent acoustic pulse, which generated from op-

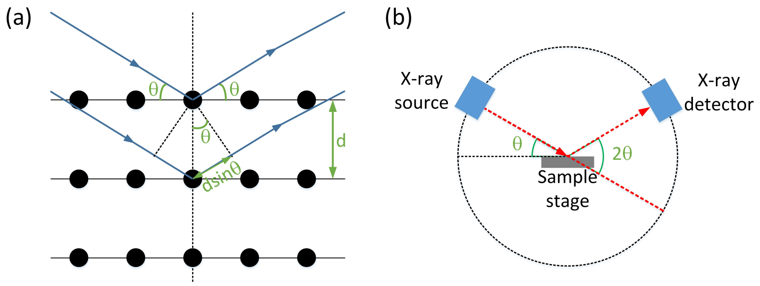

Figure 2.4: (a) Bragg's law. (b) Schematic of X-ray diffractometer working principle.

tical excitation of a crystal surface, with a great agreement between quantitative results and theoretical prediction. These results demonstrate that atomic-level dynamics can be possibly observed and analyzed with the TRXRD method. Later on, more profound TRXRD studies about dynamic material processes are conducted with a laser pulse and synchrotron X-ray diffractometer [25, 30–32]. Beyond conventional crystallography, synchrontron X-ray is also employed to more complex 3D structure like protein [33]. Based on the diffractive information, the electro density of the complex structure can be rebuilt, with assistance of molecular modeling in spatial dimensions. Thus, biomaterial structures, including human chromosome, bone, and protein, can be detected and visualized by using X-ray diffractions.

With large, accurate material information and wide applications, XRD and related instrument do not attract too much attention from MEMS development, as electron microscopy. A laser pulse can bring time interval down to pico-second, but it can only provide heat or optical excitations. Furthermore, synchrotron or coherent X-ray diffractometers are extremely sophisticated instruments, which can consume a large amount of human and economic resources. Figure 2.5 is one of the accurate kinetic studies about material evolution using in-situ XRD with thermal and gas stimuli [23]. In this study, an in-house reactor chamber was created, and installed on the XRD instrument. Gas flow and temperature were accurately calibrated and controlled. These functions can be integrated using MEMS platforms, as developed for $in-situ$ EM applications. These platforms have advantages in the flexibility of both function and size. Sample stimuli and characterization can be integrated and conducted at the same time. High level of integration and miniaturization of the MEMS characterization platform can expand the possibility of frontier research, cut off experimental expense, and add much more value to the conventional XRD, which can be accessed by more researchers.

References

[1] J. Tijn Van Omme, Marina Zakhozheva, Ronald G. Spruit, Mariya Sholkina, and H. Hugo Pérez Garza. Advanced microheater for in situ transmission electron microscopy; enabling unexplored analytical studies and extreme spatial stability. *Ultramicroscopy*, 192:14–20, 2018.

[2] L. Mele, F. Santagata, E. Iervolino, M. Mihailovic, T. Rossi, A. T. Tran, H. Schelle-

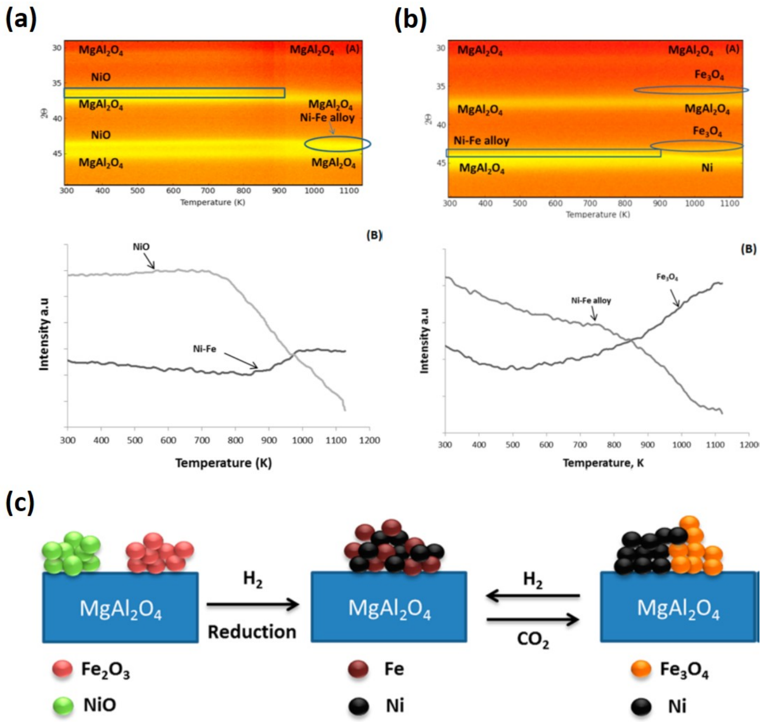

Figure 2.5: (a) In-situ 2D XRD patterns and integral intensity variation of NiO and FeNi peak, in 10% H_2 flow, from room temperature to 1123 K. (b) $In-situ$ 2D XRD patterns and integral intensity variation of NiO and FeNi peak, in 100% CO_2 flow, from room temperature to 1123 K. (c) Schematic diagram of $Fe-Ni$ alloy formation and decomposition under different gases [23]

vis, J. F. Creemer, and P. M. Sarro. A molybdenum mems microhotplate for high-temperature operation. *Sensors and Actuators A: Physical*, 188:173–180, 2012.

[3] Z. Li, Z. A. Li, S. Sun, D. Zheng, H. Wang, H. Tian, H. Yang, X. Bai, and J. Li. Direct observation of inner-layer inward contractions of multiwalled boron nitride nanotubes upon in situ heating. *Nanomaterials (Basel)*, 8(2), 2018.

[4] J. A. Watts, M. W. Fay, G. A. Rance, P. D. Brown, and A. N. Khlobystov. Formation of hollow carbon nanoshells from thiol stabilised silver nanoparticles via heat treatment. *Carbon*, 139:538–544, 2018.

[5] X. Xie, J. Tu, Q. Y. Ge, Z. H. Lu, and L. T. Sun. Nanoscale observation of conformational transformation of dna polymerase via in-situ liquid-cell transmission electron microscopy. *Journal of Biomedical Nanotechnology*, 15(5):1106–1111, 2019.

[6] R. A. Bernal, T. Filleter, J. G. Connell, K. Sohn, J. X. Huang, L. J. Lauhon, and H. D. Espinosa. In situ electron microscopy four-point electromechanical characterization of freestanding metallic and semiconducting nanowires. *Small*, 10(4):725–733, 2014.

[7] Linfeng Fei, Shuijin Lei, Wei-Bing Zhang, Wei Lu, Ziyuan Lin, Chi Hang Lam, Yang Chai, and Yu Wang. Direct tem observations of growth mechanisms of two-dimensional mos2 flakes. *Nature Communications*, 7:12206, 2016.

[8] Charles D. Amos, Manuel A. Roldan, Maria Varela, John B. Goodenough, and Paulo J. Ferreira. Revealing the reconstructed surface of li[mn2]o4. *Nano Letters*, 16(5):2899–2906, 2016.

[9] Sheng Dai, Shuyi Zhang, George W. Graham, and Xiaoqing Pan. In situ scanning transmission electron microscopy with atomic resolution under atmospheric pressure. *Microscopy Today*, 27(03):16–21, 2019.

[10] H. H. Perez-Garza, D. Morsink, J. Xu, M. Sholkina, Y. Pivak, M. Pen, S. van Weperen, Q. Xu, and Ieee. *The "Climate" System: Nano-Reactor for in-situ analysis of solid-gas interactions inside the TEM.* International Conference on Nano-Micro Engineered and Molecular Systems NEMS. 2016.

[11] Songhua Cai, Chenyi Gu, Yifan Wei, Min Gu, Xiaoqing Pan, and Peng Wang. Development of in situ optical–electrical mems platform for semiconductor characterization. *Ultramicroscopy*, 194:57–63, 2018.

[12] R. A. Bernal, R. Ramachandramoorthy, and H. D. Espinosa. Double-tilt in situ tem holder with multiple electrical contacts and its application in mems-based mechanical testing of nanomaterials. *Ultramicroscopy*, 156:23–28, 2015.

[13] C. Luo, C. L. Wang, X. Wu, J. Zhang, and J. H. Chu. In situ transmission electron microscopy characterization and manipulation of two-dimensional layered materials beyond graphene. *Small*, 13(35), 2017.

[14] Y. Zhu and H. D. Espinosa. An electromechanical material testing system for in situ electron microscopy and applications. *Proceedings of the National Academy of Sciences*, 102(41):14503–14508, 2005.

[15] R. Ramachandramoorthy, W. Gao, R. Bernal, and H. Espinosa. High strain rate tensile testing of silver nanowires: Rate-dependent brittle-to-ductile transition. *Nano Letters*, 16(1):255–263, 2016.

[16] X. Li, M. Sun, C. X. Shan, Q. Chen, and X. L. Wei. Mechanical properties of 2d materials studied by in situ microscopy techniques. *Advanced Materials Interfaces*, 5(5), 2018.

[17] W Robert Nitske. *The life of Wilhelm Conrad Röntgen, discoverer of the X ray*. University of Arizona Press, 1971.

[18] WILLIAM E FORD. Mineralogy. 1932.

[19] André Guinier. *X-ray crystallographic technology*. Hilger and Watts, 1952.

[20] Challapalli Suryanarayana and M Grant Norton. *X-ray diffraction: a practical approach*. Springer Science & Business Media, 2013.

[21] Alden B Greilinger. A back-reflection laue method for determining crystal orientation. *Zeitschrift für Kristallographie-Crystalline Materials*, 91(1-6):424–432, 1935.

[22] William Lawrence Bragg. The specular reflection of x-rays. *Nature*, 90(2250):410–410, 1912.

[23] S. A. Theofanidis, V. V. Galvita, H. Poelman, and G. B. Marin. Enhanced carbon-resistant dry reforming fe-ni catalyst: Role of fe. *ACS Catalysis*, 5(5):3028–3039, 2015.

[24] Mathias K. Christensen, Jette Katja Mathiesen, Søren Bredmose Simonsen, and Poul Norby. Transformation and migration in secondary zinc–air batteries studied by in situ synchrotron x-ray diffraction and x-ray tomography. *Journal of Materials Chemistry A*, 7(11):6459–6466, 2019.

[25] A. L. Bugaev, O. A. Usoltsev, A. Lazzarini, K. A. Lomachenko, A. A. Guda, R. Pellegrini, M. Carosso, J. G. Vitillo, E. Groppo, J. A. van Bokhoven, A. V. Soldatov, and C. Lamberti. Time-resolved operando studies of carbon supported pd nanoparticles under hydrogenation reactions by x-ray diffraction and absorption. *Faraday Discuss*, 208:187–205, 2018.

[26] A. M. A. Leguy, Y. Hu, M. Campoy-Quiles, M. I. Alonso, O. J. Weber, P. Azarhoosh, M. van Schilfgaarde, M. T. Weller, T. Bein, J. Nelson, P. Docampo, and P. R. F. Barnes. Reversible hydration of ch(3)nh(3)pbl(3) in films, single crystals, and solar cells. *Chemistry of Materials*, 27(9):3397–3407, 2015.

[27] S. Mhin, K. Nittala, C. Cozzan, K. Kim, D. S. Robinson, L. M. Sanchez, R. G. Polcawich, and J. L. Jones. Role of the pbtio3 seed layer on the crystallization behavior of pzt thin films. *Journal of the American Ceramic Society*, 98(5):1407–1412, 2015.

[28] Christian Rischel, Antoine Rousse, Ingo Uschmann, Pierre-Antoine Albouy, Jean-Paul Geindre, Patrick Audebert, Jean-Claude Gauthier, Eckhart Fröster, Jean-Louis Martin, and André Antonetti. Femtosecond time-resolved x-ray diffraction from laser-heated organic films. *Nature*, 390:490, 1997.

[29] Christoph Rose-Petruck, Ralph Jimenez, Ting Guo, Andrea Cavalleri, Craig W. Siders, Ferenc Rksi, Jeff A. Squier, Barry C. Walker, Kent R. Wilson, and Christopher P. J. Barty. Picosecond–milliångström lattice dynamics measured by ultrafast x-ray diffraction. *Nature*, 398(6725):310–312, 1999.

[30] PK Lambert, CJ Hustedt, KS Vecchio, EL Huskins, DT Casem, SM Gruner, MW Tate, HT Philipp, AR Woll, and P Purohit. Time-resolved x-ray diffraction techniques for bulk polycrystalline materials under dynamic loading. *Review of Scientific Instruments*, 85(9):1–7, 2014.

[31] A. E. Gleason, C. A. Bolme, H. J. Lee, B. Nagler, E. Galtier, D. Milathianaki, J. Hawreliak, R. G. Kraus, J. H. Eggert, D. E. Fratanduono, G. W. Collins, R. Sandberg, W. Yang, and W. L. Mao. Ultrafast visualization of crystallization and grain growth in shock-compressed sio2. *Nature Communications*, 6, 2015.

[32] Kerry Simmance, Wouter van Beek, and Gopinathan Sankar. Time resolved in situ x-ray diffraction study of crystallisation processes of large pore nanoporous aluminophosphate materials. *Faraday Discussions*, 177(0):237–247, 2015.

[33] J. Miao, T. Ishikawa, I. K. Robinson, and M. M. Murnane. Beyond crystallography: Diffractive imaging using coherent x-ray light sources. *Science*, 348(6234):530–535, 2015.

3

MEMS ENABLED FAST TIME-RESOLVED NANOMATERIAL CHARACTERIZATION PLATFORM

It is essential for material design and process development to understand the sintering mechanism of micron-thickness Cu NPs. However, there are limited methods and tools for the time-dependent study of Cu NPs sintering process. In this chapter, a novel MEMS(micro-electro-mechanical system)-based fast time-resolved X-ray diffraction (TRXRD) characterization platform for nanomaterial is introduced. The devices were designed, fabricated, and investigated. The design employs a thick silicon oxide structure for lateral thermal isolation. The device and its system have a 60 ms and 50ms minimum heat pulse width, uniform temperature distribution, and variant gas environments. Four-point measurement electrodes structure is also integrated into the design, for in-situ electrical resistance measurement. The investigation results show that the fabricated devices and systems can be applied in the time-dependent study of Cu paste sintering.

Parts of this chapter has been published in:
B. Zhang, J. Wei, A. J. Böttger, H. W. van Zeijl, P. M. Sarro, and G. Zhang. MEMS enabled fast time-resolved x-ray diffraction characterization platform for copper NP sintering in heterogeneous integration applications. In 2019 20th International Conference on Solid-State Sensors, Actuators and Mi-crosystems & Eurosensors XXXIII (TRANSDUCERS & EUROSENSORS XXXIII),pages 1772–1775. [1]

3.1. INTRODUCTION

LOW temperature sintering of metallic nanoparticle (NP) paste, such as Cu NP-based paste, has a great potential in the interconnect of heterogeneous integration [2–4] and power electronics packaging. Ag NP-based paste is developed and applied and applied for high performance and reliability driven applications [5–8]. Considering the cost-effective factor and potential electromigration issue [9, 10], Cu recently became one of the most promising materials in novel packaging applications [11–14]. Many research works were done to optimize the low temperature sintering process and material synthesis. To achieve these goals, experimental time-dependent insight of the sintering process is essential [15–18]. However, related time-dependent study is limitedly reported, even for Ag NP-based paste, which is already developed and applied in high power applications. Considering the experimental conditions and specimen geometry, the results obtained might be difficult to be applied in the envisioned applications. As an emerging material and technology, more detailed and systematic study of Cu NP-based paste sintering process under real application conditions needs to be performed.

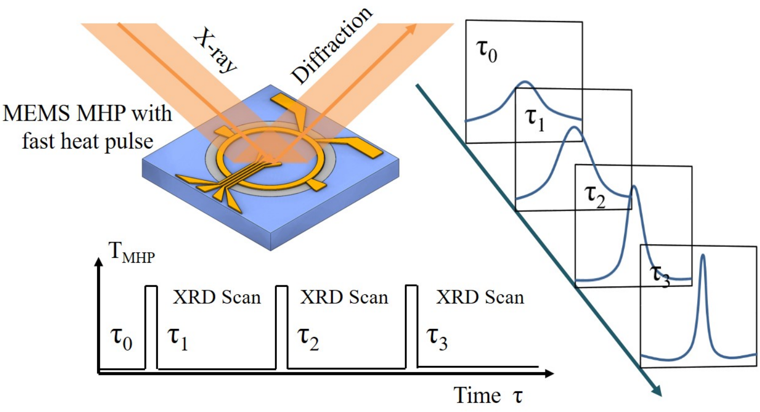

Figure 3.1: Concept of MEMS enabled time-resolved X-ray diffraction (TRXRD) for nanomaterial characterization.

To mimic and study the sintering process as in real application, Cu NP-based paste (particle size <100 nm) needs to be processed with micrometer thickness, in a gas environment. Transmission electron microscope (TEM) reveals particle behavior at the atomic level [18–20]. However, as summarized in chapter 2, the obtained information has limitation to be applied in real applications. On the other hand, time-dependent X-ray diffraction study is currently too sophisticated for most of researchers. To fulfill this need, a MEMS-enabled fast time-resolved XRD (TRXRD) method is proposed in this paper to obtain insight knowledge about Cu NP-based paste sintering.

TRXRD is defined as a method for detecting dynamic position and intensity of diffracted XRD pattern as a function of time, by using a short pulse X-ray beam at the sample [17]. High-intensity synchrotron radiation beams enable the necessary time interval to reveal intermediate states of materials. Instead of using short pulses of synchrotron

X-ray beam, a MEMS micro-hotplate (MHP) device is introduced to enable TRXRD in milli-seconds (ms), using conventional XRD facilities. Fine, accurate XRD scans are performed during frozen states (Figure 3.1). By switching alternatively between activated and frozen states, a series of XRD patterns, thus material details, for a specific dynamic process can be obtained as a function of time. To enable a milli-seconds TRXRD, the device contains an on-chip MHP to enable fast temperature control (typically tens of milli-seconds) on micro-sized samples placed on top of the MHP surface. This allows fast switching of temperature-sensitive reactions between activated and frozen states.

3.2. THERMAL DESIGN THEORY

THE governing equation of heat conduction, in a homogeneous, isotropic solid, is Fourier's first law of heat conduction [21]

$$\vec{j} = -\kappa \cdot \nabla T \quad (W/m^2) \tag{3.1}$$

Where $j \rightharpoonup$ is the heat flux vector represents the heat flow per unit time, per unit area of the isothermal surface in the direction of decreasing temperature. ∇T is the temperature gradient vector, normal to the isothermal surface, and κ is the heat conductivity of the material. In the case of MHP, the internal energy is provided to maintain the temperature constant. The volumetric rate of energy generation $p(W/m^3)$ is required. Additionally, the rate of energy storage in the material in a unit volume is defined as volume specific heat, $c_v(J/(kg \cdot K))$. In solid, $c_v = c_p = c$, and the total energy stored in the unit volume of material is denoted as $u(J/m^3)$. Before the MHP reaches a steady state, the net rate of heat generated plus the net rate of heat conducted per unit volume is equal to the net rate of energy stored per differential volume. Thus, the dynamic differential equation form, according to Fourier's second law, can be written as:

$$p + \nabla \cdot \vec{j} = \frac{\partial u}{\partial t} = \rho c \frac{\partial T}{\partial t} \tag{3.2}$$

$$-\nabla \cdot (\kappa \cdot \nabla T) + p = \rho c \frac{\partial T}{\partial t} \tag{3.3}$$

Where $\rho(kg/m^3)$ is the density of the material. At a static state, where $\partial T/\partial t = 0$, the heat conduction equation is:

$$\nabla \cdot (\kappa \cdot \nabla T) = p \tag{3.4}$$

In their integration form, surface heat flux and energy generation are integrated in the entire surface area and volume respectively:

$$\int_V \nabla \vec{j} \cdot dV + \int_v p \cdot dV = \rho c \int_v \frac{\partial T}{\partial t} \cdot dV \tag{3.5}$$

Taking only the linear regime of conduction,

$$-\kappa \cdot \Delta T + P = C \cdot \frac{d}{dt} \Delta T \tag{3.6}$$

At the static state, where $dT/dt = 0$, the heat conduction equation is:

$$-\kappa \cdot \Delta T = P = V_{heat} \cdot I_{heat} \tag{3.7}$$

In the case of a transducer-based MHP, this heat flow is provided by heating current, I_{heat}, and voltage, V_{heat}. It indicates that the power consumption of the device has a linear relationship with temperature change.

The solution for dynamic differential conduction is:

$$Tt = \Delta T_f (1 - e^{-\frac{t}{\tau}}) \tag{3.8}$$

Where $\Delta T_f = T_f - T_0$, which T_f denotes to the final temperature, and T_0 denotest to the initial temperature. Thus, the thermal time constant of the device can be written as:

$$\tau_0 = \frac{C}{K} = CR \tag{3.9}$$

Where the heat resistance of the device is denoted as R. The thermal time constant can be affected by temperature, as power consumption, thermal capacity and resistance is temperature-dependent. In the design proposed in this chapter, a 50 μm-thick Si membrane is employed as the main material of MHP. It can provide uniform temperature distribution in the whole material detection area. Silicon oxide outer ring is applied as the lateral thermal isolation structure.

3.3. MHP WITH A THICK SILICON OXIDE THERMAL ISOLATION

3.3.1. STRUCTURAL DESIGN

TYPICALLY, the size of an MHP with suspended is below 0.5 mm in diameter, depending on the applications. A temperature difference of 30 - 50 $^\circ C$ from edge to the center, when the MHP temperature is between 300 - 400 $^\circ C$, is generated [22–24]. For a sintering process study under TRXRD, a 0.5 mm diameter heating area hardly provides enough signal for detection. In addition, Cu NP-based paste sintering process initiates below 300 $^\circ C$. It is a temperature-sensitive process. Therefore, a temperature variation of more than 10% can have a strong effect on the final characterization results.

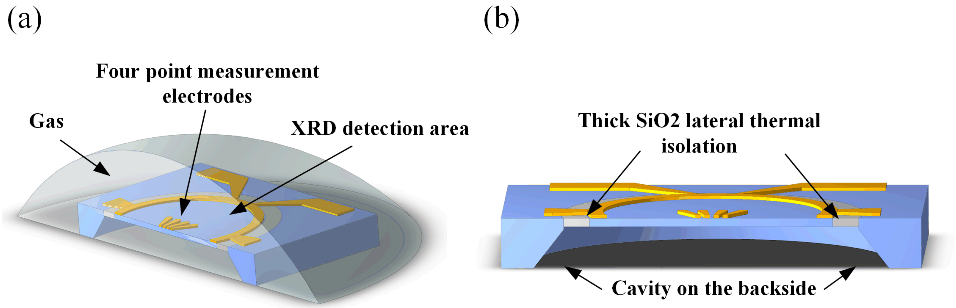

Figure 3.2: Schematic drawing of MHP structures

Table 3.1: Simulated MHP average temperatures and deviations in percentage of average temperatures.

Power (W)	T_{avg} ($^\circ C$)	T_{max} ($^\circ C$)	T_{min} ($^\circ C$)	Deviation (%)
0.1	104.44	106.39	102.95	1.35
0.2	188.67	192.56	185.70	1.49
0.3	272.83	278.67	268.37	1.55
0.4	356.96	364.73	351.01	1.57
0.5	441.06	450.78	433.63	1.59
0.6	525.15	536.82	516.24	1.60
0.7	609.32	622.85	598.84	1.61
0.8	693.32	708.87	681.44	1.62

To minimize the influence from MHP to the XRD detection, the heating element needs to be placed outside of the XRD detection area (1 mm in diameter for typical X-ray beam size). Therefore, the center part of the MHP may have a temperature drop due to convection and thermal radiation losses. To ensure a homogeneous reaction across a large XRD detection area, a sample support layer with good thermal conduction property is required. Due to the high thermal conductivity [25], a 50 μm-thick single-crystal silicon membrane is chosen as the support layer (Figure 3.2). Meanwhile, a thick oxide ring as horizontal thermal isolation is integrated along the edge of the MHP area [26] to constrain temperature uniformity within the area, as well as to reduce power consumption. Thus, by accurate control of heating power, the device can switch between activated and frozen states.

3.3.2. FUNCTION VALIDATION WITH SIMULATIONS

THERMAL SIMULATIONS

To evaluate the temperature distribution and corresponding thermal stress along the MHP area, a finite element modeling (FEM) simulation was performed using COMSOL Multiphysics, v5.2. In the simulation, half of the device was analyzed due to symmetry of the structure. A certain amount of power was input in the metal line area of MHP, as heat source. External air convection was considered using the default value from the software database. In the thermo-mechanical simulation, the bottom of surface of the device is set as fixed, and the temperature is 25 $^\circ C$, since it will be mounted on a much larger substrate that with fixed position and constant temperature. In Table 3.1, a series of input powers from 0.1 - 0.8 W, with a step value of 0.1 W were input. Simulated average temperatures and deviations (in the percentage of average temperatures) under various power supplies are presented. As the average temperature of MHP increased to around 700 $^\circ C$, deviation from the average value is only 1.62%. During sintering study of Cu NPs, the maximum operating temperature is 300 °. MHP has a deviation less than 1.57% (< 4.71 $^\circ C$).

Furthermore, Figure 3.3 (a) and (b) show the simulated temperature distributions, when the input heat power to MHP temperature was 0.5 W. The simulated average temperature on the MHP area was 441.06 $^\circ C$. Simulated temperature distribution and tem-

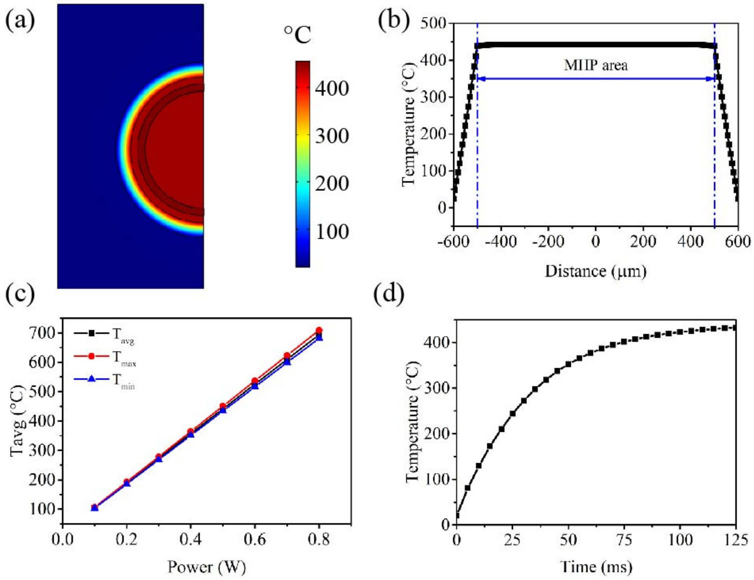

Figure 3.3: (a) Simulated temperature distribution of MHP, when the 0.5 *W* power was input. (b) Simulated temperature profile along the center of MHP. (c) Simulated average, maximum and minimum temperatures with variant of input heat power. (d) Device temperature response with 0.5 *W* heat power.

perature profile on the centerline of MHP are shown respectively. Figure 3.3 d presents the simulated results of the device temperature response. A 0.5 *W* heat power pulse was given to the device. The average temperature on the MHP was simulated with 5 ms time interval. In Figure 3.3 a, it shows a uniform temperature distribution within X-ray detection area (1 mm in diameter). On the edge of MHP, there is a rapid temperature drop in a short distance. That is the effect of the oxide thermal isolation structure. In Figure 3.3 b, temperature profile on the centerline of MHP is presented from the simulated result in Figure 3.3 a. In the 1 mm diameter MHP area, which is the X-ray detection area, temperature profile is less than 2%. From the edge of MHP, a sharp drop due to lateral thermal isolation structure can be observed. Additionally, as in Figure 3.3 c, the deviation of temperature distribution remains low at different operation temperatures. Thus, the designed structure can ensure a uniform temperature distribution within the sintering temperature range. The temperature uniformity of this device achieves requirements for the sintering process study. The time for the MHP to reach 90% of total temperature change is considered as temperature response time. According to the device simulation results, as in Figure 3.3 c, it takes approximately 75 ms for the MHP to achieve 90% of the target temperature. Thus, the device can have a fast switch between active and frozen states during the TRXRD experiments, comparing to the time scale of sintering process.

MECHANICAL SIMULATIONS

Since the 50 μm-thick Si membrane is constrained by thick-oxide lateral thermal isolation structure, the thermal stress due to coefficient of thermal expansion (CTE) mis-

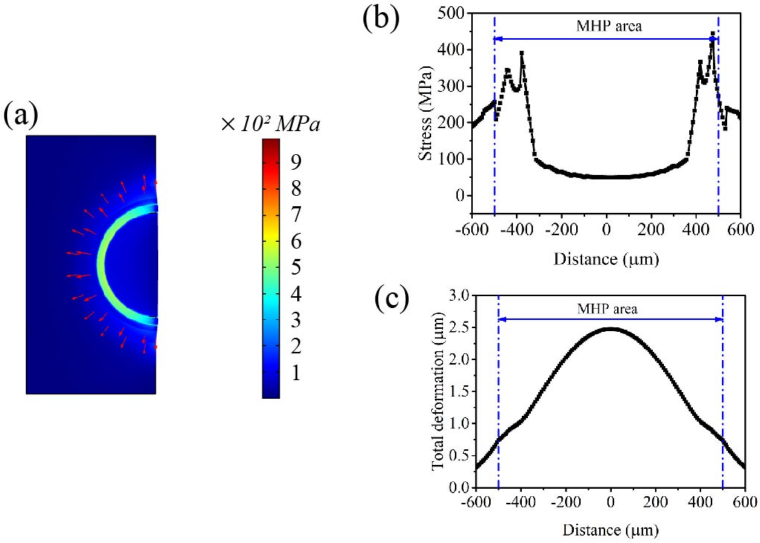

Figure 3.4: Simulated results of the device when the MHP average temperature is 441.06 °C. (a) Thermal stress along MHP. Red arrows present deformation directions. (b) Simulated stress profile on the centerline of MHP. (c) Corresponding total deformation profile on the centerline of MHP.

match at high temperature may have an impact on MHP performance. Therefore, it is essential to evaluate the mechanical performance of MHP at a raised temperature. Figure 3.4 shows the thermal stress and total deformation along the MHP area when the MHP temperature is 441.06 °C. As shown in Figure 3.4 a, there is a stress concentrated area at the place where metal lines are embedded. It could be caused at interface between the metal lines and the silicon membrane of MHP, since there is a large difference of coefficient of temperature expansion of metal (Pt in this case) and silicon. Figure 3.4 b presents the stress profile along the middle line of MHP. The maximum stress can reach 400 MPa on the MHP. Considering the fracture strength of single-crystalline silicon, 400 MPa of concentrated stress and large deformation (Figure 3.4 c) may lead to crack initiation under this condition [27]. To avoid the risk of device damage and failure due to thermal stress concentration, the maximum operating temperature of the device is therefore limited to 400 °C.

3.3.3. Microfabrication

A bulk-micromachining process is developed for device fabrication in Figure 3.5. A 525 μm thick Si wafer was used as a starting material (Figure 3.5 a). A thick silicon oxide lateral thermal isolation structure (50 μm deep, 100 μm wide) is fabricated using deep reactive ion etching (DRIE) and wet thermal oxidation (Figure 3.5 b). After the lateral thermal isolation structure was obtained, 300 nm of SiNx was deposited by low pressure chemical vapor deposition (LPCVD). It is used as an isolation layer between Si and Pt, diffusion layer between Si and Cu NP - based and as a hard mask for Si cavity etching on the backside (Figure 3.5 c). A 200 nm Pt metal layer, with 20 nm Ta as an ad-

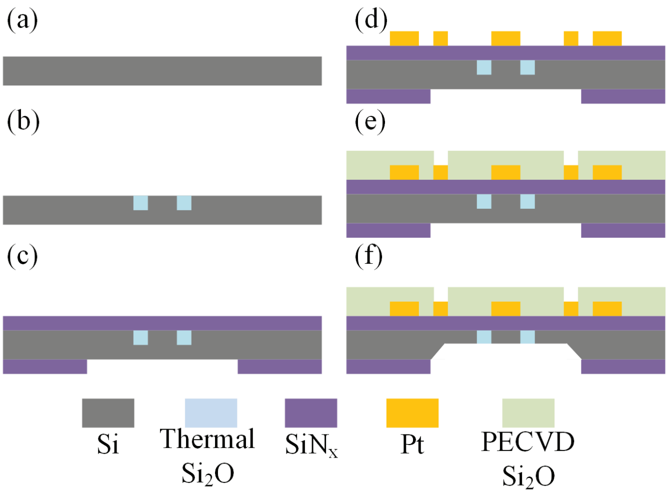

Figure 3.5: The main steps of the fabrication process. (a - b) Formation of thick silicon oxide blocks for thermal isolation by using DRIE and thermal oxidation. (c - d) Surface smoothening and metallization. (e) Passivation layer deposition and contact pads opening. (f) Backside cavity etching in a KOH solution.

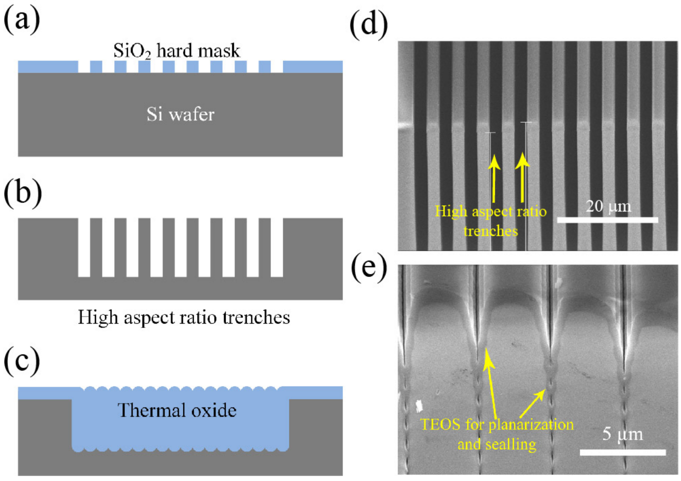

Figure 3.6: (a – c) Main fabrication steps of lateral thermal oxide isolation structures. SEM cross-section images of (d) high aspect ratio trenches after DIRE, and (e) thick oxide blocks after TEOS planarization and sealing used for lateral thermal isolation.

hesion layer, was used as the MHP metal layer. Ta/Pt layer was evaporated and patterned by the lift-off method (Figure 3.5 d). A SiO_2 passivation layer was deposited by PECVD. Contact pads were opened by using reactive ion etching, with photoresist as a mask layer (Figure 3.5 e). Si cavity on the backside was etched by isotropic wet etching with KOH solution (Figure 3.5 f). The etching was stopped as soon as it reaches the predefined 50

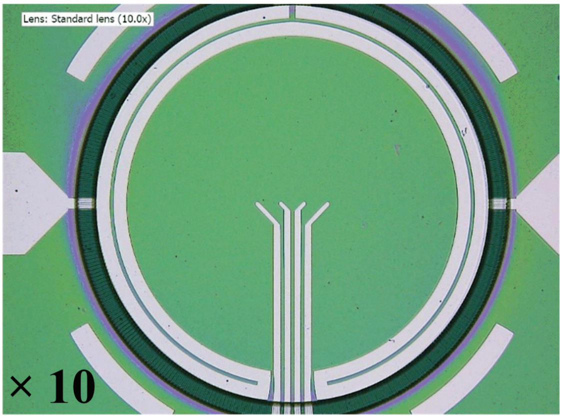

Figure 3.7: Optical image (close-up) of a fabricated MHP.

μm-thick SiO_2 thermal isolation block. A 50 μm-thick Si membrane was then created. An optical image fabricated device is shown in Figure 3.7.

Figure 3.6 a–c illustrates the main steps to fabricate lateral thermal isolation structure. Corresponding SEM images of cross-sections are shown in Figure 3.6 d–e. plasma enhanced chemical vapor deposition (PECVD) SiO_2 was used as a mask layer (Figure 3.6 a) to create high aspect ratio trenches using DRIE (Figure 3.6 b). Width and depth ratio of trenches was determined by material expansion volume during oxidation [28]. Figure 3.6 d presents the cross-section structure of high aspect ratio trenches. Wet oxidation step was proceeded to obtain a thick silicon oxide block, as in Figure 3.6 c. To ensure a complete and smooth structure of silicon oxide block, sealing and planarization were included, using LPCVD and surface etching. Figure 3.6 e shows the cross-section of the lateral thermal isolation structure after the TEOS sealing and planarization.

3.3.4. DEVICE ASSESSMENTS

TEMPERATURE RESPONSE

To determine if fabricated MHP can achieve fast temperature switch between activated and frozen states, the response time needs to be characterized. Therefore, transient change and stability under constant input heating power of MHP were measured in Figure 3.8. By giving a short current pulse, transient change of the MHP resistance, as a function of time, can be measured as an indication of the average temperature in the heating area. A source-measure-unit (SMU) (Agilent 4156C parameter analyzer) and an oscilloscope were connected to the MHP. The SMU was used to supply an accurate current pulse. The oscilloscope was used to measure the transient change of MHP resistance in both the heating and the cooling process. In the transient resistance measurement, to reach 90 % of total resistance change, it takes approximately 35 ms and 25 ms to stabilize for heating and cooling respectively. Thus, the minimum heat pulse width of MHP is 60 ms. Comparing to the simulation results (Figure 3.3 c), the measured temperature response is shorter. It might be contributed to over-etch of the cavity on the backside,

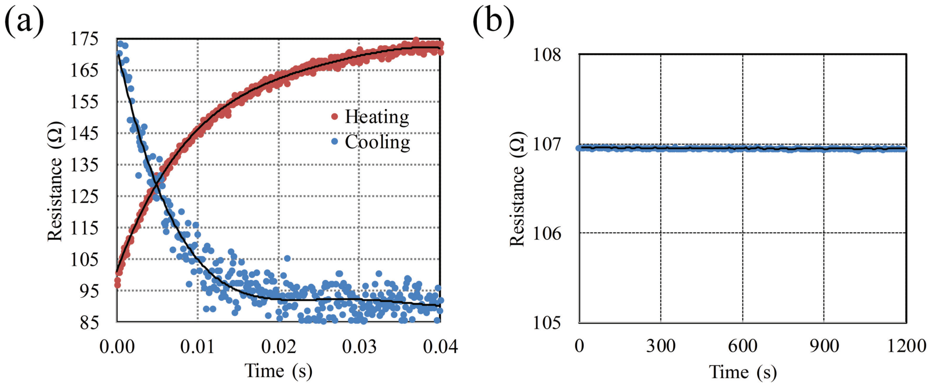

Figure 3.8: (a) Transient measurement of MHP device electrical resistance variation during heating and cooling. (b) 20 min static measurement of MHP device electrical resistance, with input current of 50 mA.

which leads to low heat capacity of the MHP. Thus, the time constant can decrease. Furthermore, the material of lateral thermal isolation structure in the fabricated device is a mixture of thermal SiO_2 and $TEOS$ from LPCVD, which can also introduce variation in temperature response. During fabrication, variations can be introduced to each device in the wafer. Therefore, the time constant of each device should be a bit different. However, the variation from fabrication is limited, since wafer-level process is applied, which limits the process variations to low level. In the application of nanoparticle sintering study, which in the range of seconds to minutes, this variations in temperature response can be neglected.

TEMPERATURE CALIBRATION AND POWER CONSUMPTION

To control the temperature of MHP precisely, the relationship between temperature, power consumption, and MHP electrical resistance needs to be determined. Thus, a series of calibration measurement were conducted. As mentioned above, fabrication variation could influence the device performance. Since an accurate quantitative relation is needed here, wafer-level calibrations and measurements were conducted to determine each device's performance.

Temperature coefficient of resistance (TCR) is a property of all materials, which means that resistance values for conductors at any temperatures other than the standard temperature, varies according to its TCR. For conductive materials, the TCR is usually a positive and constant value of TCR. The specific resistance of conductive material at certain temperatures can be determined by a formula:

$$R = R_{ref}(1+\alpha(T-T_{ref})) \tag{3.10}$$

$$\alpha dT = \frac{dR}{R} \tag{3.11}$$

Where, R is the conductor resistance at temperature T, R_{ref} is the conductor resistance at reference temperature T_{ref}, usually 20 $^\circ C$ or 0 $^\circ C$, and α is the TCR of con-

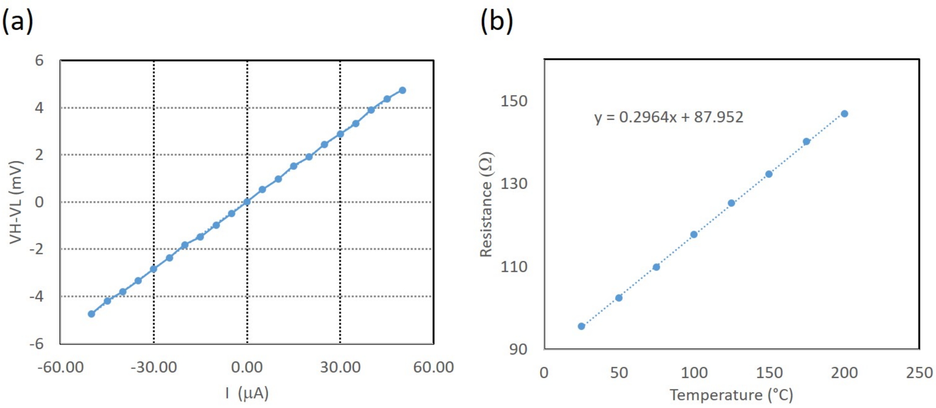

Figure 3.9: (a) Measured MHP resistance of one device at 25 $^{\circ}C$. (b) Resistance of the measured MHP at 8 various temperatures, and its linear regression equation.

ductive material. To obtain the TCR of each device, the device was heated to 8 temperatures, from 25 to 200 $^{\circ}C$, to measure the resistances of MHP at each temperature. With 8 measured resistance, a linear regression between R and T can be conducted, and TCR of the heating metal can be obtained. To perform this experiment, devices on a wafer scale were placed inside a probe station (Cascade) to enable automatic measurement throughout the wafer. A source-measure-unit (SMU) (Agilent 4156C parameter analyzer) was connected as a power source and measurement. The probe station has a heating chuck which can control the measuring temperature.

In the MHP device, the four-point measurement was used. Figure 3.9 a present one of the I-V curve measured from one MHP at 25 $^{\circ}C$. It is linear from -50 - 50 μA, which indicates its conductor property. Combined with other measurements at higher temperatures, a linear increase of resistance can be observed in Figure 3.9 b. The linear regression equation is presented in the figure, where

$$R_{ref} = 87.95j \quad \Omega, T_{ref} = 0 \quad ^{\circ}C \tag{3.12}$$

$$R = R_{ref}(1 + \alpha T \tag{3.13}$$

$$\alpha = \frac{dR}{dT \times R_{ref}} = 0.00337 \quad ^{\circ}C^{-1} = 3.37 \quad ppm/^{\circ}C \tag{3.14}$$

The calculated TCR of Pt layer is very close to reported value from literature. With obtained TCR, and R_{ref} of each device, an accurate correlation between MHP temperature and resistance was established.

Furthermore, power consumption of each device and its corresponding MHP temperature needs to be determined quantitatively. Therefore, the power-current curves of all fabricated devices was investigated at room temperature. In this experiment, the measured wafer was placed by vacuum on the probe station. Air convection on the small surface area is negligible. Thick silicon oxide thermal isolation structure was assumed to

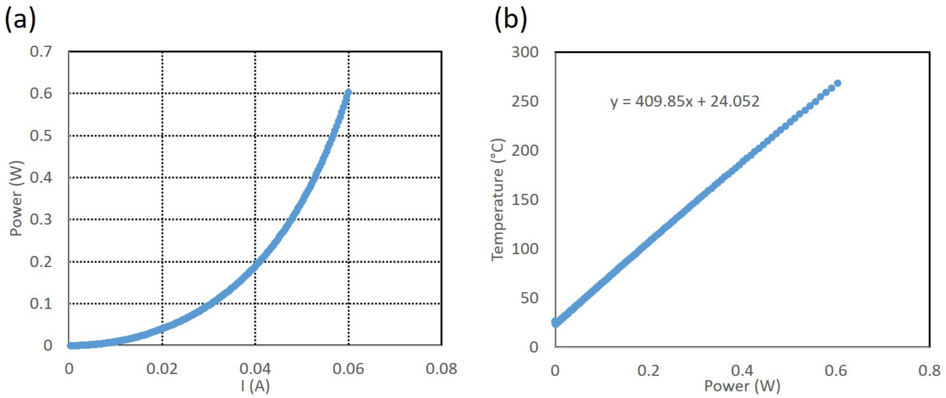

Figure 3.10: (a) Measured power-current curve of one of the MHP. (b) Calculated power-temperature relationship of fabricated MHP.

block considerable heat dissipation in the lateral direction. Only the thermal transfer made by the Joule heating effect on the Si membrane is taken into main consideration. As discussed in section 3.2, the power consumption of the device has a linear relationship with temperature change on the surface, as depicted in Figure 3.10 b. Based on these measured results, the temperature of MHP can be accurately controlled by tuning the input electrical power.

3.4. MHP WITH A SUSPENDED THICK SILICON MEMBRANE

3.4.1. STRUCTURAL DESIGN

As mentioned in the previous section, the device with thick oxidation structure may have risk of damage and vertical displacement at temperature above 300 $^\circ C$, due to CTE mismatch between Si and SiOx. In order to improve the device operation temperature range and optimize the measurement accuracy, a new design with 50 μm-thick suspended Si membrane was proposed. Figure 3.11 shows the schematic of the design. This design consists of similar heating element layout and four-point electrodes as in the previous design. A cavity on the backside of device is also included, to reduce the power consumption. Differently, lateral thermal isolation structure is replaced with air, while thin Si beams provide sufficient mechanical support for the membrane. The thin Si beams are designed with curvature, in order to release thermal expansion of Si, while keep the Si membrane at the same height. With expansion from both Si membrane and beams, the MHP will rotate anti-clockwise, without budging or swelling. Therefore, the XRD detection would not be affected at high temperature. Additionally, instead of using Pt as heating material, Mo is employed in this design, with advantage in process compatibility and high-temperature stability.

3.4.2. FUNCTION VALIDATION WITH SIMULATIONS

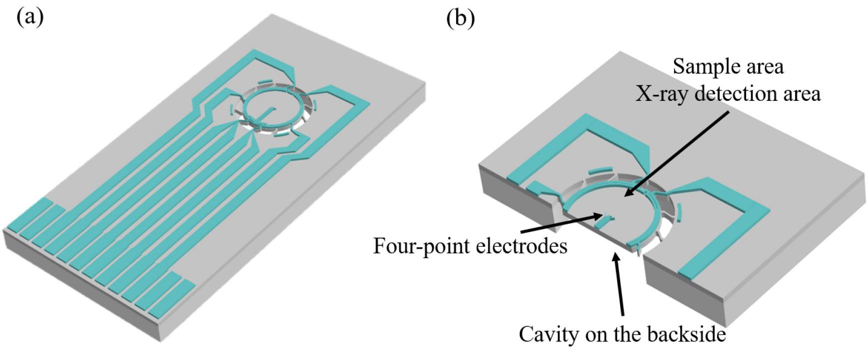

Figure 3.11: The schematic chip design with embedded MHP with suspended thick silicon membrane. (a) An overview. (b) The cross-section view of the device.

THERMAL SIMULATIONS

Finite element simulation was conducted to evaluate the temperature distribution and corresponding mechanical stability at elevated temperatures. A 3D model of MHP, with diameter of 1 mm, was built in COMSOL v5.3a. A variant of heat power was applied on the heating element, from 0.5 - 5 W, with a step of 0.5 W. Similar as in the first design, the natural air convection was included in the simulation, using default data from the software database. The bottom surface of the chip is set as the mechanical constrain. The temperature of the surface is set as 20 $^{\circ}C$, as in the simulation for the first design. To evaluate the profile of simulated results, there is a line drawn in the center of MHP. For nanomaterial characterization that is sensitive to temperature, a temperature variation less than 10 $^{\circ}C$ is considered as an uniform temperature distribution.

Figure 3.12 shows the thermal simulation results. Figure 3.12a, b, d present the results when the input power is 3 W. In the temperature profile of MHP centre line (Figure 3.12b), between -500 μm to 500 μm, there is no temperature variation observed, indicating a homogeneous temperature distribution in that area. There are two peaks of 2.6 $^{\circ}C$ presented, which is 1% higher than the center temperature, due to the heating element on MHP surface. On the edge of the membrane, a drop of 1.6 $^{\circ}C$ can be observed, namely less than 1 % variation from the center temperature. It could be contributed by stronger air convection on the edge. Figure 3.12c presents the surface temperature evaluation of MHP under variant heat power input. Comparing with the design with SiOx thermal isolation, the temperature distribution is comparable, except the minimum temperature. According to the isothermal images, the minimum temperatures happen only at the area connected to Si beams, where the thermal conductivity is locally higher than air. Considering the average and maximum temperature do not have much deviation, the impact of Si beams heat dissipation can be neglected. Therefore, the 1-1.5 mm in diameter X-ray detection area has a temperature uniformity higher than 99.9 %. It is rarely reported in other designs to achieve highly homogenous temperature distribution, in such large area. It meets the requirements for accurate nanomaterial characterization. In Figure 3.12d, time response of the device to temperature was also simulated. The response time is determined as the time device reaches 90 % of total temperature change. In this design, the device is simulated to need 12 ms to response, which is much faster than the previous design (Figure 3.8 b).

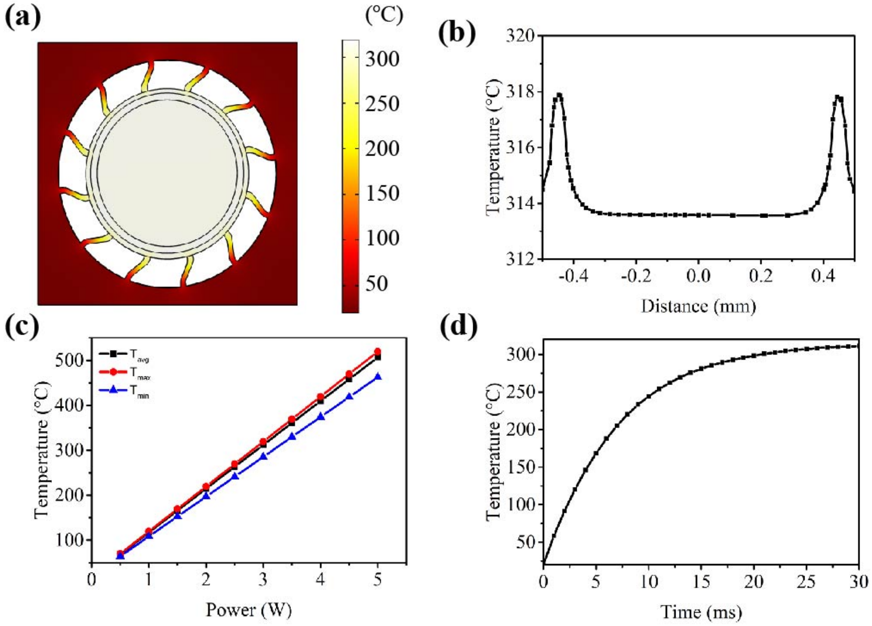

Figure 3.12: Simulated results of the device when the input heat power is 3 W. (Simulated temperature profile along the center of MHP. (c) Simulated average, maximum and minimum temperatures with variant of input heat power. (d) Device temperature response with 3 W heat power.

MECHANICAL SIMULATIONS

Thermal stress of device was also investigated, under the same condition. In Figure 3.13a, the stress level on most of the device area is close to zero. Comparing to the previous design, this structure can release much more thermal stress with assitance of curved Si beams, which improves the mechanical stability dramatically in larger operation temperature range. As shown in the insert of Figure 3.13a, stress concentration up to 300 MPa is observed, at the sharp corner of curved Si beams. Considering the fracture strength of single crystalline Si [30], this structure can withstand high temperature operation. Furthermore, fabricated devices could not have sharp corners as simulated here. Thus, the stress concentration can be avoided. Displacement of device is also evaluated, with direction indicated in Figure 3.13b insert, and profile on the center line in Figure 3.13c. As the red arrow depicted, the suspended Si membrane tends to rotate anti-clockwise to release thermal expansion from itself and beams. Since the Si membrane has a circular shape, there is no displacement in the center, where x value is zero. Furthermore, no vertical displacement was observed, which gives no interference to XRD measurement. Based on the finite element simulation results, the possible operation temperature can be largely expended, with no effect to XRD, by this design.

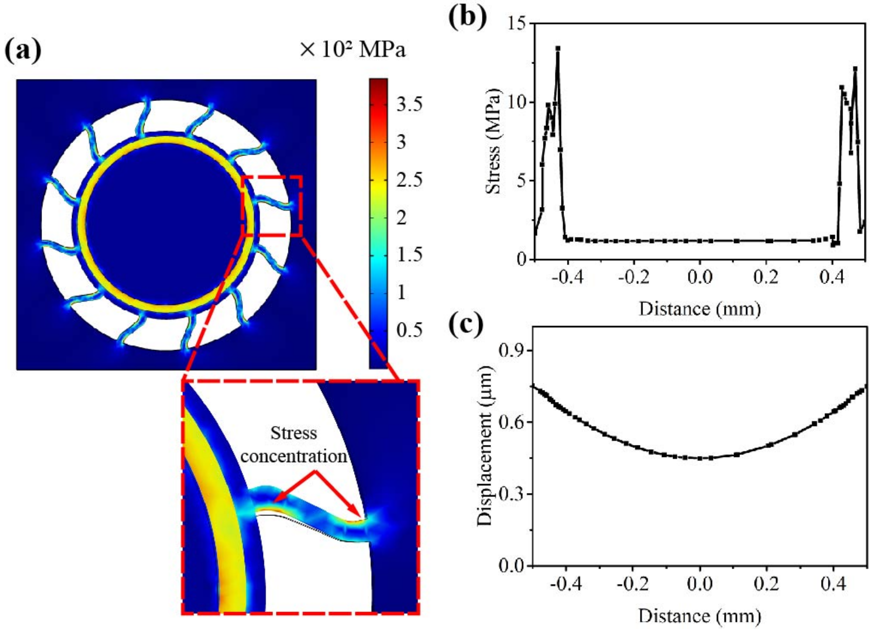

Figure 3.13: The schematic chip design with embedded MHP with suspended thick silicon membrane. (a) An overview. (b) The cross-section view of the device.

3.4.3. MICROFABRICATION

A bulk-micromachining process is developed for the device fabrication in Figure 3.14. A 300 μm thick Si wafer was used as starting material (Figure 3.14a). A 500 nm thick silicon oxide layer was created by thermal oxidation at 1050 $^\circ C$. It was used as an isolation layer between metal and the Si wafer. 50 nm Ti/350 nm Mo/50 nm Ti stacking metal layers(Figure 3.14b) was deposited sequentially by magnetron sputtering. Metal layer were patterned with plasma etching, with photoresist as mask layer. As in Figure 3.14c a 100 nm thick layer of TEOS was deposited on the front side by plasma enhanced chemical vapor deposition (PECVD). The TEOS layer was annealed and covered with a 100 nm SiNx layer by LPCVD. The annealing can solidify TEOS layer. The SiNx layer can provide good barrier to moisture and oxidation. The backside of wafer was also deposited with 3 um TEOS by PECVD. This layer was used as hard mask layer for deep reactive ion etching (DIRE) later. Then the thermal oxide, TEOS and SiNx and SiO_2 on the front side and backside were patterned by plasma etching, with photoresist as mask layer (Figure 3.14d). Both front side and back side plasma etching landed on Si wafer. DIRE was followed on both side, as in Figure 3.14e. On the front side, 50 μm thick Si beams and the MHP area were created by DIRE. Cavities on the back side were created by DIRE on the back side. It landed on predefined Si beams and MHP area. A 50 μm thick suspended Si membrane was created. In Figure 3.14f, contact pads and four-point electrodes were opened by plasma etching, with photoresist as mask layer. It landed on Ti metal layer. A 200 nm Pt metal layer, which is the contact metal layer between device and nanomaterials, was evaporated and patterned by lift-off method. Figure 3.15 shows cross section of fabricated devices under SEM.

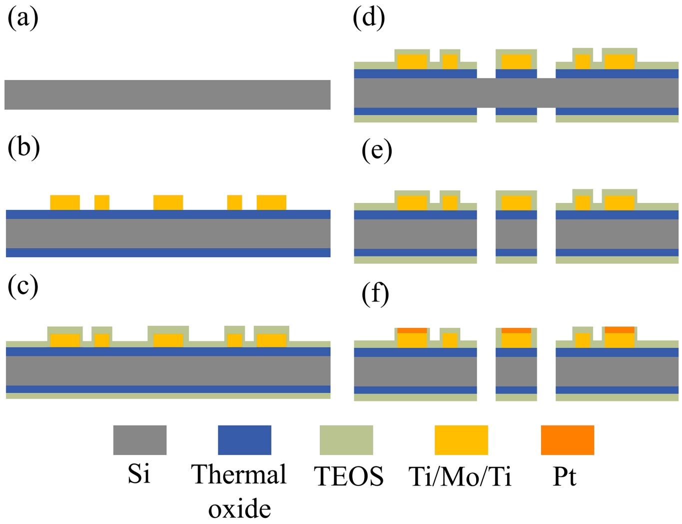

Figure 3.14: Main steps of fabrication of device with thick suspended Si membrane. (a) Start with 300 μm Si wafer. (b) Ti/Mo/Ti metallization on SiNx barrier layer. (c) TEOS protection and isolation layer deposition (d) Hard mask patterning for DIRE on front and backside. (e) DIRE 50 μm from the front side, and 250 μm on the backside. (f) Contact pads and four-point electrodes opening and Pt metallization

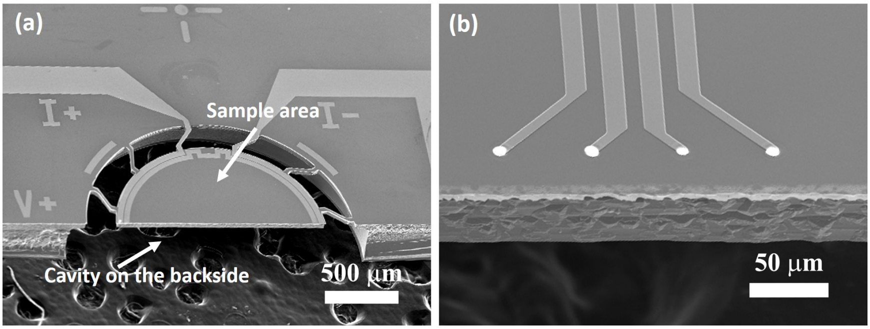

Figure 3.15: SEM images of cross section of fabricated device. (a) Top half of the MHP area, with sample area and cavity labeled. (b) Four-point electrodes for sample electrical resistance measurement.

3.4.4. DEVICE ASSESSMENT

To evaluate the fabricated devices, there are three parts needs to be tested. First is the device response time, which determine if fabricated device can achieve fast switch of temperature. Second, temperature coefficient of resistance (TCR) of the heating element, which is TiN/Ti/Mo/Ti/TiN stacking layer, needs to be measured. It can calibrate accurately the temperature of MHP by its resistance measurement. Third, power consumption curves of each devices are required to correlate power to device temperature.

TEMPERATURE RESPONSE

To measure device stabilization time, a fabricated MHP was connected to a source-measure-unit (SMU) (Keithely 2612B, Tektronix, USA) and an oscilloscope, through microprobes. The SMU was used to supply current pulse. The oscilloscope was used to measure transient change of MHP resistance in both heating and cooling process. By giving a short current pulse, transient change of the MHP resistance, as a function of time, can be measured as an indication of the average temperature in the heating area. In the transient resistance measurement (Figure 3.16), to reach 90 % of total resistance change, it takes approximately 24.50 ms and 25.25 ms to stabilize for heating and cooling respectively. Thus, the minimum heat pulse width of MHP is 49.8 ms. The measured response time is longer than the simulated results (Figure 3.12d). During the fabrication process, especially in the DRIE step on both sides of device, the thickness of the fabricated device can be thicker, and the Si beam size may also be deviated from design. Thus, the response time of each devices can be a bit deviated from measured data in Figure 3.16, due to fabrication variation.

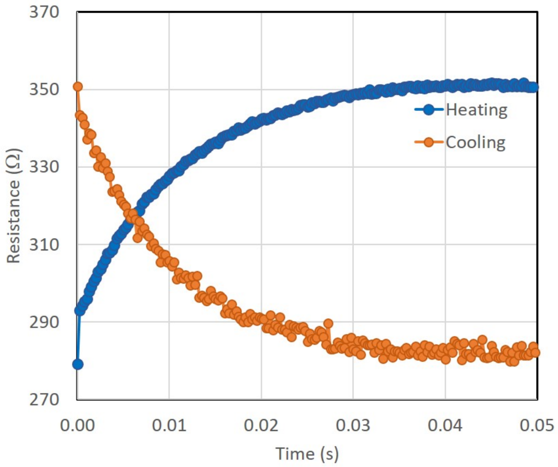

Figure 3.16: Transient measurement of MHP device resistance variation during heating and cooling.

Compared to the first design, using silicon oxide as thermal isolation structure, the time response of this design is faster. According to the discussion in section 3.2, the time constant of the device is determined by following equation, where

$$\tau_0 = C_0 R_0 \tag{3.15}$$

The temperature response of this device is determined together by isolation structure and MHP. The 50 μm-thick Si membrane remains the same in both designs. The diameter and the thickness of the Si membrane remain the same, so the temperature response difference is contributed by the time constant of thermal isolation structures. In the first design, only silicon oxide is used, which has an approximate specific heat of 1.01 $J/g\cdot K$ and thermal resistance of 0.70 $K\cdot m/W$, from reported literature [29, 30]. In the second design, air and Si beams are both employed in thermal isolation structures. Sine air takes most of the volume, it will be considered as the main material for simplification. Air has a similar specific heat of 1.00 $J/g\cdot K$ and much higher thermal resistance of 38.5 $K\cdot m/W$ at 300 K [31, 32]. Therefore, the second design has a thermal isolation structure with much larger time constant. This means that it takes much longer time for air and Si beams to reach steady state, which decrease the response time of Si membrane to achieve targeted temperature, namely temperature response. Similar as discussed in section 3.2.4, fabrication variations could contribute to device performance differences. In temperature response, this variation will be neglected, due to limited effect.

TEMPERATURE CALIBRATION AND POWER CONSUMPTION

Same as in 3.2.3.2, to obtain the accurate and precise control of the temperature of the MHP. TCR of the heating element in MHP and power consumption of each fabricated devices were calibrated and measured in wafer level. They were heated to 8 temperatures, from 25 to 200 $^\circ C$. The resistances of each MHP was measure at that temperature. With 8 measured resistance, a linear regression between R and T can be conducted, and TCR of the heating metal can be obtained. To perform this experiment, devices on wafer scale was placed inside a probe station (Cascade) to enable automatic measurement throughout the wafer. A source-measure-unit (SMU) (Agilent 4156C parameter analyzer) was connected as power source and measurement. The probe station has a heating chuck which can control the measuring temperature.

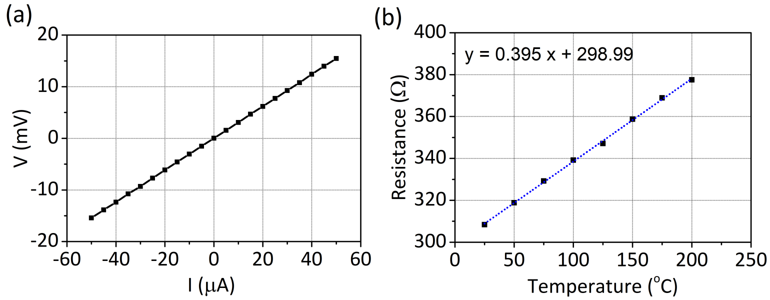

Figure 3.17: .(a) Measured MHP resistance of one device at 25 $^\circ C$. (b) Resistance of the measured MHP at 8 various temperatures, and its linear regression equation

Furthermore, power consumption of each device and its corresponding MHP temperature needs to be determined quantitatively. Therefore, power-current curve of all fabricated devices were investigated at room temperature. In this experiment, measured wafer was placed by vacuum on the probe station. Air convection on the small surface area is negligible. Air between Si beams as thermal isolation structure was assumed to block considerable heat dissipation in the lateral direction. Only thermal transfer made by Joule heating effect on the Si membrane is taken into main consideration, as equation shown in section 3.2.3.2.

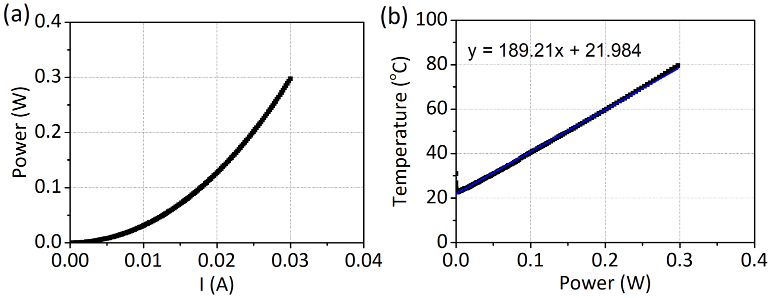

Figure 3.18: (a) Measured power-current curve of one of the MHP. (b) Calculated power-temperature relationship of fabricated MHP.

Temperature of MHP has a linear relationship with both power consumption and resistance of heating element at that temperature. Figure 3.18b showed measured results, which device showed linear relationship between power consumption and temperature. Thus, temperature of MHP can be accurately controlled by applying different power.

3.5. PACKAGING AND CHIP MOUNTING

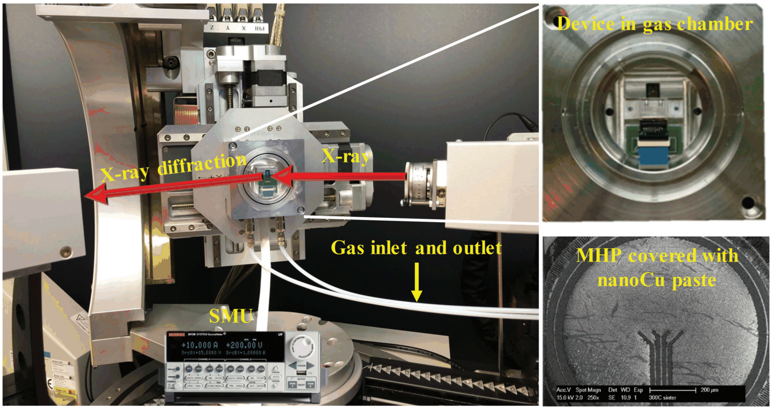

Figure 3.19: TRXRD experiment set-up. Chip is connected to source-measurement unit (SMU) for temperature control and real-time measurement. The SEM image on the right corner shows a MHP device covered with Cu NP-based paste.

To enable environmental TRXRD, a gas cell is introduced in the setup. In the gas cell, MEMS chip is placed in the middle, with electrical connection for MHP and four-point measurement. A dual-channel SMU (Keithley 2612B, Tektronix, USA) is connected to control the temperature of MHP and monitor the electrical resistance of the sample precisely. On top of the gas cell, a polypropeiene film (thickness < 13 μm), which is X-ray transparent, is applied to seal reaction gas inside, without the effect of the XRD measurement. As shown in Figure 3.19 inset, The gas cell was mounted on XRD equipment (D8

Explorer, Bruker, USA) for TRXRD, with X-ray source of Cu $K\alpha$ radiation, $\lambda = 1.54$ Å.

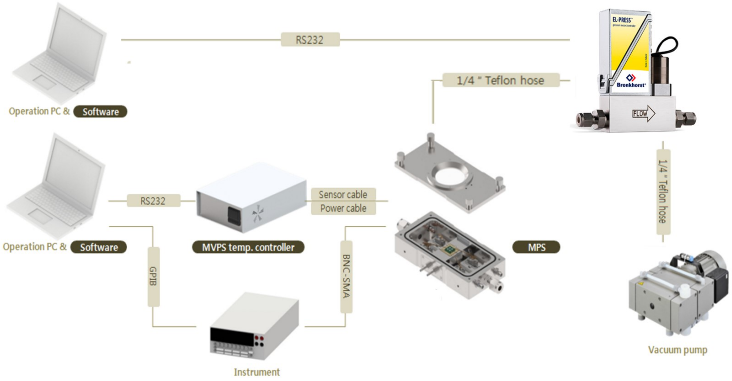

Figure 3.20: Vacuum probe station setup for thermal sintering.

For the thermal sintering in a vacuum condition, the entire system is shown in Figure 3.20. Unlike previous thermal sintering in forming gas, the target temperature in vacuum was achieved by a hotplate integrated with the micro-probe-station (NEXTRON, Korean). The temperature controller (NEXTRON, KR) connected with MPS allows chuck temperature up to 750 $^{\circ}C$. Other core components in the system comprised a vacuum pump and a pressure controller (P1-CONTROL, Bronkhorst, NL), which enabled vacuum conditions.

3.6. CONCLUSION

IN this chapter, a MEMS-based TRXRD nanomaterial characterization platform is designed and fabricated. It contains an embedded MHP for temperature control and four-point electrical measurement electrodes for sample property monitoring. A gas cell was employed to provide an environmental experimental condition, without interference with XRD measurements. To achieve the optimum temperature fast switch and mechanical stability, lateral thermal isolation structures were proposed and fabricated. With these designs, a 60 ms minimum heat pulse width and uniform temperature distribution were achieved. Combined with gas cell and power supply, it can enable TRXRD characterization of nanomaterial, with large flexibility of temperature control and gas environment.

REFERENCES

[1] B. Zhang, J. Wei, A. J. Böttger, H. W. van Zeijl, P. M. Sarro, and G. Zhang. Mems enabled fast time-resolved x-ray diffraction characterization platform for copper nanoparticle sintering in heterogeneous integration applications. In *2019 20th International Conference on Solid-State Sensors, Actuators and Microsystems & Eurosensors XXXIII (TRANSDUCERS & EUROSENSORS XXXIII)*, pages 1772–1775.

[2] Daniel Lu and C. P. Wong. *Materials for advanced packaging*, volume 181. Springer, New York, 2009.

[3] Wolfgang Arden, Michel Brillouët, Patrick Cogez, Mart Graef, Bert Huizing, and Reinhard Mahnkopf. More-than-moore white paper. *ITRS White Paper*, 14, 2010.

[4] William Chen, WR Bottoms, Klaus Pressel, and Juergen Wolf. The next step in assembly and packaging: system level integration in the package (sip). *ITRS White Paper*, 9, 2008.

[5] Peng Peng, Anming Hu, Adrian P. Gerlich, Guisheng Zou, Lei Liu, and Y. Norman Zhou. Joining of silver nanomaterials at low temperatures: processes, properties, and applications. *ACS Applied Materials & Interfaces*, 7(23):12597–12618, 2015.

[6] Wei Liu, Rong An, Chunqing Wang, Zhen Zheng, Yanhong Tian, Ronglin Xu, and Zhongtao Wang. Recent progress in rapid sintering of nanosilver for electronics applications. *Micromachines*, 9(7):346, 2018.

[7] Seyed Amir Paknejad and Samjid H. Mannan. Review of silver nanoparticle based die attach materials for high power/temperature applications. *Microelectronics Reliability*, 70:1–11, 2017.

[8] Xiaomin Wang, Yunhui Mei, Xin Li, Meiyu Wang, Zhenduo Cui, and Guoquan Lu. Pressureless sintering of nanosilver paste as die attachment on substrates with enig finish for semiconductor applications. *Journal of Alloys and Compounds*, 777:578–585, 2019.

[9] Jesus N Calata, Guo-Quan Lu, Khai Ngo, and Luu Nguyen. Electromigration in sintered nanoscale silver films at elevated temperature. *Journal of electronic materials*, 43(1):109–116, 2014.

[10] Raphaël Riva, Cyril Buttay, Bruno Allard, and Pascal Bevilacqua. Migration issues in sintered-silver die attaches operating at high temperature. *Microelectronics Reliability*, 53(9-11):1592–1596, 2013.

[11] Yoichi Kamikoriyama, Hiroshi Imamura, Atsushi Muramatsu, and Kiyoshi Kanie. Ambient aqueous-phase synthesis of copper nanoparticles and nanopastes with low-temperature sintering and ultra-high bonding abilities. *Scientific Reports*, 9:1–10, 2019.

[12] Z. Zhang, C. Chen, Y. Yang, H. Zhang, D. Kim, T. Sugahara, S. Nagao, and K. Suganuma. Low-temperature and pressureless sinter joining of cu with micron/submicron ag particle paste in air. *Journal of Alloys and Compounds*, 780:435–442, 2019.

[13] Mai Kanzaki, Yuki Kawaguchi, and Hideya Kawasaki. Fabrication of conductive copper films on flexible polymer substrates by low-temperature sintering of composite cu ink in air. *ACS Applied Materials & Interfaces*, 9(24):20852–20858, 2017.

[14] Jingdong Liu, Hongtao Chen, Hongjun Ji, and Mingyu Li. Highly conductive cu–cu joint formation by low-temperature sintering of formic acid-treated cu nanoparticles. *ACS Applied Materials & Interfaces*, 8(48):33289–33298, 2016.

[15] Di Erick Xu, Jang Baeg Kim, Michael David Hook, Jae Pil Jung, and Michael Mayer. Real time resistance monitoring during sintering of silver paste. *Journal of Alloys and Compounds*, 731:504–514, 2018.

[16] X. Milhet, A. Nait-Ali, D. Tandiang, Y. J. Liu, D. Van Campen, V. Caccuri, and M. Legros. Evolution of the nanoporous microstructure of sintered ag at high temperature using in-situ x-ray nanotomography. *Acta Materialia*, 156:310–317, 2018.

[17] A. Ziegler, H. Graafsma, X. F. Zhang, and J. W. M. Frenken. *In-situ Materials Characterization: Across Spatial and Temporal Scales*. Materials Science. Springer-Verlag Berlin Heidelberg, 2014.

[18] M. Hummelgard, R. Zhang, H. E. Nilsson, and H. Olin. Electrical sintering of silver nanoparticle ink studied by in-situ tem probing. *PLoS One*, 6(2):e17209, 2011.

[19] M. Yeadon, J. C. Yang, and R. S. Averback. In-situ observations of classical grain growth mechanisms during sintering of copper nanoparticles on (001) copper. *Appl Phys Lett*, 71, 1997.

[20] J. Tijn Van Omme, Marina Zakhozheva, Ronald G. Spruit, Mariya Sholkina, and H. Hugo Pérez Garza. Advanced microheater for in situ transmission electron microscopy; enabling unexplored analytical studies and extreme spatial stability. *Ultramicroscopy*, 192:14–20, 2018.

[21] David W Hahn and M Necati Özisik. *Heat conduction*. John Wiley & Sons, 2012.

[22] Maria Eloisa Castagna, Roberto Modica, Salvatore Cascino, Maurizio Moschetti, Viviana Cerantonio, Alberto Messina, and Antonello Santangelo. A high stability and uniformity w micro hot plate. *Sensors and Actuators A: Physical*, 279:617–623, 2018.

[23] Qi Liu, Guifu Ding, Yipin Wang, and Jinyuan Yao. Thermal performance of micro hotplates with novel shapes based on single-layer SiO_2 suspended film. *Micromachines*, 9(10):514, 2018.

[24] L. Mele, F. Santagata, E. Iervolino, M. Mihailovic, T. Rossi, A. T. Tran, H. Schellevis, J. F. Creemer, and P. M. Sarro. A molybdenum mems microhotplate for high-temperature operation. *Sensors and Actuators A: Physical*, 188:173–180, 2012.

[25] Robert Hull. *Properties of crystalline silicon*. IET, 1999.

[26] C. Zhang and K. Najafi. Fabrication of thick silicon dioxide layers for thermal isolation. *Journal of Micromechanics and Microengineering*, 14(6):769–774, 2004.

[27] Yoshimasa Takahashi, Hikaru Kondo, Hironobu Niimi, Takeshi Nokuo, and Toshiaki Suzuki. Fracture strength analysis of single-crystalline silicon cantilevers processed by focused ion beam. *Sensors and Actuators A: Physical*, 206:81–87, 2014.

[28] J. Wei, C. Yue, M. van der Velden, Z. L. Chen, Z. W. Liu, K. A. A. Makinwa, and P. M. Sarro. Design, fabrication and characterization of a femto-farad capacitive sensor for pico-liter liquid monitoring. *Sensors and Actuators A: Physical*, 162(2):406–417, 2010.

[29] M. G. Burzo, P. L. Komarov, and P. E. Raad. Thermal transport properties of gold-covered thin-film silicon dioxide. *IEEE Transactions on Components and Packaging Technologies*, 26(1):80–88, 2003.

[30] B. El-Kareh and L. N. Hutter. *Fundamentals of semiconductor processing technology*. Springer US, 2012.

[31] J. Hilsenrath. *Tables of thermal properties of gases: comprising tables of thermodynamic and transport properties of air, argon, carbon dioxide, carbon monoxide, hydrogen, nitrogen, oxygen, and steam*, volume 564. US Department of Commerce, National Bureau of Standards, 1955.

[32] Engineering ToolBox. Air-thermal conductivity, 2009.

4

TIME-DEPENDENT STUDY OF COPPER NANOPARTICLE-BASED PASTE SINTERING MECHANISM

In this chapter, a time-dependent study of the sintering process of copper nanoparticle-based paste is performed using a MEMS-based material characterization platform under XRD. Both static and dynamic study was conducted, together with electrical resistance and microstructure analysis. Combined XRD with these analyses, the sintering process can be divided into three different phases, including organic solvents evaporation, surface oxides reduction, and Cu NP sintering. With the information obtained from other characterization methods, complete knowledge of Cu NP sintering at various scale can be understood.

4.1. INTRODUCTION

It is challenging to optimize the sintering process of Cu NP paste, since it is easy to be oxidized in an ambient atmosphere. To overcome this risk, a few attempts were made, including organic shell and reductive additives [1–3], to protect them from oxidation, without interference with the fusion process between particles. Complex paste system and reactive property of Cu NPs increase the difficulty to obtain an optimum sintering process of Cu paste. Understanding the Cu NP sintering process is one of the fundamental approaches to reveal the mechanisms in detail [4, 5].

For research works reported about Ag paste, there are advanced characterization methods applied to explicit sintering mechanism into nano-level [6–9]. However, there are limited works that included the dynamic response of the impact of process parameters, which knowledge can be transferred to applications. As one of the emerging materials in die-attach for power electronics application, Cu paste catches much attention from researchers. As reviewed in Section 1.3, numbers of works have been done in material synthesis, process optimizations and mechanism explorations by both experimental and simulation methods. Effect of temperature, particle size and sintering conditions were investigated in various aspects. As a dynamic process, the sintering of a complex system as metallic nanoparticle paste involves multiple stages. Combining static and dynamic study to separate and understand these stages have essential value to push Cu paste in power electronics application more efficiently. With the platform developed in Chapter 3, temperature, time and atmosphere impacts can be studied. In this chapter, the atmosphere of forming gas is applied through all the experiments. A commercial copper paste is studied with TRXRD at various temperatures and time frame. Combined with other characterization results, deeper and complete knowledge of copper paste sintering can be obtained, at variant scales.

4.2. EXPERIMENT AND CHARACTERIZATIONS

Process flow is shown in Figure 4.1. One commercial Cu NPs-based paste is used in this experiment. To dispense the Cu paste on the MHP surface, it was diluted with isopropanol (99%, Sigma Aldrich, USA) to reduce its viscosity. Then only a small amount of diluted paste was drop casted on the MHP surface. After paste application, MEMS chip were dried at 150 $^\circ C$ for 30 min in a convection oven (Binder FP30, Germany), to remove most of the solvents in the paste. Then the MEMS chip was placed in the gas cell for non-ambient XRD experiments. Gas cell was mounted on XRD equipment (D8 Explorer, Bruker, USA), with X-ray source of Cu $K\alpha$ radiation, $\lambda = 1.54$ Å, as shown in Chapter 3 (Figure 3.19). Each XRD scan was conducted in $2\theta/\theta$ mode, from $2\theta = 30 - 100$ °, with 0.05 ° step size for 0.5 seconds.

In the experiment, 5% H_2 + 95% N_2 (forming gas) was employed to sinter Cu paste. Gas flow was 32 ml/min, controlled by a mass flow controller. The temperature profile of MHP was determined by input current from SMU (Keithley 2612B, Tektronix, USA). In static-temperature sintering study, a control loop was created in the corresponding software (Text Script Builder), to ensure temperature stability during the experiment. Based on process temperature in die attach applications, 150-260 $^\circ C$ was selected as temperature range, with a step of 15 $^\circ C$. At each temperature, samples were held for 45 min

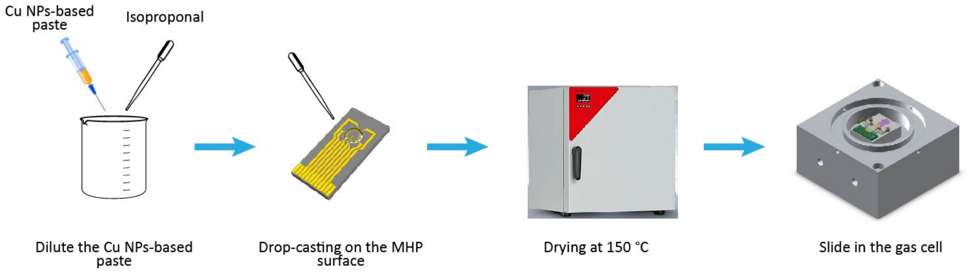

Figure 4.1: Process flow of sample preparation.

to finish all sintering processes, and XRD scans. In the meantime, timestamps of both channels in the SMU were synchronized. Thus the heating process and the electrical measurements can be conducted simultaneously. A 50 μA direct current was input to measure the electrical resistance of the testing sample. After the sintering experiment, samples were fractured to observe the cross-section microstructure. SEM images were taken on both the surface and cross-section of samples (FEI NovaNano, Thermo Fisher, USA).

4.3. STATIC SINTERING BEHAVIOUR STUDY

4.3.1. X-RAY DIFFRACTION STUDY

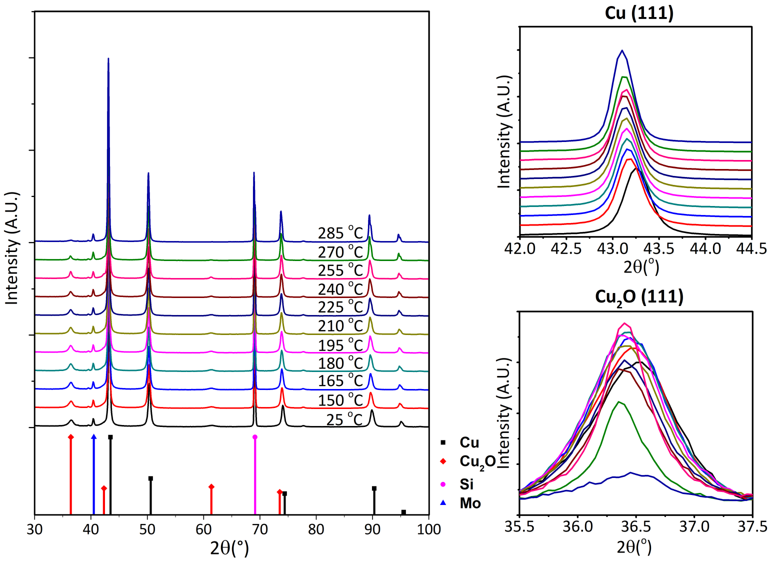

Figure 4.2: XRD patterns of the sample obtained at temperatures from 25 – 285 $^\circ C$, in forming gas, including Cu (111) and Cu_2O (111) peak zoom-in.

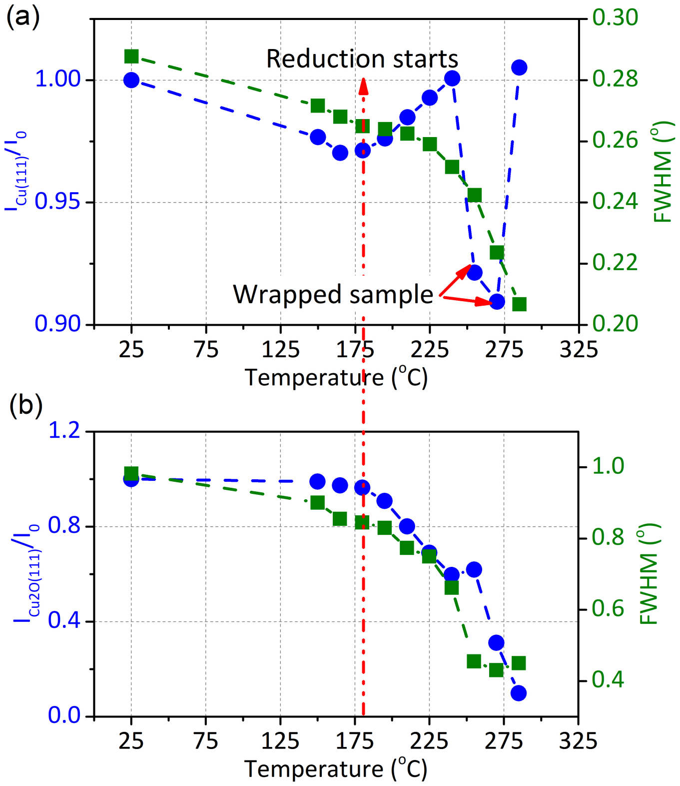

Figure 4.3: Integrated intensity and corresponding full-width-half-maximum (FWHM) of (a) Cu (111), and (b) Cu_2O (111) from 25 – 285 $°C$, in forming gas

At each temperature, an XRD scan was conducted after 45 min holding time. Figure 4.2 shows a series of XRD scans obtained at various temperatures. Figure 4.3 includes the peak intensity evolution of both Cu and Cu_2O peaks. In the XRD pattern, Cu has the strongest peak intensity, indicating that the majority content of the paste is Cu. However, small Cu_2O peaks are also presented, which might be introduced during Cu NP synthesis. As temperature rises up, Cu (111) peak in Figure 4.2 shifted to the left due to lattice expansion. Cu_2O (111) peak is flattened after sintering, due to reduction of H_2.

The peaks intensity evolutions shown in Figure **??** is integrated intensity, which present the peak area above the background. The integrated intensity is proportional to the amount of material in the detected volume. TOPAS was employed to remove background, peak overlapping effect in the diffraction patterns. The larger integrated intensity indicates larger amount of certain materials in the sample. Furthermore, as an indication of the peak shape and grain size, the corresponding peak widths (FWHM) are also extracted. Since the unit of integrated intensity is arbitrary, relative changes of each peaks are introduced. Additionally, the data points at 255 and 270 $°C$ are irregular from the neighboring points, due to a sample wrappage. Since the XRD measurement is sensitive to sample vertical position, it results in two abnormally low points. As sintering temperature rises, the process can be divided into three phases. In the first phase, the integrated intensities and FWHM of both Cu (111) and Cu_2O peak do not have much change between 150 – 180 $^\circ C$. In this stage, most organic solvent did not evaporate, so there is no change of Cu NPs. In the second phase, between 180 - 225 $^\circ C$, Cu_2O intensity started to decrease, while Cu intensity started to increase, indicating that the reduction of Cu_2O is initiated by H_2. At the meantime, both materials' FWHM decreased as the process temperature rises up, due to possible crystalline growth at elevated temperature. After 225 $^\circ C$, Cu_2O peak intensity and Cu FWHM experienced a faster decline until the end of the experiment. This indicates that surface oxidation is reduced dramatically, which leads to a considerable amount of connections and sintering necks formation between Cu NPs. By the end of the experiment at 285 $^\circ C$, there are minor Cu_2O peak intensities detected, which indicates that the reduction of Cu_2O is complete.

Since the Cu NPs inside paste were synthesized by the wet solution method, it usually introduce non-uniform lattice distortions and dislocations in the NPs, which lead to micro strain. Micro strain inside nanomaterials, can contribute to peak broadening, together with crystallite size. There are three most-used methods to separate micro train and crystallite size effect from XRD peak widths, which are Rietveld refinement [10], Warren-Verbach analysis [11] and Williamson-Hall (W-H) method [12]. Considering the complexity and efficiency of each method, the W-H method is employed in this chapter to separate micro strain and crystallite size from the diffraction patterns. The full width half maximum (FWHM) of each peaks relation to micro strain and crystallite size can be written as:

$$\beta^2_{hkl} = [(\beta^2)_{measure} - (\beta^2)_{instrument}] \tag{4.1}$$

$$\beta_{hkl} cos\theta = \frac{k\lambda}{D} + 4\frac{\sigma}{E_{hkl}}\epsilon sin\theta \tag{4.2}$$

Where β_{hkl} is the FWHM of one peak, $\beta_{measure}$ is the peak width from measurement, $\beta_{instrument}$ is the peak width from the X-ray diffractometer, θ is the diffraction angle, λ is the wavelength of X-ray source, D is the crystallite size, σ is ϵ is the micro strain, E_{hkl} is Young's modules on certain orientation of (hkl). In the W-H model, the peak broadening has a linear relation with micro strain. By plotting $\beta_{hkl} cos\theta$ as a function of $4 sin\theta$, crystallite size D and micro strain ϵ can be obtained from intercept and slop in the linear fitting. Based on the W-H analysis method, in Figure 4.4, the evolution of Cu NPs micro strain and crystallite size as sintering temperature rise can be analyzed. As the temperature increase, the strain level in Cu NPs continuously decrease. From 150 – 180 $^\circ C$, while both Cu and Cu_2O peaks did not change much, the micro strain decrease can be contributed mainly by thermal relaxation and rearrangement of the atoms in the lattice, which reduce the defects amounts in the sample. In this temperature range, crystallite size of Cu remains the same. Between 180 - 225 $^\circ C$, the reduction of Cu_2O does not effect Cu much. From 225 $^\circ C$, the crystallite size started increase from 50 nm to around 70 nm, the same as shown in Figure **??** a. Furthermore, the micro strain also followed with a faster decrease, indicating sintering neck formation process during this temperature range. At the end of the experiment, the strain level of Cu reduced close to 0, which presents a mostly defects-free and connected networks in the sintered Cu paste.

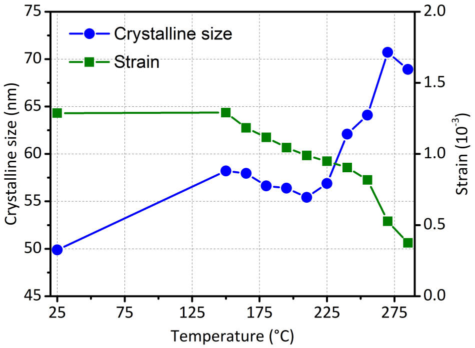

Figure 4.4: Analyzed micro strain and crystallite size of Cu at various temperature, by using the W-H method.

From XRD analysis, Cu NPs in the paste experience three different stages, in forming gas. In the first stage, between 25 – 180 $°C$, there is a relatively slow change in this temperature range. In the second stage, from 180 – 240 $°C$, the reduction of Cu_2O started, from intensity evaluation. However, no Cu crystallite growth is observed. In the Cu paste, besides Cu NPs, there are normally many types of solvents and organic additives added in the system. These contents have different evaporation temperatures. In this temperature range, there might be still some organic residues among Cu NPs, which can prohibit Cu NPs from sintering neck formations. However, a slow reduction can be initiated due to fast diffusion of H2 gas molecules and partially exposed Cu_2O surfaces. After 240 $°C$, fast reduction and crystalline growth began, indicating that there are barely organics left in the sample. Higher temperature drives reduction reaction and Cu NPs inter-particle diffusion faster. Thus, a connected sintered network can be formed.

4.3.2. $In-situ$ ELECTRICAL RESISTANCE

During the entire sintering process, the embedded four-point electrical resistance electrodes in-situ monitored the electrical resistance change of the sample, as shown in Figure 4.5 a. Electrical resistance of the sintered material is an indication of the level of condensation and sintering. The lower electrical resistance, a more condensed sintered structure is obtained. Additionally, it is also one of the most applied measurement method in electronics application. Understanding the relation between electrical resistance and crystallography during sintering can accelerate the Cu NPs-based paste into the applications.

In the Figure 4.5 a, the electrical resistance of Cu paste decrease, as the sintering temperature increases. At the beginning of the experiment, sample resistance dropped two orders, once the temperature rose to 150 $°C$. After drying step, there are probably still some organic compounds remained. Thus, the electrical resistance drops due to the further evaporation of solvents. At this stage, the sample has a very high electrical resistance due to a lack of connections between Cu NPs, according to XRD analysis. Afterward, as the temperature increases gradually, the resistance of the sample also experienced a de-

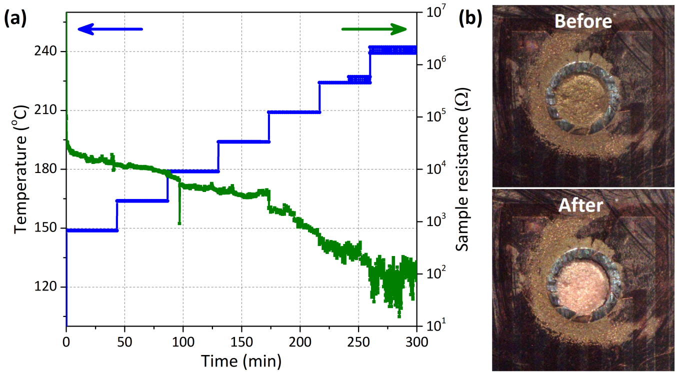

Figure 4.5: $In - situ$ electrical resistance measurement of the sample, in forming gas. (b) Optical images of the sample before and after sintering.

crease correspondingly. However, there is no significant resistance decrease observed in the entire sintering process, even the sample was reduced and crystalline grew well, according to XRD analysis. Furthermore, in the optical pictures taken before and after sintering (Figure 4.5b), the sample color changed from matt, dark brown to shiny, light brown, which can also indicate the completion of the reduction process. In the electrical measurement, a small direct current of 50 μA was applied, which can have an electrical field of a few micrometers. However, the tested sample has a thickness of more than 10 μm. In XRD measurement, X-ray can penetrate most of the sample thickness, which can give a collective investigation of the material in the entire heating area. Along with the thickness, there might be a microstructure variation, especially on the bottom of the sample, where electrodes were placed to measure. That measurement location variation can contribute to differences between measured resistance and XRD analysis.

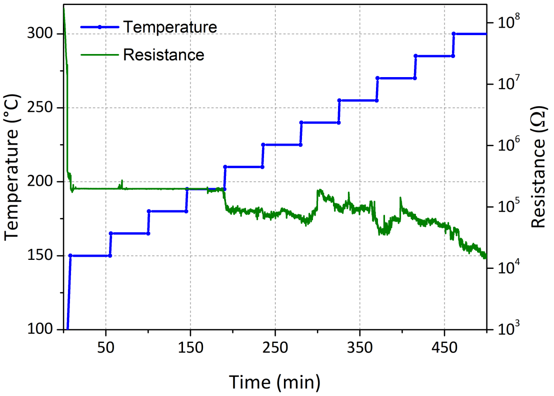

Figure 4.6: In-situ electrical resistance measurement of the sample, from 25 – 300 $^{\circ}C$, in a vacuum. Step size is 15 $^{\circ}C$, with a ramping rate of 15 $^{\circ}C$/min.

Similar to in sintering experiment in forming gas, a Cu paste sample was placed in a vacuum environment, with in-situ electrical resistance measurement, as shown in Figure 4.6. The temperature profile was conducted by the heating stage from the vacuum probe station. The same heating steps were followed, from room temperature to 300 $^{\circ}C$, with 15 $^{\circ}C$ steps. The heating ramping rate is 15 $^{\circ}C$/min. At each temperature, the holding time is 35 min. Since the vacuum probe station cannot be mounted in XRD equipment, there is not XRD analysis included in the experiment. There are three stages can be observed. Firstly, from 25 – 150 $^{\circ}C$, the sample resistance dropped dramatically from non-conductive to 105 Ω. After that, in the second phase, the resistance entered in a plateau, where no obvious change is found. In the third stage, from 195 $^{\circ}C$ until the end of the experiment, the resistance started to decrease again, with fluctuation. In the first stage, resistance decrease could be mainly contributed by the thermal expansion of organic compounds. During the second plateau phase, since the environment is a vacuum, there is rarely a gas atmosphere for organic compounds to react with and decompose. Thus, evaporation is the main method to remove organic additives in the paste. Additionally, with the help of a vacuum, the evaporated solvents can be eliminated from Cu joints easily. However, since the oxidation layer on the surface, the sample resistance remained the same. In the third phase, the resistance drop indicates that most of the organic additives were eliminated, due to the heating process. Cu NPs surface can initiate contacts and form better electrical conduction paths. Therefore, the resistance started to decrease with some fluctuations.

4.3.3. MICROSTRUCTURE ANALYSIS

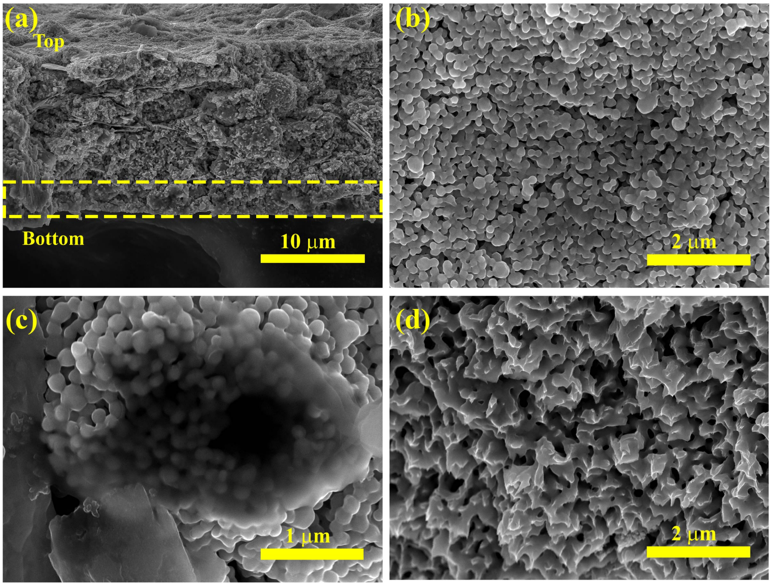

Figure 4.7: SEM images of cross-section and microstructure of sintered Cu paste in forming gas.

Figure 4.7 shows the microstructures of Cu paste sintered in forming gas. The cross

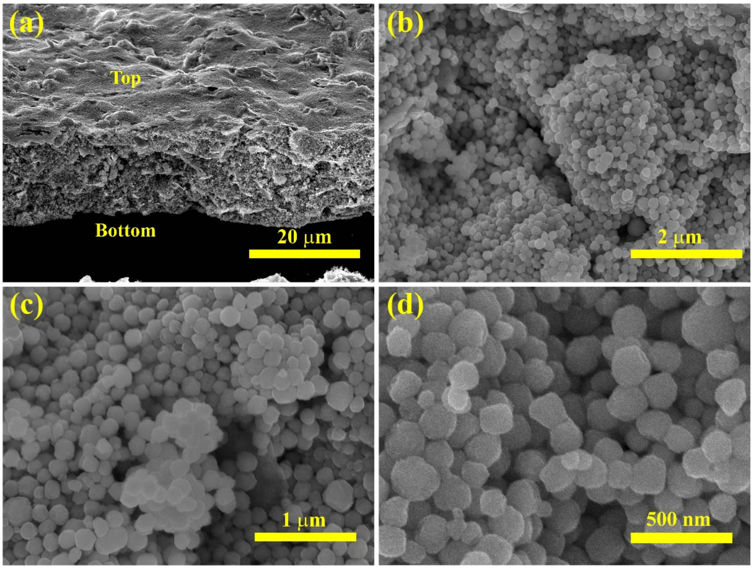

Figure 4.8: SEM images of (a) cross section and (b – d) microstructure of sintered Cu paste sample in vacuum.

section structure is presented in Figure 4.7 a, which has a thickness of approximately 15 μm. There are barely voids observed in the SEM viewfield. In the area labeled (Figure 4.7a) at the bottom of the sample, a darker contrast can be observed. iFigure 4.7 c also presents one of the particle clusters together with darker contrast. From XRD analysis, we can confirm the only crystalline material after sintering is Cu. In SEM images, the morphology of the content with darker contrast does not agree with metallic nanoparticles. Additionally, it is known that epoxy is introduced in the paste, which is often used as a paste hardener in the paste to increase the mechanical strength and reliability. Thus, the different contrast can possible caused by organic residues. Appearance of organic residues (epoxy) on the bottom agrees with the high resistance measured at the end of the sintering process. However, due to lack of back scattering electron images, it can not be confirmed yet. Figure 4.7 b shows the upper surface of the sintered sample. Sintering necks can be observed in most of the particle joints, which indicates a good sintering quality. Figure 4.7 d shows the fracture surfaces of this sample, where ductile deformation dominates, which is a typical metallic bond fracture surface features. From the microstructure of the sintered sample in forming gas, a high-level sintering bond is formed after reduction, with some possible organic hardening agents on the bottom.

Figure 4.8 presents the microstructure of the sample sintered in a vacuum. It has the similar thickness as sample sintered in forming gas (Figure 4.8 a). Not much voids can be observed on both cross-section and sample surface, due to a vacuum environment and long process time. However, as shown in Figure 4.8 (b – d), Cu NPs are still separate from neighboring particles, without sufficient sintering neck formations, indicating a lower level of sintering. In Figure 4.8 c, there are a few Cu NPs that are sintered into a cluster, with compact connections between each other. This may contribute to the lower resistance measure in Figure 4.6. With a higher magnification (Figure 4.8 d), Cu NPs with cubic-like morphology are presented. Some Cu NPs initiated good connections with other particles. However, the total amount and diameter of sintering necks are very small and limited. In vacuum environment, organic solvents can evaporate partially at lower temperature range. When sintering temperature exceeds 200 °*C*, most of organic compounds are removed by decomposition, which requires gas molecular. In vacuum, there are very low amount of gas molecular available for decomposition. The organic compounds left from evaporation can be remained after sintering, which leads to low conductivity of the sample. Thus, the resistance of this sample after sintering is still more than 104 Ω.

Based on the TRXRD analysis results, the sintering process of this Cu paste can be divided into three phases: solvents evaporation (150 - 180 °*C*), surface oxides reduction (180 - 225 °*C*) and Cu NPs sintering (225 - 250 °*C*). In order to remove the solvents and other organic compounds, gas atmosphere, like N_2, can help with organic decomposition, especially at temperature above 200 °*C*.

4.4. TIME-RESOLVED XRD (TRXRD) STUDY WITH HEAT PULSES

Besides the static study discussed before, a dynamic sintering study was conducted with TRXRD method, together with MHP devices. As introduced in Chapter 3, the designed MHP can achieve fast temperature switch in milliseconds, which can enable a heat pulse with a minimum 60 ms width. In order to have sufficient temperature to reduce surface oxidation and form good sintering connections, 300 °*C* is selected as the sintering temperature in this TRXRD experiment. Considering the reaction kinetics in the sintering process, 1 second, 300 °*C*, heat pulse was given to the Cu paste sample. After every two heat pulses (1 × 2 sec), an XRD scan and electrical resistance measurement are conducted, as shown in Figure 4.9a. With a series repeated cycle, a dynamic material evolution information can be extracted from this experiment. In this experiment, 54 heat pulses were given to the Cu paste sample, in forming gas environment. Thus, the sample received accumulated 54 second of sintering in total. 26 XRD patterns and electrical resistance measurements were collected, corresponding to material status after every two heat pulses.

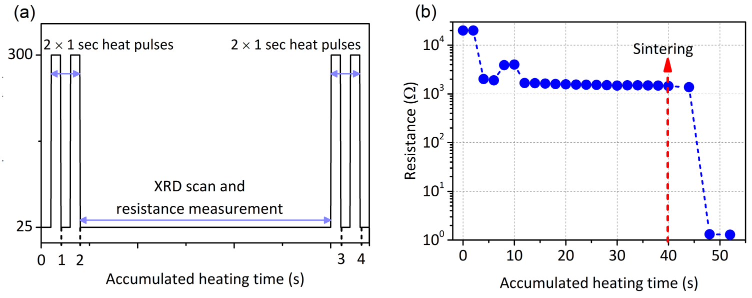

Figure 4.9: (a) Temperature profile used in the TRXRD sintering experiment. The number of heat pulses can be adjusted as required in each sintering process. (b) The electrical resistance change of the sample after every two heat pulses as accumulated sintering time proceeds.

4.4.1. TRXRD ANALYSIS

XRD patterns collected before sintering and after every two heat pulses are shown in Figure 4.10. Each XRD scan take around 30 min, which is difficult to finish all the characterizations in one day, 0 - 30 sec in the first day and 32 - 52 sec in the second day. Therefore, this multi-pulses TRXRD experiment was separated into two days. The sample in the gas cell was left in the XRD instrument overnight, without opening or moving the entire setup. During the night, there was no continuous gas flushing in the chamber. In the pattern showed in Figure 4.10, the strongest peak is from Si, since a Si-based MHP substrate was used. Besides that, peaks from MHP metallization, Mo, is also visible. Besides signals from device, similar as in the static study, Cu is the majority material, since Cu peak remains strong in all patterns presented. Furthermore, with zoom-in insert, Cu_2O can also be detected due to minor oxidation in the paste. Cu_2O (111) peak remained during most of the experiment, until the last four heat pulses.

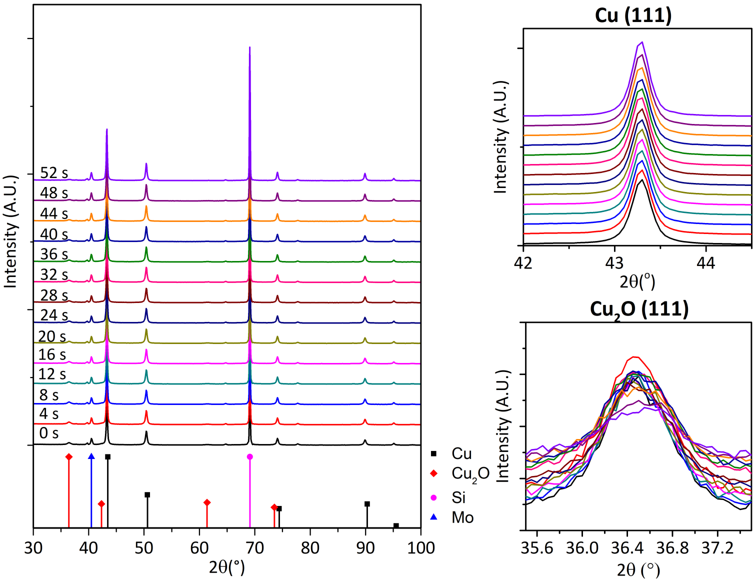

Figure 4.10: XRD patterns obtained from the TRXRD experiment. Inserts include zoom-in patterns of Cu (111) and Cu_2O (111) peaks, from 0 – 52 sec in forming gas.

TOPAS was also used in the analysis of XRD patterns from heat pulses to extract more information about this process. In Figure 4.11, both the integrate intensity and FWHM evolution of Cu (111) and Cu_2O (111) are included, a contradictory trend can be observed. To avoid arbitrary unit, relative change is also used. From 0 – 30 sec (first day), Cu (111) intensity slightly increased, while a slow decrease of Cu_2O (111) intensity is presented after 8 sec of accumulated sintering time. In the contrary, FWHM of Cu (111) slowly decreased, as the value for Cu_2O did not change. From the beginning of the sintering, the evaporation of the organic compounds might not be sufficient. Thus, only small amount of the Cu NPs surfaces are exposed after some solvents removal. Therefore, the reduction of Cu_2O can take place slowly, which also increase the Cu amount correspondingly. After 30 sec, the sample was left in the chamber overnight. On the second day, a second XRD scan was performed before applied the next heat pulse. Thus, two data points are presented at 30 sec. From 30 sec, the integrated intensity values for both Cu (111) and Cu_2O are shifted to higher value. FWHM values for both materials remain the same. As heat pulses went further, the integrated intensity values went back at 40 sec. The possible reason for intensity change after overnight is still unknown. It needs to be investigated further in the future work.After 40 sec, both Cu (111) and Cu_2O (111) experienced much faster change. Cu_2O started to be reduced much faster, followed by intensity increase of Cu (111). This is a clear indication of reduction of surface oxides. Together with reduction, FWHM of Cu (111) decreased, with very limited change of FWHM. This crystalline growth presents that the sintering process initiated at 40 sec and continued until end of the experiment.

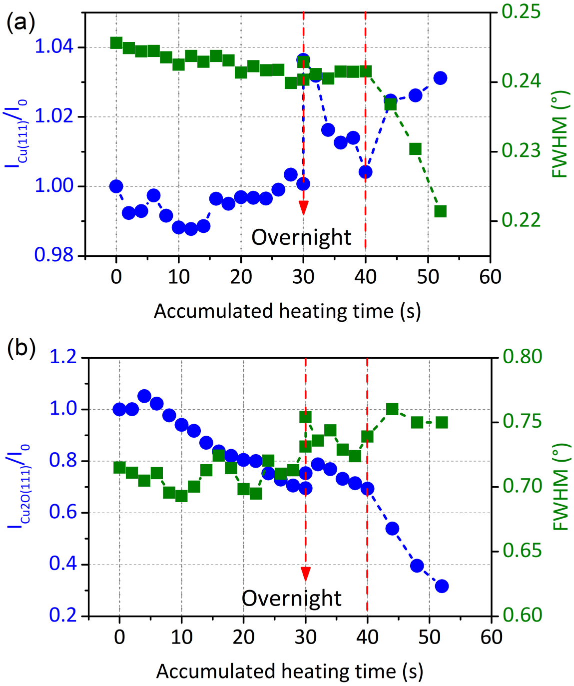

Figure 4.11: Integrated intensity and corresponding FWHM of (a) Cu (111) and (b) Cu_2O (111) from 0 – 52 sec, in forming gas.

With the similar method mentioned before, Cu (111) peak width (FWHM) in XRD patterns obtained in Figure 4.10 was analyzed by W-H method, in Figure 4.12. Thus, the peak broadening contribution from micro strain and crystallite size can be separated. From 0 – 40 sec, there is a minor change in Cu crystallite size, while the micro strain is slowly decrease. Correlate with Figure 4.11, the reduction of Cu_2O is also at slow rate, due to high level of the organic solvents. With surface oxides, Cu NPs can be constrained from crystalline growth. Since the W-H analysis is based on FWHM data, as depicted in Figure 4.11a, it is not effected by overnight left. Between 30 – 40 sec, there the micro strain continuously decreased while the crystallite size of Cu stays the same, indicating that the organic evaporation and surface reduction processes remain the same as 0 - 30 sec. At 40 sec, both micro strain and crystallite size entered the fast change stage, as in Figure 4.11. In the last 12 sec of process time, with mostly exposed Cu NPs surfaces, reduction and crystalline growth can proceed much more vigorous.

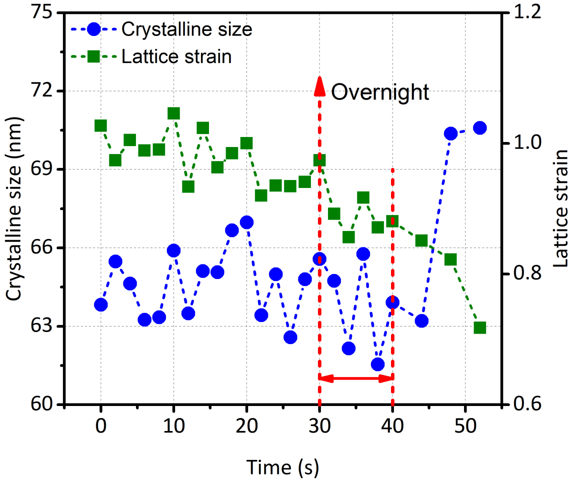

Figure 4.12: Analysed micro strain and crystallite size of Cu at various temperatures, by using the W-H method.

From the TRXRD results analysis, with desecrate segments of materials status, the crystallography change of Cu NPs as a function of time is illustrated with both qualitative and quantitive data. The three stages of sintering in Cu paste, as described in section 4.2.1, also agree with the dynamic study results here. Furthermore, micro strains are often introduced from synthesis process, because of localize defects or intrinsic oxides. To initiate sintering between particles, oxidation layer needs to be removed firstly, so the Cu atoms can be exposed for sintering. In this experiment, micro strain level decrease accordingly with decrease of Cu_2O amount, which indicates that the main source of micro strain. By the end of the experiment, the value for both Cu_2O and micro strain are not close to zero, a study with longer sintering time is needed to investigate their relation further.

4.4.2. $In-situ$ ELECTRICAL RESISTANCE MEASUREMENT

Figure 4.9b shows the resistance change of the sintered sample after every two heat pulses, with accumulated sintering time. In the first two data points, they already reached the maximum measurement value of the current setup. The actual resistance can be much larger than the maximum value, which shows a non-conductive property of the sample. After that, the first drop occurred, with resistance more than 1 $k\Omega$. This first resistance drop is probably a result of solvents evaporation. With less solvent and relative more amount of Cu NPs, the system became more conductive. After that, the resistance sample experiences a gradual decrease until 44 sec, even after overnight left in the gas cell. In this stage, there are two measured data points higher at 8 and 10 sec. These two larger resistances can be contributed by small cracks or delamination between measurement probes, due to shrinkage and thermal shocks. With the further proceeding of the sintering, these cracks or structure damages are probably fixed by inner structure adjustment or condensation. Between 30 – 44 sec, there is no plateau observed as in Figure 4.11 and 4.12. Since XRD measurements were conducted from surface to several micrometers-deep in the sample, it can reflect the collective material property within the whole detection volume. However, the electrical resistance measurement was performed from the bottom of the sample, where less re-oxidation may occur. Thus, the possible surface re-oxidation has limited impact on resistance change. Similar as shown in Figure **??**, when Cu crystalline started to grow at 44 sec, sample resistance also dropped to resistance around 1 Ω. It shows a clear link between Cu connection formation and resistance evolution process.

4.4.3. MICROSTRUCTURE ANALYSIS

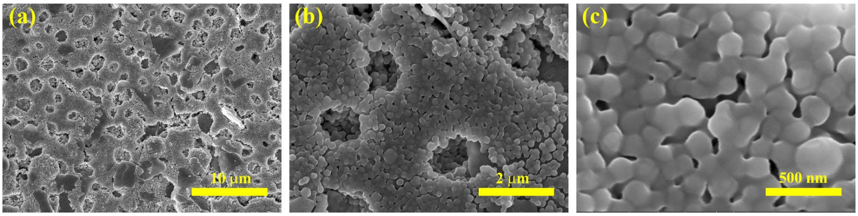

Figure 4.13: SEM images of Cu paste sintered with heat pulses.

After the sintering experiment, the microstructure of the Cu paste sample was observed under SEM, as shown in Figure 4.13. Different from the sample sintered with static temperatures, a porous surface is presented in Figure 4.13 a and b. In this dynamic sintering experiment, a high sintering temperature, and much shorter sintering time were applied. This can lead to limited time for Cu NPs to reorganize for condense structure, after organic solvents evaporation. Thus, large voids can be generated and remained after sintering, from solvent outgassing. In Figure 4.13 b and c, large sintering necks and 3D connections are formed between Cu NPs, in the entire sample surface. This indicates a high-level of sintering with 300 $^\circ C$ heat pulses, and uniform temperature distribution of the MHP.

According to the dynamic study of the sintering process using TRXRD at a constant temperature, we can conclude that Cu NPs paste needs sufficient time and energy for solvents removal and reduction of surface oxides, before it can enter the phase to form sintering necks and connections. For the commercial Cu paste tested here, at 300 $^\circ C$, it needs 40 sec before sintering of Cu NPs start. With this unique method and characterization setup, the continues sintering process can be separated accurately into a series of segments, for a detailed analysis and investigation. The relation between Cu NPs crystallography data and electrical resistance can be correlated, which can lead to simpler, more accurate assessment methods to evaluate sintering level of Cu joints.

4.5. CONCLUSION

IN this chapter, a MEMS-based TRXRD nanomaterial characterization platform was employed to perform both static and dynamic sintering study on Cu NP paste. With embedded MHP and electrodes, the relation between crystallography, electrical resistance and microstructure of Cu paste is evaluated at both steady and dynamic statues. From XRD patterns analysis of both steady and dynamic results, the sintering process can be divided into three stages, solvents evaporation, oxides reduction and Cu NPs sintering. Reduction, sintering temperature and time were also determined from the XRD analysis. At 180 $^\circ C$, Cu_2O starts to be reduced to Cu. 225 $^\circ C$ is the temperature where the formations of sintering neck initiated. In the dynamic sintering study, it is found that sufficient time and energy, which is 40 sec at 300 $^\circ C$, is needed to remove organic solvents and additive, to start sintering. With these two studies, it can validate the concept and function of the designed MEMS-based nanomaterial characterization platform. With these unique method, the sintering process can be investigated with variant perspectives, which results insights and fundamental knowledge valuable for both process development and material optimization of Cu NPs-based paste.

REFERENCES

[1] Yoichi Kamikoriyama, Hiroshi Imamura, Atsushi Muramatsu, and Kiyoshi Kanie. Ambient aqueous-phase synthesis of copper nanoparticles and nanopastes with low-temperature sintering and ultra-high bonding abilities. *Scientific Reports*, 9:1–10, 2019.

[2] Y. T. Kwon, Y. S. Kim, Y. Lee, S. Kwon, M. Lim, Y. Song, Y. H. Choa, and W. H. Yeo. Ultrahigh conductivity and superior interfacial adhesion of a nanostructured, photonic-sintered copper membrane for printed flexible hybrid electronics. *ACS Applied Materials & Interfaces*, 10(50):44071–44079, 2018.

[3] Takuya Morioka, Masafumi Takesue, Hiromichi Hayashi, Masaru Watanabe, and Richard L Smith Jr. Antioxidation properties and surface interactions of polyvinylpyrrolidone-capped zerovalent copper nanoparticles synthesized in supercritical water. *ACS applied materials & interfaces*, 8(3):1627–1634, 2016.

[4] Seunghwa Yang, Wonbae Kim, and Maenghyo Cho. Molecular dynamics study on the coalescence kinetics and mechanical behavior of nanoporous structure formed by thermal sintering of cu nanoparticles. *International Journal of Engineering Science*, 123:1–19, 2018.

[5] Yujin Seong, Youngkyu Kim, Randall German, Sungho Kim, Seong-Gon Kim, See Jo Kim, Hak Jun Kim, and Seong Jin Park. Dominant mechanisms of the sintering of copper nano-powders depending on the crystal misalignment. *Computational Materials Science*, 123:164–175, 2016.

[6] I. L. Regalado, J. J. Williams, S. Joshi, E. M. Dede, Y. H. Liu, and N. Chawla. X-ray microtomography of thermal cycling damage in sintered nano-silver solder joints. *Advanced Engineering Materials*, 21(3), 2019.

[7] Kazuhiko Sugiura, Tomohito Iwashige, Kazuhiro Tsuruta, Chuantong Chen, Shijo Nagao, Tohru Sugahara, and Katsuaki Suganuma. In situ tem observation of sintered ag die-attach layer with added tungsten carbide particles while heating to high temperature. *Japanese Journal of Applied Physics*, 58(10), 2019.

[8] Hao Zhang, Yang Liu, Lingen Wang, Fenglian Sun, Xuejun Fan, and Guoqi Zhang. Indentation hardness, plasticity and initial creep properties of nanosilver sintered joint. *Results in Physics*, 12:712–717, 2019.

[9] Chuantong Chen and Katsuaki Suganuma. Microstructure and mechanical properties of sintered ag particles with flake and spherical shape from nano to micro size. *Materials & Design*, 162:311–321, 2019.

[10] H. M. Rietveld. Line profiles of neutron powder-diffraction peaks for structure refinement. *Acta Crystallographica*, 22(1):151–152, 1967.

[11] B. E. Warren and B. L. Averbach. The effect of cold-work distortion on x-ray patterns. *Journal of Applied Physics*, 21(6):595–599, 1950.

[12] G. K. Williamson and W. H. Hall. X-ray line broadening from filed aluminium and wolfram. *Acta Metallurgica*, 1(1):22–31, 1953.

5

IN-AIR SINTERING BEHAVIOR OF CU NANOPARTICLE-BASED PASTE FOR DIE ATTACHMENT IN HIGH POWER ELECTRONICS APPLICATION

Parts of this chapter have been submitted to Scientific Reports:

Demand is growing for metallic nanoparticle sintering technology to be implemented in die attachment in power electronics. This technology offers superior performance compared to lead-free solders. Although copper nanoparticle-based paste is a potentially low cost material, it faces the challenge of oxidation during the sintering process, which may result in tremendous degradation of mechanical, thermal and electrical properties. Thus, there are very few in-air copper paste sintering reported. In this paper, an in-air pressure-assisted low-temperature sintering process is achieved under low temperature using a commercial copper nanoparticle-based paste. Sintering behavior at various temperatures (200 – 240 °C) and pressures (5 – 25 MPa) was studied. Sintering joints at higher temperatures lead to more condensed microstructures and higher bonding strength. Finally, a maximum shear strength of 41.63 ± 4.35 MPa was obtained after sintering at 240 °C, 25 MPa for 3 min. Different from most reported Cu paste sintering processes in protective atmosphere, all the samples are obtained from in-air sintering. Higher sintering temperature accelerate diffusions between Cu NPs. Sufficient pressure can press out solvents and air. Thus, oxidation of Cu can be constrained, and the sintering process can be initiated. Consequently, a higher level of 3D connections between the copper nanoparticles was achieved. These intact microstructures enable sintered joints to achieve a higher shear strength. Furthermore, a shear strength of 28.1 ± 8.47 MPa was achieved under the sintering condition 10 MPa at 240 °C. This result already meets the requirements for die attachment applications. Thus, the moderate, cost-effective, in-air sintering technology with pressure-assisted can be applied in the high power electronic die attachment applications.

5.1. INTRODUCTION

THE need for miniaturization and integration drives the ongoing power electronics industry [1–3]. Power electronics are often applied in a harsh environment, such as aerospace, energy production and automotive. Wide bandgap semiconductor-based power electronics, including gallium nitride (GaN) and silicon carbide (SiC), have working temperature often exceeds 200 $°C$, sometimes until 350 $°C$. Current silicon (Si) based power electronics and its packaging technology cannot meet these requirements. For die attachment materials, typical lead-free die attachment materials, have a reflow temperature of 220-260 $°C$ [4, 5]. Therefore, novel die attachment or interconnect materials must face both packaging process and application challenges, including lower process temperature but higher operation temperature, higher thermal and electrical properties [6].

Metallic nanoparticles have become one of the most promising candidates for die attach or interconnection in high power electronics [7]. Researchers explored the size effect of metallic nanoparticles [8]. It revealed that metallic NPs could be sintered to bulk material at temperatures below 300 $°C$, which is compatible with current process flow. As a result of that, it may allow for a higher operating temperature than that of SAC solders. Furthermore, intermetallic compounds growth and Kirkendal voids can be possibly avoided, by using one-type sintered materials [9]. Recently, Ag NP paste has been applied widely as die attach material in power electronics applications [10–12]. It allows many benefits as mentioned before. Sintering parameters and material were tuned to improve the mechanical strength of sintered joints [10, 13–15]. Multiple SiC die attachment was successfully applied using Ag NPs sintering [16]. In this study, organic additives removal and bonding layer thickness were believed to have an essential effect on sintering quality. However, the drawbacks of Ag NP paste on electromigration are also of concern in high current flow applications. It was reported that sintered silver joints could have a migration issue at high operation temperature [17, 18]. Since copper has similar thermo-electrical properties to Ag, but higher resistance to electromigration, Cu NP paste becomes one of the emerging die attach materials in high power electronics. The primary experimental sintering behavior of Cu NPs was studied, which indicates that Cu NPs can also be sintered below 300 $°C$ [19]. What's more, sintered Cu NPs, with similar properties to bulk Cu, can withstand a higher operating temperature than SAC alloy.

However, Cu NPs are easily oxidized in air, which would act as a barrier to sintering. To prevent this, a reductive or protective sintering atmosphere is considered necessary for Cu NP paste sintering. Recently, there have been many reports on the Cu NP paste fabrication process to investigate and optimize its performances in die attach. Various atmosphere, including formic acid gas [20], 5% H_2 + 95% N_2 [21, 22], and Ar + H_2 [23] are used in sintering to reduce copper oxides and prevent further oxidation of the Cu NPs, with pressure assistance. High shear strength of 51.7 MPa was achieved using pressure-assisted sintering with reductive treatments [20]. In this work, a formic acid treatment at an external pressure of 10 MPa for 10 min at 260 $°C$ was applied in order to achieve high adhesion strength. It included a dedicated wet chemical treatment and a relatively long sintering process time. As in industrial applications, processing gas and complex wet chemical treatments are time-consuming and costly.

Besides the sintering atmosphere, external pressure during the process is another key parameter. Although pressureless sintering offers the advantage of process simplicity, it sometimes requires strict process conditions and complex pre-treatments. 100% H_2 atmosphere is required to achieve high shear strength [24, 25]. Furthermore, reductive additives and surface modifications were also proven to have positive effect on shear strength without external sintering pressure [26]. Pressureless sintering in 5% H_2 + 95% N_2 or inert gas has also been reported [27, 28]. However, the shear strength of sintered Cu NP joints without pressure ranges mostly below 10 MPa. This might satisfy some applications, which do not require strong shear strength. For die attach in power electronics applications, external pressure is probably needed to enhance the joint strength. Pressure assisted sintering with a mixture of various particle sizes in air condition can increase the shear strength to 20 MPa [29]. Furthermore, the sintering process reported with high shear strength, has mostly process time between 20 min and 1 hour, or even longer, which can decrease the production throughput. Strict sintering atmosphere and complex material treatments can raise the cost and procedures of manufacturing. Consequently, pressure-assisted sintering in an ambient atmosphere to achieve high quality sintered Cu NP joints, without the complexity of process conditions, becomes an essential research topic.

In this chapter, an in-air pressure-assisted sintering process is proposed and achieved using a commercialized Cu NP paste. Sintering behaviors and microstructures of sintered Cu NP joints at various pressures and temperatures are analyzed. The mechanical properties of sintered Cu NP joints were investigated under shear tests. Corresponding fracture mode and microstructure of fracture surfaces are characterized by SEM/FIB. Finally, the possible pressure-assisted sintering mechanism of Cu NP paste in the air was proposed.

5.2. MATETRIALS AND METHODS

5.2.1. CU PASTE CHARACTERIZATION BEFORE SINTERING

A small amount of Cu paste (43.6 mg) was sent for thermogravimetric analysis (TGA) (STA 449, Netzsch, Germany) at room temperature (25 $^\circ C$) up to 500 $^\circ C$ at 10 $^\circ C/min$ ramping rate, in both argon (Ar) and compressed air environments. A mass loss of Cu paste with increasing temperature in selected atmospheres was detected. Cu paste composition and phase change were investigated by an elevated temperature X-ray diffractometer (D5005, Bruker, USA). The X-ray diffractometer (XRD) instrument had a Cu $K\alpha$ (λ = 1.54 Å) X-ray source. A theta/theta scan method was applied. To evaluate the material change at various temperatures, the XRD was equipped with a Pt heating strip to elevate the sample temperature. A thin layer of Cu paste was dispensed on a 10 mm × 10 mm silicon substrate. Cu paste on the silicon substrate was cured first in an N_2 oven at 80 $^\circ C$ for 30 min. Then it was placed on the Pt heating strip of the XRD instrument. The temperature of the sample was monitored by a thermocouple. The sample was heated from room temperature to 300 $^\circ C$, in intervals of 50 $^\circ C$. After the sample was heated and soaked at each stabilized temperature, an XRD scan was conducted.

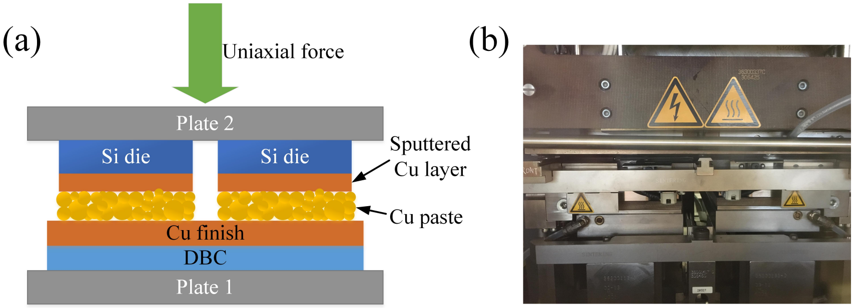

Figure 5.1: (a) Schematic cross-section of the pressure-assisted sintering setup. (b) Pressure-assisted sintering equipment.

5.2.2. CU PASTE SINTERING AND JOINT CHARACTERIZATION

A silicon wafer (0.5 mm in thickness), sputtered with a metal stacking layer (500 nm Al, 200 nm Ni and 300 nm Cu), was used in this experiment (Sigma deposition system, SPTS, UK). After the preparation of the metal layer, it was diced into 2 $mm \times 2$ mm square dies for the pressure-assisted sintering. Direct-bonded copper (DBC) boards with a Cu plating layer were used as substrates in this experiment. The paste was dispensed from a syringe on the DBC in an “X” shaped pattern. Dies were placed on top of the dispensed pattern and paste was squeezed out to fill the area underneath. The bond line thickness measured was 10 μm. The drying step was preceded to remove the low-organic solution and absorbed moisture from the paste. It was performed at 80 $^\circ C$ for 30 min in N_2. Pressure-assisted sintering in the air was conducted with industrial equipment from Besi Netherlands, as in Figure 5.1 b. Figure 5.1 a shows a schematic cross-section of the pressure-assisted sintering setup. The top and bottom press plates (plate 1 and plate 2 in Figure 5.1 a) were firstly preheated at recommended sintering temperature. Then DBC substrates with Si dies attached were then placed in between the two plates. These plates provide axial force and temperature at the same time. Temperature, pressure and holding time were precisely controlled by the equipment. The holding time of sintering process remained the same throughout all the sintering experiments: 3 min. In this sintering process, no protective gas was applied. Various sintering temperatures and pressures were applied to study the sintering behavior of Cu paste. For each sintering condition, one batch of samples was sintered and characterized. Each batch contained 10 – 15 Si dies on DBC substrates.

After sintering, the shear strength of the samples was characterized by a shear die-shear machine (4000 Bondtester, Nordson Dage, UK). The shear strengths of the samples under various sintering conditions were obtained. Furthermore, optical images of the fractured surfaces of sintered Cu joints were investigated (AM3113T, Dino-Lite, Taiwan). Microstructures of the fractured surfaces of the sintered Cu joints were characterized with a scanning electron microscope (NovaNano SEM, FEI, USA). Cross sections of the sintered Cu joints were analyzed with a focused ion beam (FIB) and dispersive X-ray spectroscopy (EDX) (Helios G3-CX, FEI, USA).

5.3. RESULTS AND DISCUSSION

5.3.1. SINTERING TEMPERATURE DETERMINATION

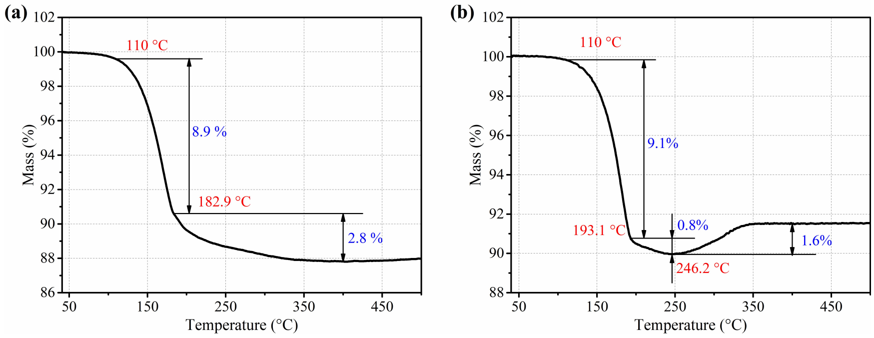

Figure 5.2: TGA results of Cu NP-based paste in (a) Ar and (b) compressed air.

Since Cu paste consists of Cu NPs and multiple types of organic additives, TGA and in-situ XRD were performed and analyzed to determine the appropriate sintering temperature range. Figure 5.2 shows the mass loss and thermal behavior of Cu paste characterized by TGA. In Ar, the mass loss from 50 – 400 $^{\circ}C$ was 12.2 %, including three stages. The first one was 0.5 % between 50 – 110$^{\circ}C$, which might be resulted from moisture and low-evaporation-temperature organic compounds. The second stage was a fast mass loss of 8.9 %, from 110 – 182.9 $^{\circ}C$. Most of the mass loss occurred in this phase, which indicates that most of the solvents evaporate or decompose. Furthermore, there was a third stage, which consisted of a slow mass loss of 2.8 %, from 182.9 – 400 $^{\circ}C$. Due to various kinds of organic additives in the conductive paste, they could have different evaporation and decomposition temperatures.

In compressed air, there were four phases observed in the curve. Similar to the result in Ar, the first phase had a slow mass loss, which was between 50 – 110 $^{\circ}C$. The second phase had a fast mass loss of 9.1 %, from 110 to 193.1 $^{\circ}C$. This was also the largest mass loss of the entire process. It could be contributed by the evaporation and decomposition of multiple organic compounds. Since it has a different atmosphere as in Ar, the temperature range of the second step went further to 193.1 $^{\circ}C$. The third step was a slow mass loss between 193.1 – 246.2 $^{\circ}C$, which was 0.8 %. In the last step, a mass increase of 1.6 % between 246.2 – 400 $^{\circ}C$ was observed. According to the measurement in Ar, the sample had a further mass loss above 246.2 $^{\circ}C$. Above 193.1 $^{\circ}C$, Cu NPs, with low amount of solvents protection, may have a high risk of oxidation. Therefore, the mass change in the last two steps probably includes two parts: one is the mass increase due to the oxidation of Cu, the other one is the mass decrease from the evaporation of organic compounds. In the third phase, the organic evaporation was possibly stronger than oxidation, which resulted in a mass loss. In the last phase, the increase from oxidation is higher than the loss from evaporation, thus a mass increase observed after 246.2 $^{\circ}C$. From measurements above, Cu NP paste can have low organic residuals and moderate oxidation process between 193.1 – 246.2 $^{\circ}C$. Thus, it can be primarily determined as the appropriate sintering temperature in air.

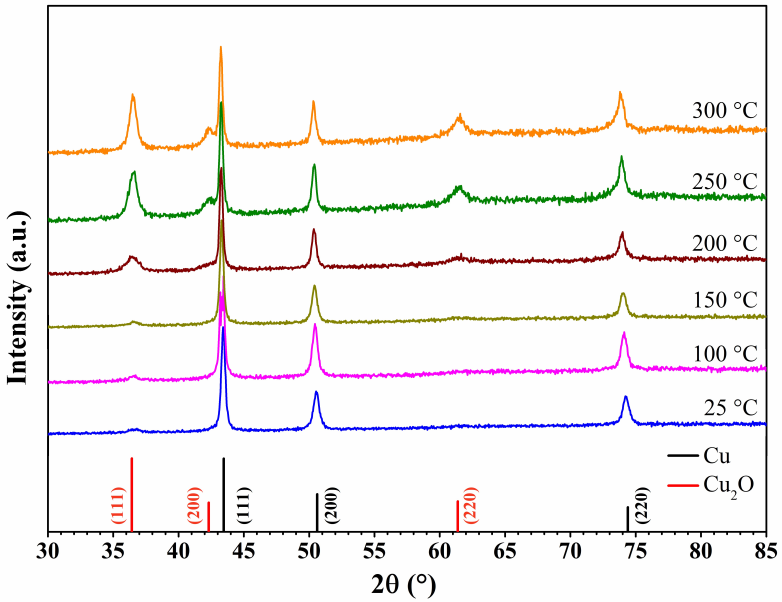

Figure 5.3: X-ray diffraction scans of Cu nanoparticle-based paste at an elevated temperature in air.

To understand the material composition and structural change during the sintering process further, an elevated X-ray diffraction analysis in the air was conducted. Figure 5.3 shows the XRD patterns of Cu NP paste at various elevated temperatures. From room temperature to 150 °C, Cu paste showed three strong Cu peaks, which indicates that Cu NP can resist oxidation until relatively high temperatures. From 200 °C, Cu NP paste started to show a weak Cu_2O (111) peak at $2\theta = 36.9$ °, but the intensity of the Cu_2O (111) and (220) peaks at 200 °C was negligible. This is the temperature where Cu NPs started to get slightly oxidized. The Cu NPs in the paste can remain not oxidized until 200 °C, probably because there is still organic protection layers present before 193.1 °C, as obtained from the TGA measurements (Figure 5.1 b). As the temperature increased to 250 °C, Cu NPs were exposed to air, without organic protection, the Cu_2O (111) peak grew much stronger. The other two Cu_2O peaks: Cu_2O (200) and Cu_2O (220) started to appear in the XRD pattern. From 250 – 300 °C, the Cu_2O peaks continued growing, which indicates further oxidation. Correlated with the TGA in the air (5.1 b), a mass increase above 246.2 °C was mainly contributed by further oxidation of Cu NPs above 250 °C. Based on the analysis above, this Cu NP-based paste can resist oxidation in air below 200 °C, and get partially oxidized between 200 – 250 °C.

According to the TGA measurements in Ar and air and elevated XRD analysis in the air, most organic additives in the Cu paste can be removed at 193 °C. Furthermore, the oxidation level in the Cu paste in air can remain low level until 250 °C. Therefore, the appropriate in-air sintering temperature of this Cu paste is between 200 – 250 °C.

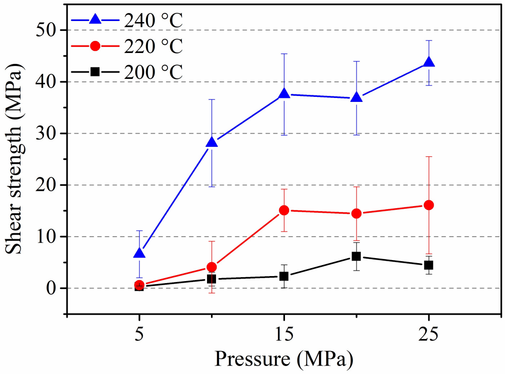

Figure 5.4: Shear strength of sintered Cu NPs joints at various temperatures and pressures.

5.3.2. SINTERING PARAMETER OPTIMIZATION AND SINTERING JOINTS CHARACTERIZATION

Based on the TGA and XRD results, three sintering temperatures, from 200 $^\circ C$, 220 $^\circ C$ to 240 $^\circ C$, five levels of external pressure, from 5 MPa to 25 MPa, were selected in the experiment. After 3 min of sintering, each batch cooled down to room temperature naturally. A shear strength test as described above was conducted to evaluate the mechanical property of the sintered Cu NP joints. Figure 5.4 shows the shear strength of sintered Cu NP joints prepared at various sintering temperatures and pressures.

Samples sintered at 200 $^\circ C$, under an external pressure of 5 MPa, showed the lowest shear strength of 0.29 MPa. As sintering pressure increases, the shear strength slightly improved to 4.46 MPa at 25 MPa. When the sintering temperature is 220 $^\circ C$, samples showed a low shear strength of 0.61 MPa at the pressure of 5 MPa. As pressure rise to 15 MPa, there is a big improvement of shear strength to 15.09 MPa. After that, the shear strength of samples does not show much improvement, with increased external pressure. At 240 $^\circ C$, shear strength of 6.59 MPa was obtained from sintering under pressure of 5 MPa. From pressure of 5 – 10 MPa, the shear strength increased more than four times, from 6.59 MPa to 28.1 MPa. The highest improvement of shear strength is observed here. After external pressure of 10 MPa, the shear strength continued to increase, until the pressure rises to 25 MPa. However, the increase rate is much lower than the pressure of 5 – 10 MPa. Therefore, the highest shear strength of 41.63 ± 4.35 MPa was achieved at 240 $^\circ C$, 25 MPa. In this experiment, samples sintered at 240 $^\circ C$, 10 MPa have a shear strength of 28.1 ± 8.47 MPa, which already meets the requirements for die attach in power electronics applications. In addition, high pressure during sintering might introduce the risk of sample damage. As a result, sintering at 240 $^\circ C$, 10 MPa is the optimal sintering condition.

After the shear strength test, both macro- and micro- fracture surface morphology analyses were performed to evaluate the fracture mode of Cu NP joints under various sintering conditions. Optical images of the shear surfaces and fracture modes of rep-

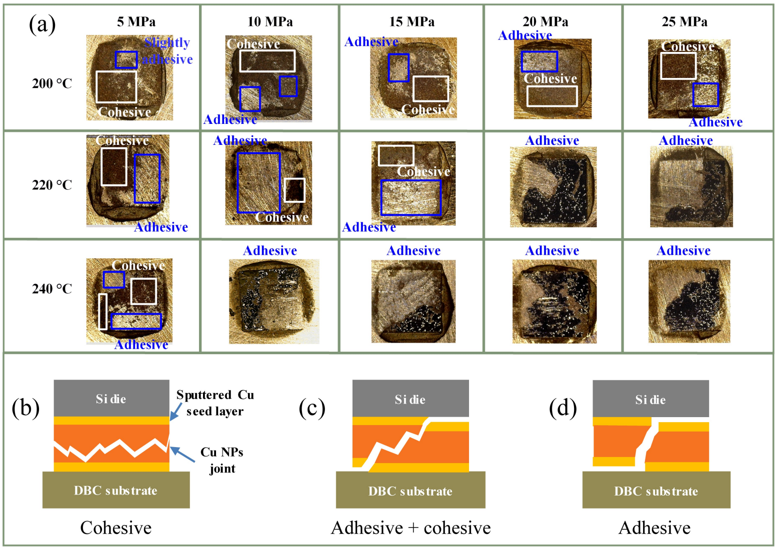

Figure 5.5: Sheared surfaces of sintered Cu NP joints at various temperatures and pressures. Areas presenting different fracture modes are labeled accordingly.

resentative samples under each sintering condition are presented in Figure 5.5 a. Two types of fracture modes are observed: adhesive and cohesive. As depicted in Figure 5.5 b, a cohesive fracture happens inside Cu joints. Only Cu NPs are shown on most of the fracture surfaces. In adhesive mode (Figure 5.5 d), fracture happens mainly at two interfaces: one is between the Cu NPs and DBC substrate, the other is between the sputtered Cu and Ni layers. Cu NPs are barely seen on the fracture surfaces. While it is also possible for both fracture modes to occur simultaneously (Figure 5.5 c). In this case, Cu joints, DBC substrate and sputtered Cu layers can be observed together. When sintering at 200 $^\circ C$, samples processing at different pressures all presented mixed-fracture modes. Samples sintered at 220 $^\circ C$, with pressures between 5 to 15 MPa, also exhibited the mixed fracture modes. However, when pressure was higher than 10 MPa, there were much fewer cohesive fractures. Cohesive fractures indicate the Cu NPs did not form strong and long-range connections, which can result in lower shear strength, as presented in Figure 5.4. Under this sintering condition, Cu NPs were supplied with higher energy and compact closer to form inter-particle connections. Therefore, fewer cohesive fractures occurred and dramatic shear strength improvement could be observed from 5 to 10 MPa at 220 $^\circ C$. Furthermore, when sintering pressure rise to 20 MPa and above at 220 $^\circ C$, the fracture mode changed into an adhesive mode, indicating a more condensed joint structure. Sintered joints have better mechanical strength than these interface layers. When sintering temperature increased further to 240 $^\circ C$, the adhesive fracture mode dominates, except at 5 MPa. From 240 $^\circ C$, 10 MPa, adhesive fractures occurred at two interfaces, which means sputtered Cu seed layers and interface adhesion failed before the Cu NP joints fractured. Thus, the shear strength also experienced the highest increase.

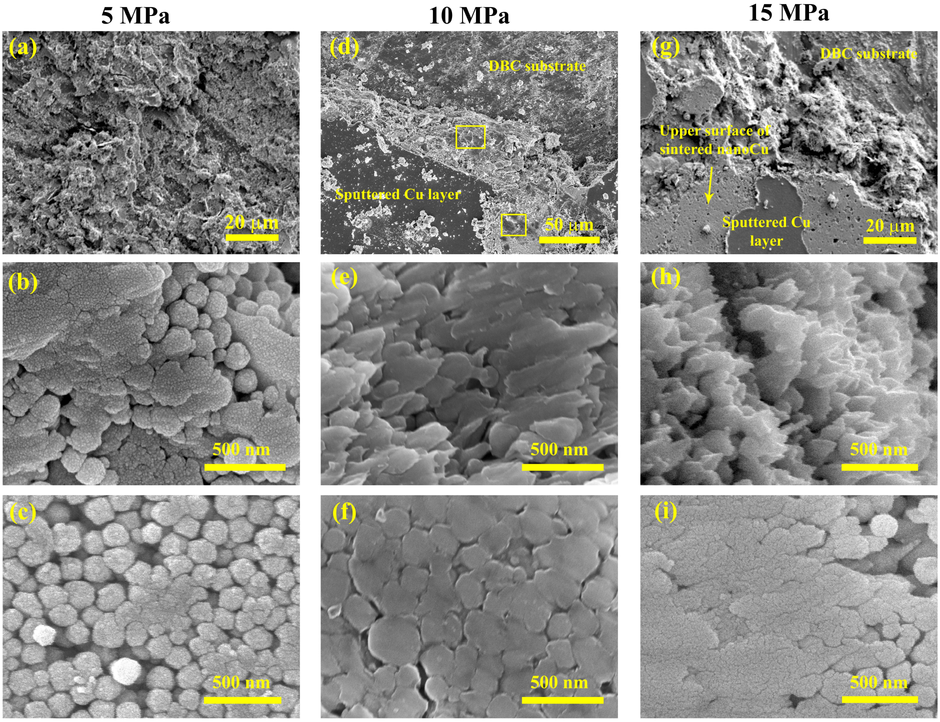

Figure 5.6: SEM images of fracture surfaces of Cu NPs paste sintered at 240 $^{\circ}C$ and various of pressures: (a-c) 5 MPa, (d-f) 15 MPa and (g-i) 25 MPa, and a schematic drawing of the corresponding fracture modes.

Since 240 $^{\circ}C$, 10 MPa is determined as the optimal process parameter, samples sintered at 240 $^{\circ}C$ under three pressures (5, 10 and 15 MPa), were selected for microstructure observation (Figure 5.6). At 5 MPa (Figure 5.6 a – c), a porous structure with Cu NPs were shown on the fracture surface, corresponding to a cohesive mode. Figure 5.6 b shows the area where slight plastic deformation can be observed, due to fracture. It also contains a mixture of Cu NPs at different sintering stages. There are still many particles observed to have a spherical shape, which indicates low-level sintering. On the upper surface of Cu joints (Figure 5.6 c), only a few Cu NPs in the center were sintered with neck formations. With a low pressure of 5 MPa, evaporated organic additives were not eliminated completely. As a result of that, Cu NPs are loosely packed together, without large sintering neck formations and long-range connections. Therefore, cracks can be easily initiated and propagate inside Cu joints, which led to a low mechanical strength consequently.

When sintering pressure increased to 10 MPa, in Figure 5.6 d, the DBC substrate, peeled-off sputtered Cu, DBC substrate and a small area of the sintered Cu joint are shown in the fracture surface area. Plastic deformation of sintered NPs started to occur during failure, as shown in Figure 5.6 e. In Figure 5.6 f, large sintering necks and continuous connections with neighboring Cu NPs were formed. Thus, there is a dramatic drop

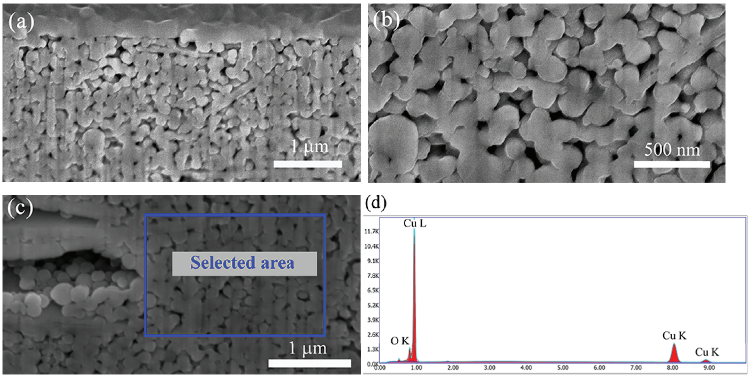

Figure 5.7: (a-b) FIB/SEM images of the microstructure cross-section of the Cu NP joint sintered at 240 °C, 10 MPa. (c) EDX detection area on the cross-section of the Cu NP joint and (d) the spectrum.

in porosity comparing to 5 MPa samples, which results in a huge increase in mechanical strength. With a pressure increase from 5 to 10 MPa, most of the organic solvents in the pores were removed by reducing the porosity of Cu joints. A much more compact sintered microstructure is achieved. While the shear test, cracks can propagate easier at interfaces than inside Cu joints. This results in the typical adhesive fracture surfaces. This dramatic change at 10 MPa makes it the optimum process condition. When the sintering pressure increased to 15 MPa, the adhesive fracture surface in Figure 5.6 g shows mainly the sputtered Cu seed layer and DBC substrate and some area of the upper surface of the Cu NP joints. Figure 5.6 h shows the much more steep fracture surface, where plastic deformation presents. It has a similar morphology as at 10 MPa. In Figure 5.6 f, most of Cu NPs become integral with lower porosity, indicating a higher-level of sintering. With higher pressure, vaporized organic residues in between Cu NPs were pressed out further than 10 MPa. More Cu NP surfaces were exposed for surface diffusion and sintering neck formations. This condensed microstructure sintered at 15 MPa prompts the shear strength to a higher value. However, the fracture mode and microstructure between 10 to 15 MPa share a few common features. Less sintering promoted progress was achieved under this condition. Therefore, the shear strength experienced a lower growth rate.

As discussed above, besides temperature, the pressure level during sintering has also an essential effect on Cu NPs microstructure. The increase of pressure results in a microstructure with a higher density of sintered Cu joints. Therefore the mechanical strength of sintered Cu joints improves tremendously, even with possible surface oxide formation, due to high process temperature in air.

Cross-section microstructure of one representative sample under the optimum sintering condition (240 °C, 10 MPa), was characterized, in Figure 5.7 a – b. Compared to the sample processed at 240 °C, 5 MPa, more sintering neck formation between particles and lower porosity can be observed. Thus a tremendous improvement in the shear strength of this sample was obtained. Considering the possibility of oxidation at sintering temperature in air, an SEM/EDX was taken to evaluate the oxygen content within the

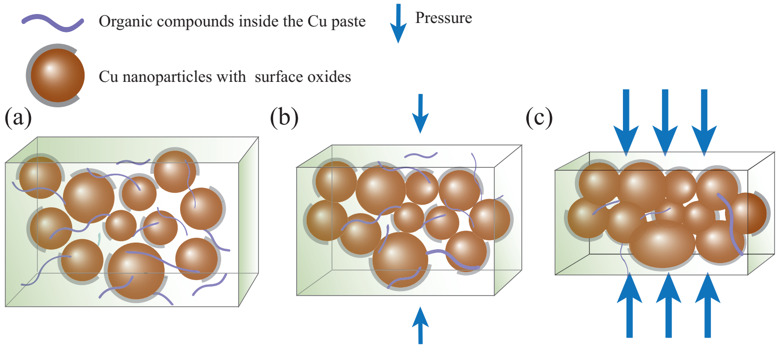

Figure 5.8: Schematic effect of pressure during sintering of Cu NP paste. (a) Cu NP paste before sintering. (b) Cu NP paste sintered under low pressure and (c) high pressure.

Cu joint. As shown in Figure 5.7 d, a small amount of oxygen element (around 0.5 wt%) was detected in the selected area. It could possibly have originated from two sources: surface oxidation of the Cu NPs, or organic residues from evaporation during the process. The XRD pattern of Cu paste at 250 °C in the air also depicts Cu_2O peak, which can be correlated here. Due to the small amount of oxidation, it does not have a strong negative effect on the sintering process. Condensed sintered Cu NP joints can be achieved under the appropriate sintering condition.

As reviewed for Ag NP paste sintering [30], higher pressure during sintering can lower the activation energy required for sintering initiation. Considering Cu and Ag may have similar metallic properties, with increased sintering pressure, the activation energy for Cu NP sintering can be possibly decreased. Figure 5.8 shows a schematic elaboration of pressure effect during sintering in air. Before sintering, Cu NPs in the paste are separated by complex organic additives. Particle surfaces are covered to prohibit oxidation and sintering. With the assistance of low pressure, vapored organic additives and air are partially removed by the assistance of pressure. Cu NP surfaces thus can be exposed, and Cu atoms can diffuse between particles for the formation of sintering necks [30–33]. Since the sintering process is performed at relatively high temperatures in the air, a small amount of oxidation can form on the Cu NP surfaces. However, due to voids created by organic residue, and possible oxidation which can keep further distance between particles, no continuous and long-range connections networks are formed, under low pressure. Consequently, samples can result in poor mechanical strength. As sintering pressure increases, most of the evaporated organic additives and air can be removed. Almost all the Cu NP surfaces are exposed and then brought to close proximity to initiate sintering. A low level of air during sintering also limits the further oxidation at process temperatures. Advanced level of sintering, with condensed microstructures and 3D connection networks, can be achieved with high pressure. As a result of that, the shear strength of sintered joints can be improved significantly, even without any protective atmosphere. In conclusion, in-air low temperature sintering of Cu NP paste can be applied in the die-attach for power electronics applications.

5.4. CONCLUSION

IN this study, the in-air sintering behavior of Cu paste under various process conditions was investigated and analyzed. Based on the paste characterization results, in-air sintering temperature range was determined and multiple pressure-assisted sintering experiments in air were performed. As temperature and pressure increase, Cu NPs form more condensed structures with neighboring particles. Both of these factors accelerate the neck formation and inter-particle connection inside Cu joints. Therefore, a maximum shear strength of $41.63 \pm 4.35\ MPa$ was obtained under the sintering condition of $240\ ^{\circ}C$, $25\ MPa$ for $3\ min$. It was also discovered that the highest shear strength improvement can be achieved at $240\ ^{\circ}C$, $10\ MPa$ to $28.1 \pm 8.47\ MPa$, which already meets the requirements for die attach in power electronics applications. Considering the cost of production and the risk of the die being damaged at high pressure, it is determined as the optimal sintering condition. Based on the experiments and characterization analysis, it can be concluded that in-air sintering with pressure assistance of Cu NP-based paste can be applied in die-attach for power electronics applications.

REFERENCES

[1] H. A. Mantooth, M. D. Glover, and P. Shepherd. Wide bandgap technologies and their implications on miniaturizing power electronic systems. *IEEE Journal of Emerging and Selected Topics in Power Electronics*, 2(3):374–385, 2014.

[2] P. G. Neudeck, R. S. Okojie, and Liangyu Chen. High-temperature electronics - a role for wide bandgap semiconductors? *Proceedings of the IEEE*, 90(6):1065–1076, 2002.

[3] Wolfgang Arden, Michel Brillouët, Patrick Cogez, Mart Graef, Bert Huizing, and Reinhard Mahnkopf. More-than-moore white paper. *ITRS White Paper*, 14, 2010.

[4] Thomas Siewert. *Properties of lead-free solders*. Thesis, 2002.

[5] Y. Yamada. *Die-Attach Materials for High Temperature Applications in Microelectronics Packaging*, pages 181–196. Springer International Publishing, 2019.

[6] William Chen, WR Bottoms, Klaus Pressel, and Juergen Wolf. The next step in assembly and packaging: system level integration in the package (sip). *ITRS White Paper*, 9, 2008.

[7] Daniel Lu and C. P. Wong. *Materials for advanced packaging*, volume 181. Springer, New York, 2009.

[8] Ph Buffat and Jean Pierre Borel. Size effect on the melting temperature of gold particles. *Physical review A*, 13(6):2287–2298, 1976.

[9] K. N. Tu. Reliability challenges in 3d ic packaging technology. *Microelectronics Reliability*, 51(3):517–523, 2011.

[10] Zheng Zhang, Chuantong Chen, Yang Yang, Hao Zhang, Dongjin Kim, Toru Sugahara, Shijo Nagao, and Katsuaki Suganuma. Low-temperature and pressureless

sinter joining of cu with micron/submicron ag particle paste in air. *Journal of Alloys and Compounds*, 780:435–442, 2019.

[11] S. T. Chua and K. S. Siow. Microstructural studies and bonding strength of pressureless sintered nano-silver joints on silver, direct bond copper (dbc) and copper substrates aged at 300 °c. *Journal of Alloys and Compounds*, 687:486–498, 2016.

[12] S. Siow Kim. Mechanical properties of nano-silver joints as die attach materials. *Journal of Alloys and Compounds*, 514:6–19, 2012.

[13] Chengjie Du, Xin Li, Yunhui Mei, and Guoquan Lu. An explanation of sintered silver bonding formation on bare copper substrate in air. *Applied Surface Science*, 490:403–410, 2019.

[14] Hao Zhang, Yang Liu, Lingen Wang, Fenglian Sun, Jiajie Fan, Mark D. Placette, Xuejun Fan, and Guoqi Zhang. Effects of sintering pressure on the densification and mechanical properties of nanosilver double-side sintered power module. *IEEE Transactions on Components, Packaging and Manufacturing Technology*, 9(5):963–972, 2019.

[15] Xiaomin Wang, Yunhui Mei, Xin Li, Meiyu Wang, Zhenduo Cui, and Guoquan Lu. Pressureless sintering of nanosilver paste as die attachment on substrates with enig finish for semiconductor applications. *Journal of Alloys and Compounds*, 777:578–585, 2019.

[16] Jianfeng Li, Christopher Mark Johnson, Cyril Buttay, Wissam Sabbah, and Stéphane Azzopardi. Bonding strength of multiple sic die attachment prepared by sintering of ag nanoparticles. *Journal of Materials Processing Technology*, 215:299–308, 2015.

[17] Raphaël Riva, Cyril Buttay, Bruno Allard, and Pascal Bevilacqua. Migration issues in sintered-silver die attaches operating at high temperature. *Microelectronics Reliability*, 53(9-11):1592–1596, 2013.

[18] Hongqiang Zhang, Wengan Wang, Hailin Bai, Guisheng Zou, Lei Liu, Peng Peng, and Wei Guo. Microstructural and mechanical evolution of silver sintering die attach for sic power devices during high temperature applications. *Journal of Alloys and Compounds*, 774:487–494, 2019.

[19] M. Yeadon, J. C. Yang, and R. S. Averback. In-situ observations of classical grain growth mechanisms during sintering of copper nanoparticles on (001) copper. *Appl Phys Lett*, 71, 1997.

[20] Jingdong Liu, Hongtao Chen, Hongjun Ji, and Mingyu Li. Highly conductive cu–cu joint formation by low-temperature sintering of formic acid-treated cu nanoparticles. *ACS Applied Materials & Interfaces*, 8(48):33289–33298, 2016.

[21] W. van Zeijl, Henk, Y. Carisey, Andrei Damian, R. H. Poelma, A. Zinn, Alfred, and Guoqi. Zhang. Metallic nanoparticle based interconnect for heterogeneous 3d integration, 2016.

[22] Boyao Zhang, Y. C. P. Carisey, A. Damian, R. H. Poelma, H. W. van Zeijl, and Guoqi Zhang. 3d interconnect technology based on low temperature copper nanoparticle sintering, 2016.

[23] Junjie Li, Xing Yu, Tielin Shi, Chaoliang Cheng, Jinhu Fan, Siyi Cheng, Guanglan Liao, and Zirong Tang. Low-temperature and low-pressure cu–cu bonding by highly sinterable cu nanoparticle paste. *Nanoscale Research Letters*, 12(1):255, 2017.

[24] Hideo Nakako, Dai Ishikawa, Chie Sugama, Yuki Kawana, Motohiro Negishi, and Yoshinori Ejiri. Sintering copper die-bonding paste curable under pressureless conditions, 2017.

[25] H. Nakako, C. Sugama, Y. Kawana, M. Negishi, Y. Yanaka, D. Ishikawa, and Y. Ejiri. Sintering cu bonding paste: cycle reliability and applications. In *International Exhibition and Conference for Power Electronics, Intelligent Motion, Renewable Energy and Energy Management (PCIM Europe 2018)*, pages 1–6.

[26] Yang Zuo, Jun Shen, Youdian Hu, and Runhua Gao. Improvement of oxidation resistance and bonding strength of cu nanoparticles solder joints of cu–cu bonding by phosphating the nanoparticle. *Journal of Materials Processing Technology*, 253:27–33, 2018.

[27] Y. Y. Dai, M. Z. Ng, P. Anantha, Y. D. Lin, Z. G. Li, C. L. Gan, and C. S. Tan. Enhanced copper micro/nano-particle mixed paste sintered at low temperature for 3d interconnects. *Applied Physics Letters*, 108(26):263103, 2016.

[28] Ho Jung, Kwang, Deuk Min, Kyung, Jae Lee, Choong, and Boo Jung, Seung. Pressureless die attach by transient liquid phase sintering of cu nanoparticles and sn-58bi particles assisted by polyvinylpyrrolidone dispersant. *Journal of Alloys and Compounds*, 781:657–663, 2019.

[29] Yang Zuo, Jun Shen, Jiacheng Xie, and Lu Xiang. Influence of cu micro/nano-particles mixture and surface roughness on the shear strength of cu-cu joints. *Journal of Materials Processing Technology*, 257:250–256, 2018.

[30] Peng Peng, Anming Hu, Adrian P. Gerlich, Guisheng Zou, Lei Liu, and Y. Norman Zhou. Joining of silver nanomaterials at low temperatures: processes, properties, and applications. *ACS Applied Materials & Interfaces*, 7(23):12597–12618, 2015.

[31] Won Yoon, Jeong and Hoon Back, Jong. Effect of sintering conditions on the mechanical strength of cu-sintered joints for high-power applications. *Materials*, 11(11):2105–2117, 2018.

[32] Yujin Seong, Youngkyu Kim, Randall German, Sungho Kim, Seong-Gon Kim, See Jo Kim, Hak Jun Kim, and Seong Jin Park. Dominant mechanisms of the sintering of copper nano-powders depending on the crystal misalignment. *Computational Materials Science*, 123:164–175, 2016.

[33] Y. Zhang, L. M. Wu, X. Y. Guo, Y. G. Jung, and J. Zhang. Molecular dynamics simulation of electrical resistivity in sintering process of nanoparticle silver inks. *Computational Materials Science*, 125:105–109, 2016.

6

CONCLUSIONS

6.1. CONCLUSIONS

In this thesis, both fundamental knowledge about die-attach process were conducted with the Cu NPs-based paste in power electronics. These research works give the insight of Cu NP-based paste sintering from various perspectives. These knowledge and experience can be transferred as the significant information to push the Cu NP-based paste into industrial application.

To understand the dynamic sintering mechanism of Cu paste, a MEMS-based TRXRD nanomaterial characterization platform was firstly designed and fabricated. It enables TRXRD study of crystalline structure and in-situ electrical resistance simultaneously. It contains an embedded MHP for temperature control, and four-point electrical measurement electrodes for in-situ electrical measurement. A gas cell was employed to provide an environmental experimental condition, without interference with XRD measurements. To achieve the optimum temperature fast switch and mechanical stability, two designs with different lateral thermal isolation structures, including Si_2O and suspended Si membrane with beams, were proposed and fabricated. With these designs, 60 ms and 50ms minimum heat pulse widths and uniform temperature distribution were achieved respectively. The later design shows faster temperature response and larger operation range. A series of assessment of fabricated devices were conducted to characterize, calibrate temperature and power consumption at wafer-level. Furthermore, a gas cell compatible with existing X-ray diffractometer was designed and installed. Combined with the gas cell and a power supply, it can enable TRXRD characterization of nanomaterial, with a large flexibility of temperature and gas environment control.

With developed characterization platform, both static and time-dependent investigations of sintering process of a commercial Cu NPs-based paste were performed under forming gas (5% H_2 + 95% N2). Series of XRD patterns and in-situ electrical resistance measurement were collected, followed with XRD intensity evaluation, microstrain, crystallite size analysis and microstructure observation. In the static study, from 25 – 285 $^\circ C$, three sintering stages, including solvent evaporation, surface oxide reduction and sintering, can be determined. The process begins with solvents evaporation. At 180 $^{\circ}C$, reduction of surface oxidation initiates, as some Cu NPs were exposed in forming gas. 240 $^{\circ}C$ is the temperature where formation of sintering neck starts. The measured resistance agrees with the microstructure of sintered joints. Additionally, a dynamic study of Cu paste sintering using a number of heat pulses at 300 $^{\circ}C$ were applied to capture the continuous sintering process at variant time. It is found that there are also three sintering stages, the same as in static study. Differently, during sintering at constant temperature, sufficient time and energy, which is 40 sec at 300 $^{\circ}C$, is needed to remove organic solvents and additive, before sintering necks and connections formation. Afterward, the reduction of surface oxides and followed sintering process can occur. From microstructure observations, long sintering time might be needed to obtain more dense sintered joints. These results and insights are on the one hand, a validation of the function of the developed MEMS-based TRXRD nanomaterials characterization method and platform. On the other hand, they can be transferred to process development and material optimization for Cu NP-based paste.

On the application side, the same commercial Cu NPs-based paste was applied in the Si die-attach application, using pressure sintering process in an industrial equipment. Unlike most reported process of Cu paste, these pressure sintering experiments were conducted in air. The in-air sintering behavior of Cu paste under various process conditions was investigated and analyzed. Based on the paste characterization results, in-air sintering temperature range was determined and multiple pressure-assisted sintering experiments in air were performed. As temperature and pressure increase, Cu NPs form more condensed structures with neighboring particles. Both of these factors accelerate the neck formation and inter-particle connection inside Cu joints. Therefore, maximum shear strength of 41.63 ± 4.35 MPa was obtained under the sintering condition of 240 $^{\circ}C$, 25 MPa for 3 min. It was also discovered that the highest shear strength improvement can be achieved at 240 $^{\circ}C$, 10 MPa to 28.1 ± 8.47 MPa, which already meets the requirements of the die attach in power electronics. Considering the process cost and the risk of the die damage at high pressure, it can be determined as the optimal sintering condition. Moreover, the experiments and microstructure of fracture surfaces, it also support that pressure assistance in-air sintering of Cu NP-based paste can be applied in die-attach for power electronics.

6.2. FUTURE WORKS

THE work proof the concept to combine a MEMS-based device with conventional XRD. This unique combination shines lights into understanding the sintering process and Cu paste. In addition, feasibility to employ pressure sintering in power electronics application has been performed. However, there are more works with many details need to be done in the future.

- TRXRD study of Cu paste with variant temperature profiles and gas environment. As proved in Chapter 3 and 4, the developed TRXRD characterization platform can provide multiple valuable results of sintering material under different conditions. With customized process temperature profile and atmosphere, fast process optimization with deep material understanding can be completed in one experiment.

- Molecular level understanding of the sintering mechanism of Cu NPs, while surface oxides present. In Chapter 5, surface oxides of Cu NPs were found while it has a limited effect on sintering. A molecular dynamics simulation can help to understand fundamentally.

- To realize an industrial application in power electronics, reliability is one of the most important factors to consider. With optimized materials and processes, reliability tests, including thermal cycling, power cycling, and high temperature and high moisture storage, should be followed to push this technology closer to industrial applications.

ACKNOWLEDGEMENTS

AFTER four year of work and a long description of my result in academic language, I will use this part to give place for all the people inspire, guide, support and comfort me during these years. First, I would like to give my sincere appreciation to my promoter Prof. Guoqi Zhang. When I was still in San Diego, wondering about the future PhD, he shined me a light to transfer my material background knowledge into semiconductor application. This project's unique combination made me to have a new life in the Netherlands, experiencing another culture and knowledge. At this moment, I still believe I made the one of the most challenging but current decision to come to Delft as a PhD candidate. As a promoter, he is critical in research works, questioning the fundamental objectives and reason behind the projects. These discussions can be tough, but also reminds long time afterwards, and guides me through many important decisions.

Second, thank Rene Peolma, Jia Wei and Henk van Zeijl, for all your supervision, advice and guidance for me at all the critical points of my PhD journey. Rene always has a sharp and critical mind, brilliant writing and practical approach for work. These valuable characteristics enriched my way of working. Henk has a lot of new and fun idea in his mind. He's always busy with many tasks. But He is also willing to help everyone with his best effort. I got many supports from Henk in cleanroom process, experiment and research works. I also got impressed by his adventures after his holidays. Jia is not in my supervisor team, but we always have inspiring and interesting conversations about new ideas and also ragdoll cats. These discussions is the main source for me to complete half of my dissertations. Without my supervisors team, it will be impossible for me to finish this work. Yu, thank you for all the time we spend together revising paper and joking. I learned a lot from your feedbacks and suggestion in research and also career. Also, I would like to thank all the partners I worked with: Dr. Klaus Pressel, Dr. Jan Gulpen, Dr. Jurrian van Zijl, Andrei Damian. Thank you all for the support and information you share with me and bear me for little results in the early stage of my PhD.

To Dong Hu, who helped me with a lot of experiments and discussions, is not graduated successfully from KTH, Sweden, and joins us in Delft as a PhD candidate. Your fast learning and adaptability impressed me all the time. Go on, and wish to see you defence after four years. To my dear friends in the Netherlands, Yue Zhang, Rong Yu, Ding Luo, Yin Yi, Zeyu Liu, you are all brilliant friends to keep me feel accompanied, heart-warmed and truly happy in dark, rainy Holland. Thanks for all that time spent in your apartments in weekend evenings, and effort to keep my cat alive while I'm not at home.

Also, thank everyone in ECTM group and EKL stuff members: Luke Middelburg, Brahim Mansouri, Manjunath Ramachandrappa, Daniel Yi, Joost van Romijn, Zhen Cui, Tianyi Jin, Joost van Ginkel, Violeta Prodanovic, Aleksander Jovic, Juan, Amir Sammak, Cinzia Silvestri, Nikolas Gaio, Ronaldo Ponte, Zahra, Bruno Morana, Miki Trifunovic, William Quiros Solano, Marta Kluba, Sten Vollebregt, Massimo Mastrangeli, Tom Scholtes, Mario Laros, Giampaolo Lorito, Robert Verhoeven, Gregory Pandraud, Hitham Hassan,

Joost Berendse and Bianca Knot. Thanks for support, patience and productive discussions, from all of you. A special thanks to Marian Roozenburg, for being incredibly patient and efficient at the same time. Your office is always the place we can find some good solutions and candies. Hope you can come back very soon to join us again!

Last but not least, I would like to thank my dear parents and loved Chengyu. You provide the most precious support and endurance from deep of my heart to keep me going further in this journey. Thanks for my parents' devotion and persistence for long long time. The older I get, the more I realize how wonderful parents they are. They teach and form who I am, by providing me a wide land field to grow, without constrain. They are two of my best friends, who share a very strong bond with me, connecting me even from a faraway western country. Also, thanks Chengyu for all we have done together and your support for all the decisions I made. I believe we still have a long way to go, together.

Curriculum Vitæ

Boyao Zhang

30-07-1991	Born in Xi’an, China.

Education

2009–2013	Bachelor of Engineering Materials Science and Engineering Xi’an Jiaotong Univeristy Xi’an, China
2013–2016	Master of Science Materials Science and Engineering University of California, San Diego San Diego, USA
2016	PhD. Microelectronics Delft University of Technology Delft, the Netherlands *Thesis:* Low temperature sintering of Cu nanoparticle paste *Promotor:* Prof. dr. G. Q. Zhang

Awards

2015	Scholarship in Department of Materials Science and Engineering University of California, San Diego
2016	1st Best paper the 17th IEEE International Components and Electronic Packaging Technology (ICEPT), Wuhan, China

LIST OF PUBLICATIONS

3. **B. Zhang, A. Damian, J. Zijl, H. W. van Zeijl, J. Fan, Y. Zhang, G. Zhang**, *In-air sintering behavior of Cu nanoparticle-based paste for die attachment in high power electronics application,* **submitted to Scientific Reports, (2020)**.

2. **B. Zhang, A. J. Böttger, H. W. van Zeijl, P. M. Sarro, and G. Zhang**, *MEMS-enabled fast time resolve X-ray diffraction charaterization platform for copper nanoparticle sintering in heterogeneous integration application,* In 2019 20th International Conference on Solid-State Sensors, Actuators and Mi-crosystems & Eurosensors XXXIII (TRANSDUCERS & EUROSENSORS XXXIII),pp. **1772–1775**, (2019).

1. **B. Zhang, Y. C. P. Carisey, A. Damian, R. H. Poelma, G. Q. Zhang, and H. W. van Zeijl**, *3D interconnect technology based on low temperature copper nanoparticle sintering,* In 2016 17th International Conference on Electronic Packaging Technology (ICEPT), pp. **1163-1167**, (2016).